ALMA MATER STUDIORUM
UNIVERSITÀ DI BOLOGNA

DOTTORATO DI RICERCA IN
ASTROFISICA

Ciclo XXXIII

From fueling to quenching star formation across cosmic time

Presentata da:
Federica Loiacono

Supervisore:
Prof. Andrea Cimatti

Coordinatore Dottorato:
Prof. Francesco Rosario
Ferraro

Co-supervisori:
Dott. Carlotta Gruppioni
Dott. Margherita Talia

Esame finale anno 2021

«Anche quando poi
saremo stanchi
troveremo il modo per
navigare nel buio.»

Poetica, Cesare Cremonini
(Novembre 2017)

«Bologna mi ha salvato la vita.»

N. P.
(Dicembre 2020)

Abstract

Investigating the mechanisms that regulate star formation across cosmic time is a complex issue. The cosmic amount of star formation varies considerably as the Universe evolves but what drives this variation is still poorly known. Most of our knowledge of the cosmic star formation history at $z > 3$ relies on UV surveys, which could miss star formation obscured by dust. At present it is not clear what is the contribution from dusty galaxies missed by UV selections to the cosmic star formation rate density (SFRD) at $z > 3$. In order to properly account for the total SFRD is thus necessary to consider unbiased samples of galaxies selected in the IR/mm bands, which are sensitive to obscured star formation and to the emission of cold gas, that is, the fuel from which stars form. In addition, active galactic nuclei (AGN) are considered to play a crucial role in galaxy evolution. The cosmic star formation history shows indeed interesting similarities with the cosmic accretion history of supermassive black holes. According to models, AGN could be decisive in suppressing star formation in massive galaxies by depleting and heating their gas reservoirs. Despite this, more recent theories predict that AGN could also trigger star formation inside molecular outflows and contribute to form the spheroidal component of galaxies. These two mechanisms have been named as "negative" and "positive" AGN feedback on star formation and their study is crucial to understand what regulates the star formation activity inside galaxies.

The aim of this thesis is to investigate the processes that fuel and suppress star formation across cosmic. On one side, we focused on the study of cold gas in the early Universe. We derived the first [C II] 158μm luminosity function at $z \sim 5$ from a mm-selection of galaxies, serendipitously detected in the ALPINE survey. By using the [C II] line as a star formation rate indicator, we measured the cosmic SFRD at $z \sim 5$, which shows a possible excess compared to the estimates from UV surveys. On the other side, we studied the impact of both negative and positive AGN feedback on star formation. First, we investigated negative feedback in a massive galaxy at $z \sim 2$, which will possibly evolve into a passive galaxy. By using spatially resolved spectroscopic data, we studied the gas kinematics and unveiled the existence of a rotating disc and of an AGN-driven ionized outflow. We evaluated the impact of gas ejection on the host galaxy, concluding that the role played by AGN feedback in this object is quite unclear. Then, we studied positive feedback in a sample of 70 nearby star-forming galaxies by using the C III λ1176 photospheric line. We detected in several objects blueshifted C III absorption, which could be indicative of young stars formed inside outflows. This fact could be related to the AGN and star formation activity within the host galaxy, and to the presence of molecular outflows.

Despite the uncertainties affecting our analysis, studying cold gas and AGN feedback with spectroscopic data represents a powerful approach to constrain the processes that feed and quench star formation across cosmic time.

Contents

Chapter 1

Introduction

1.1 Galaxy evolution in the ΛCDM framework: what regulates star formation in galaxies?

According to models, galaxies form in dark matter halos from the gravitational collapse of baryons (Blumenthal et al. 1984). Then, they grow via merging of the dark matter halos and by continuous accretion of baryons and dark matter forming larger and larger structures. This hierarchical process is at the basis of the ΛCDM (cold dark matter) paradigm, which is the standard cosmological model, based on cold (i.e., non-relativistic) dark matter particles and with a cosmological constant Λ, which accounts for the accelerated expansion of the Universe (Riess et al. 1998). How galaxies evolve, how they increase their mass by converting cold gas into stars across cosmic time is still matter of debate, as the details of this process are mostly unknown.

Until a few years ago, it was thought that mergers of galaxies played a major role in their buildup by producing intense starburst episodes (e.g., Lacey & Cole 1993; Steinmetz & Navarro 2002). This scenario has been considerably revisited after the evidences of galaxies "downsizing" (i.e., stars form earlier in more massive galaxies and on a shorter timescale; Thomas et al. 2010) and the discovery of distant galaxies with extremely ordered velocity fields (Förster Schreiber et al. 2009; Wisnioski et al. 2015). In addition, several models favour a smooth accretion of cold gas from cosmic filaments rather than mergers events in feeding star formation (Kereš et al. 2005; Dekel et al. 2009). This is supported by the existence of a well defined main sequence of galaxies in the stellar mass versus star formation rate (SFR) plane (e.g., Rodighiero et al. 2011), as well as by the current estimate of the cosmic molecular gas density at high-redshift, which cannot explain the stellar masses of galaxies at $z \sim 0$ (Walter et al. 2020).

As star formation goes on inside galaxies and massive stars begin to die via supernova explosions, a substantial amount of energy is injected into the interstellar medium (ISM), which prevents further star formation by heating the ambient gas. Significant heating to the ISM is also provided by accretion on supermassive black holes (SMBHs) harbored in the nuclear region of galaxies, which may remove gas from their central regions (Carniani et al. 2017b; Fluetsch et al. 2019; Förster Schreiber et al. 2019). These processes have been referred to as "feedback" on star formation and their implementation in models is necessary to explain the observed properties of galaxies (e.g., Sijacki et al. 2007; Vogelsberger et al. 2014; Beckmann et al. 2017; Pillepich et al. 2018).

The impact of feedback could be particularly dramatic in massive spheroidal galaxies (see also Sect. 1.5). Several studies show that they form most of their stellar mass at $1 < z < 3$ and passively evolve after this epoch (Fontana et al. 2004; Arnouts et al. 2007; Thomas et al. 2010). The mechanism suppressing the star formation remains mostly uncertain. The energy injected by active BHs in the ISM could exert a major

role in these objects, which is currently matter of study.

From what has been said so far, we see that the picture about star formation in galaxies is quite hazy, as this process is governed by several mechanisms like feedback, accretion, heating and cooling of the ISM. The details of this complex interplay are poorly understood and they require further investigation across cosmic time.

In the next Sections we will focus on the star formation history of the Universe and on the effect played by feedback on star formation, with particular attention to the evolution of massive galaxies, as these topics are particularly relevant in this thesis.

1.2 The cosmic star formation history: a population of elusive dusty galaxies

It is now well known that the star formation rate density (SFRD) of the Universe varies significantly across cosmic time (Fig. 1.1; Madau & Dickinson 2014). Thanks to more than twenty years of multiwavelength investigations, it is firmly assessed that the SFRD drops by a factor of ~ 10 from $z \sim 2 - 3$ – the so-called "cosmic noon" – to the present day (e.g., Takeuchi et al. 2003; Schiminovich et al. 2005; Cucciati et al. 2012; Gruppioni et al. 2013; Magnelli et al. 2013; Bouwens et al. 2015; Finkelstein 2016; Oesch et al. 2018; Bowler et al. 2020). Nevertheless, at $z > 3$ our constraints are almost exclusively based on observations sampling the rest-frame ultraviolet (UV) emission, while the contribution from samples selected at other wavelengths remains quite uncertain.

In particular, far-infrared (FIR) and sub-mm/mm selections of galaxies are more sensitive to dusty star-forming galaxies (see Casey et al. 2014 for a review). These galaxies are elusive for UV/optical selections as the dust grains absorb the UV-light produced by young stars, re-emitting it as thermal radiation in the IR – redshifted to mm for distant objects. Therefore, dusty galaxies may be easily missed by UV surveys, especially at high-redshift. If the contribution of dusty galaxies to the cosmic SFRD is well taken into account at $z < 3$, it is still largely unconstrained at higher redshift. This can severely impact the estimate of the SFRD of the Universe, as the contribution of obscured objects to the cosmic SFRD increases with increasing redshift, becoming the dominant component at $z \sim 2$ (Magnelli et al. 2013).

Recent studies, carried out at mm and radio wavelengths, indeed hint at the presence of significant obscured star formation at $z > 3$ (Dunlop et al. 2017; Novak et al. 2017; Williams et al. 2019; Gruppioni et al. 2020; Talia et al. 2020). The fraction of obscured star formation actually estimated is about 20–40% of that provided by UV-bright galaxies at $z > 4.5$ (Gruppioni et al. 2020; Talia et al. 2020), witnessing how important it is to properly account for dusty objects at high-redshift.

This issue can be fundamental in the study of massive galaxies. It is not clear which are the progenitors of quenched ellipticals at low redshift (see also Sect. 1.5). The number density of powerful starburst galaxies does not explain the space density of spheroidal galaxies at $z \sim 0$ (e.g., Chapman et al. 2005). A fraction of the missing progenitors of massive ellipticals could lie among dusty galaxies at $z > 3$ without extreme star formation activity (Valentino et al. 2020).

Besides the amount of obscured star formation, a second intriguing aspect deals with the drivers of the cosmic SFRD. At the moment it is not clear if the variation of

Figure 1.1: Cosmic star formation history from UV (green, blue and magenta points) and IR surveys (red symbols). At $0 < z < 3$ the cosmic SFRD is well constrained by both UV-optical and IR surveys. We can see that the IR estimates of the cosmic SFRD are significantly higher than the UV ones, highlighting that most of the radiation produced by star formation is absorbed by dust and only a fraction emerges as UV light. The contribution of dusty galaxies at $z > 3$ is mostly unknown. Both plots are from Madau & Dickinson (2014).

the SFRD of the Universe is driven by a concomitant variation of the gas reservoirs of galaxies or if it depends on a change of the star formation efficiency across cosmic time (see also Sect. 1.4.3). In order to investigate this topic it becomes crucial to study the cold gas in distant galaxies, as it is the fuel from which stars form.

Finally, another major topic that we may want to consider with respect to star formation is what is the influence that active galactic nuclei (AGN), i.e., accreting SMBHs, exert on it. We will address this issue in the following Section.

1.3   Co-evolution of galaxies and black holes

Over the past two decades, it has been well assessed that SMBHs, harboured in the nuclear regions of galaxies, play a major role in the evolution of their hosts. Several studies showed the existence of many relations between the central BH and the spheroidal component of the galaxy (i.e., the bulge of spirals and the entire galaxy, in case of ellipticals). For instance, the ratio between the BH mass and the spheroid mass is found to be $\sim 10^{-3}$ (Magorrian et al. 1998; Marconi & Hunt 2003). In addition, the BH mass is related also to the velocity dispersion of the stars inside the bulge (Ferrarese & Merritt 2000; Gebhardt et al. 2000). These relations suggest that galaxies and BHs co-evolve during their life. In particular, the phases of activity that a SMBH can experiment due to the accretion of material from the host could play a key role in setting up the observed relations. During these phases, the energy realesed by an accreting BH can easily exceed the binding energy of the bulge by tens of times and thus can have a tremendous impact on its host (Fabian 2012). The action exterted by an AGN on its galaxy has been named "AGN feedback", and it constitutes one of the main ingredients in models of galaxy evolution.

In particular, AGN feedback can deeply affect the star formation activity of a galaxy. The star formation history of the Universe and the cosmic BH accretion rate
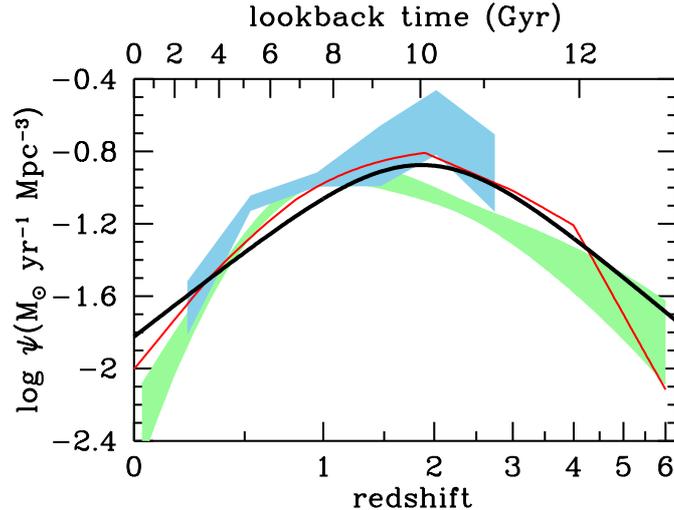
Figure 1.2: Cosmic star formation history (best-fit; solid line) compared to the accretion history of SMBHs. The latter was evaluated based on X-ray (red curve and green area; Shankar et al. 2009 and Aird et al. 2010) and IR observations (light blue area; Delvecchio et al. 2014). We can see that the two histories follow a similar trend. Figure from Madau & Dickinson (2014).

peak around the same epoch, suggesting a connection between the two processes across cosmic time (Fig. 1.2; Madau & Dickinson 2014). Therefore, if we want to understand the mechanisms governing star formation across cosmic time, we cannot prescind from the study of AGN.

To summarize what has been said so far, we have three main open problems that we may want to address about the cosmic star formation history:

1. *What is the amount of obscured star formation at $z > 3$?*

2. *What drives the shape of the cosmic SFRD?*

3. *What is the role played by AGN with respect to star formation?*

In particular, question 1) and 2) motivate the study of high-redshift galaxies in the mm/sub-mm domain, as these wavelengths are sensitive to the cold gas emission and dusty objects. In the following Section we will thus focus on the mm-astronomy and on the study of cold gas using the most advanced facilities.

Then, in Sect. 1.5, we will address question 3) by presenting the current state of the art of the studies about AGN feedback.

1.4 Cold gas at high-redshift

1.4.1 The [C II] 158 μm line: a game changer in the study of distant galaxies

The emission from cold gas can be detected using facilities operating in the mm and sub-mm domain. Several rotational transitions of molecules, as well as atomic fine

structure lines, fall indeed in this wavelength range (see Carilli & Walter 2013 for a review) and provide important information on the cold gas reservoirs of distant sources. For instance, the emission from the carbon monoxyde CO is commonly used to constrain the molecular gas mass of nearby and distant galaxies (Bolatto et al. 2013). However, at $z > 4$ the CO emission becomes difficult to detect because of the higher temperature of the Universe, which prevents the excitation of all but the highest transitions. An alternative tracer of the molecular gas mass is the neutral carbon [C I] emission at 370 μm and 609 μm, which is becoming increasingly used at high-redshift (Walter et al. 2011; Popping et al. 2017; Valentino et al. 2018; Nesvadba et al. 2019). Another important coolant of the ISM at the sub-mm wavelengths is the double-ionized oxygen [O III] 88 μm. This line can be very bright in presence of strong radiation fields or in a regime of low metallicity (Spinoglio & Malkan 1992; Stacey et al. 2010; Olsen et al. 2017). It has actually the record to have pinpointed the redshift of the most distant galaxy ($z = 9.1096$) currently ever observed (Hashimoto et al. 2018).

In particular, among the tracers of cold gas, we will focus on the singly ionized carbon [C II] 158 μm line (hereafter, [C II]) for the importance that this line is progressively assuming in the investigation of high-redshift sources.

The [C II] line is one of the brightest lines in the IR domain, radiating up to a hundredth of the entire FIR luminosity of a galaxy (Díaz-Santos et al. 2013). This line is mainly excited by collision with neutral hydrogen atoms in the so-called photo-dissociation regions (PDRs; Hollenbach & Tielens 1999) and in the neutral diffuse gas (Wolfire et al. 2003). Nevertheless, it can also trace diffuse ionized gas where it is excited by collisions with free electrons (e.g., Cormier et al. 2012). For this reason, the interpretation of the [C II] emission is not trivial, as many processes and phases of the ISM may contribute to it.

For high-redshift galaxies the [C II] line is conveniently redshifted into relatively transparent atmospheric windows, which makes this line relatively easy to observe from the ground. Until 2013, there were less than thirty [C II] detections in star-forming galaxies and quasars at $z > 1$ (Carilli & Walter 2013), while currently we have hundreds of [C II] observations, many of which at $z > 5$ (Decarli et al. 2018; Harikane et al. 2018; Pavesi et al. 2018a; Béthermin et al. 2020).

The [C II] line can be used for several purposes. Thanks to its brightness, [C II] is a powerful tool to derive accurate redshifts of distant galaxies (e.g., Walter et al. 2012; Riechers et al. 2013; Capak et al. 2015). In contrast to the CO emission, it is much less affected by the increasing temperature of the cosmic microwave background (CMB) up to $z \sim 4.5$ and beyond (Vallini et al. 2015), which makes this line ideal to study the cold ISM up to very high-redshift, close to the end of reionization. Spatially resolved observations of the [C II] emission can be used to characterize the kinematics of the cold ISM (Smit et al. 2018; Kohandel et al. 2019) and study galactic outflows and inflows (Maiolino et al. 2015; Ginolfi et al. 2020b).

In addition, when other sub-mm/mm lines are also available, their flux ratios can be used to study the physical properties of the ISM in terms of gas density, strength of the radiation field and excitation source (e.g., Pavesi et al. 2016, 2018a; Novak et al. 2019). The combined use of [C II] and [O III] 88 μm lines provides important insight on the multi-phase ISM of pristine galaxies, as their ratio is sensitive to the hardness of the radiation field and to the metallicity (Carniani et al. 2017a; Hashimoto et al. 2019). Moreover, the [C II] line has also been suggested to be a tracer of molecular gas
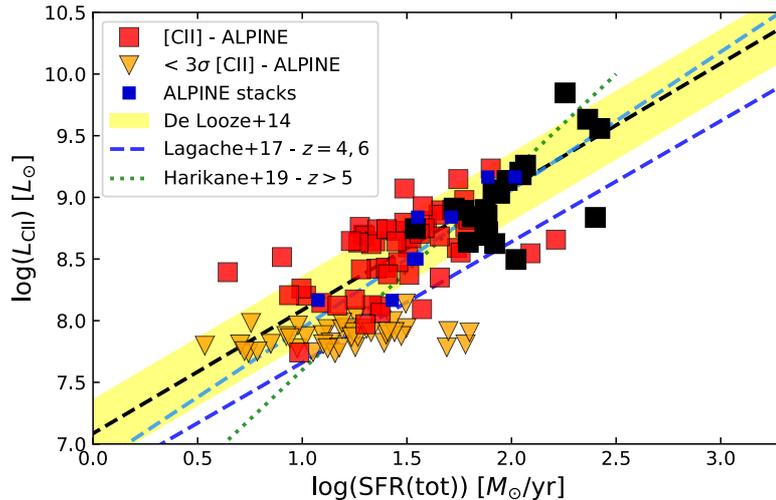
Figure 1.3: Relation between [C II] luminosity and SFR at $z \sim 5$. We see that the high-z galaxies of Schaerer et al. (2020) (squares and triangles) follow the linear relation found in nearby galaxies by De Looze et al. (2014) (yellow area). This fact suggests that the [C II] line can be used as a SFR indicator at both low and high redshift. Figure from Schaerer et al. (2020).

mass (Madden et al. 1997; Zanella et al. 2018).

Finally, [C II] results a SFR indicator at low and possibly at high-z both from observations (Stacey et al. 2010; De Looze et al. 2014; Magdis et al. 2014; Carniani et al. 2018; Matthee et al. 2019; Schaerer et al. 2020) and models predictions (Vallini et al. 2015; Lagache et al. 2018). The main limitation to the use of [C II] as a SFR tracer is the so-called "[C II] deficit" observed in low-redshift galaxies (Malhotra et al. 1997; Graciá-Carpio et al. 2011; Díaz-Santos et al. 2013), that is, a drop of the ratio between [C II] and IR luminosity with increasing IR luminosity. Some works reported a significant [C II] deficit with respect to the local [C II] – SFR relation in $z > 5$ sources (Harikane et al. 2018). However, recent studies seem to suggest no apparent [C II] deficit up to $z \sim 8$ (Schaerer et al. 2020), in line with other results (Carniani et al. 2018; Matthee et al. 2019) (Fig. 1.3).

We will focus on the use of the [C II] line in building luminosity functions and deriving the cosmic SFRD in Chapter 2 of this thesis.

1.4.2 New frontiers opened by ALMA

The Atacama Large Millimeter/submillimeter Array (ALMA) has marked a revolution in the study of cold gas. Historically, the first studies on cold gas were focused on galaxies extremely bright in the sub-mm domain (sub-millimeter galaxies; SMGs) or distant quasars using single dish radiotelescopes and bolometers (e.g., Ivison et al. 1998; Hughes et al. 1998). The main problem of these facilities is the confusion due to low spatial resolution coupled with high sensitivity. In addition, these studies sampled extreme sources, which are not representative of the overall population of galaxies.

The use of interferometry allows to overcome most of these limitations. With the advent of facilities like the Jansky Very Large Array (VLA), the Submillimeter Array (SMA), the IRAM/Plateu de Bure Interferometer (PdBI) (replaced now by the NOrth-

ern Expanded Millimeter Array; NOEMA), observations of cold gas in galaxies made a leap forward, by increasing the statistics and the quality of the data, expecially for distant sources.

ALMA represents the current end point of the advances in the field. Thanks to its unprecedented sensitivity and spatial resolution, ALMA allows us to study in detail the cold ISM in normal star-forming galaxies (i.e., not powerful SMGs) at early times. The dusty star-forming regions of distant sources can be resolved on sub-kpc scale, similar or even smaller than those resolved by optical telescopes (Hodge & da Cunha 2020). In addition, this interferometer is actually provided with eight fully working bands between 90 and 950 GHz that guarantee a wide frequency coverage. This makes it possible to pick up several emission lines in a single galaxy and to measure the IR continuum of high-redshift sources. Another advantage implied by the large bandwidth is that ALMA can be used as a "redshift machine" of distant galaxies with uncertain photometric redshifts by performing spectral scans.

The use of ALMA has determined a tremendous progress in the investigation of the high-redshift Universe. It enabled detailed studies of cold gas and dust (Díaz-Santos et al. 2018; Decarli et al. 2019a; Gullberg et al. 2019; Hodge et al. 2019) and to investigate the kinematics of rotating objects and merging events (Hashimoto et al. 2019; Smit et al. 2018). A remarkable progress has been made in resolving the cosmic IR background produced by unresolved extragalactic sorces, using blank fields (Hatsukade et al. 2013; Aravena et al. 2016; González-López et al. 2020) and serendipitous discoveries (Carniani et al. 2015a; Fujimoto et al. 2016). Moreover, the unique sensitivity of ALMA has allowed to detect the [C II] emission in normal star-forming galaxies at $z \sim 5$ (Capak et al. 2015; Willott et al. 2015), which were found to be bright in [C II] and likely poor in the dust content.

Finally, a substantial amount of ALMA observation time has been devoted to extragalactic large programs. For instance, the large program ASPECS (Decarli et al. 2019b) investigated the evolution of the CO luminosity function and the cosmic molecular gas density using blind observations (see next Section). On the other hand, ALPINE (Le Fèvre et al. 2020) targeted the [C II] line in 118 star-forming galaxies at $z \sim 5$ while REBELS (Bouwens 2020) studied the [C II] and [O III] 88 μm emission in 40 massive galaxies at $z > 6.5$. We will discuss in detail the ALPINE survey and its contribution to the study of cold gas at high redshift in Chapter 2 of this thesis.

1.4.3 The power of blind observations

Our knowledge of the cosmic SFRD is mostly based on deep surveys of blank fields, from UV to IR wavelengths. They are flux limited surveys of a well-defined volume of the Universe. It would be extremely useful to perform similar studies at the mm and sub-mm wavelengths, in order to complement the picture provided by previous surveys.

The main limitation of mm interferometers such as ALMA is their relatively small field of view, which makes surveys of blank fields expensive in terms of telescope time. Most of the studies at high-redshift have therefore focused on the exploration of properties of "targeted" galaxies that were pre-selected based on their stellar mass, SFR and/or IR luminosity (e.g., Daddi et al. 2015; Tacconi et al. 2018). These kind of studies have been instrumental to shape our understanding of the connection between the inner gas reservoirs and the build-up of galaxies. For instance, Tacconi et al. (2018)

found that high-redshift galaxies are more gas-rich compared to local objects. On the other hand, Scoville et al. (2017) found a decrease of the depletion time (i.e., the typical timescale of gas consumption) as a function of the lookback time, suggesting that galaxies might be more efficient in converting gas into stars at early epochs, even if this issue is still debated (Liu et al. 2019; Tacconi et al. 2018).

However, the pre-selection, whilst very convenient in terms of telescope time, may introduce biases associated to our prior knowledge of the emitting systems. This applies expecially to optically-faint galaxies, which may be missed in mass selected samples.

On the other hand, "blind" surveys (or, molecular line scans) aid to circumvent selection biases, thus enabling a proper census of the cold gas properties in a volume-limited region of the Universe. At present several extragalactic blind surveys have been conducted using ALMA and other interferometers (e.g., the JVLA), such as ASPECS Pilot (Walter et al. 2016) and Large Program (Decarli et al. 2019b), COLD–z (Pavesi et al. 2018b), GOODS–ALMA (Franco et al. 2018), ASAGAO (Hatsukade et al. 2018) and the mm-continuum imaging of the HUDF (Dunlop et al. 2017). In particular, the works of Decarli et al. (2016) and Riechers et al. (2019) estimated the cosmic evolution of the molecular gas density finding that it presents a behaviour that is similar to the cosmic SFRD. This result was then confirmed confirmed by Decarli et al. (2019b, 2020), who strongly reduced the uncertainties of the previous measurements (Fig. 1.4). The current estimates of the cosmic molecular gas density suggest that the variation of the cosmic SFRD could be driven by the gas content of galaxies rather than by a change in the star formation efficiency.

At the moment, blind surveys have been quite inefficient at $z > 4$, due to a combination of sensitivity, survey volume and evolution of the mass function of galaxies. An hybrid approach is to analyze serendipitous sources, that is, galaxies detected by chance in observations targeting other sources (Swinbank et al. 2012; Cooke et al. 2018; Wardlow et al. 2018; Lenkić et al. 2020). As their discovery is fortuitous, these objects are ideal to perform statistical studies because they are not pre-selected. Nevertheless, the fact that serendipitous sources are detected in pointed observations of other galaxies could introduce biases, if the environment around the main targets is strongly clustered (see also Hodge & da Cunha 2020). This is indeed the case that we have faced in this thesis, as it will be discussed in Chapter 2.

In particular, blind selections of lines and serendipitous discoveries in the mm-domain are sensitive to heavily obscured galaxies that can be missed in the UV surveys. Properly accounting for these objects is crucial when estimating global quantities such as the cosmic SFRD and building luminosity functions (see Chapter 2).

1.5 The feedback from active galactic nuclei on star formation

We introduced in Section 1.3 AGN feedback as a crucial mechanism to explain the observed relations between galaxies and their central BHs. Overall, AGN feedback has been captured into two main perspectives. The most traditional one and better constrained by observations has been called as "negative feedback" and consists in the suppression of star formation in the host galaxy, through winds and heating of the ambient medium. This process could have crucial implications in the shutdown of star formation in elliptical galaxies.
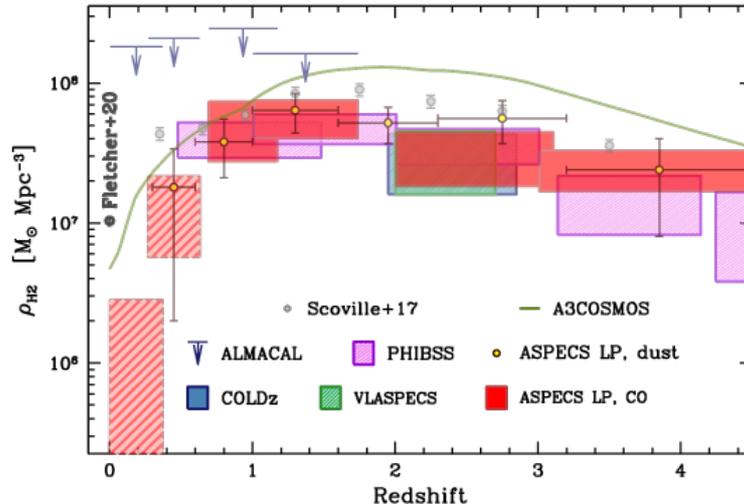
Figure 1.4: Cosmic molecular gas density from several observing campaings at sub-mm/mm wavelengths. We see that, on average, the cosmic molecular gas density shows a trend that is qualitatively consistent with the cosmic SFRD. Figure from Decarli et al. (2020).

A second and more recent picture predicts that AGN could be effective in triggering star formation inside cold outflows. This scenario is quite unclear as it is little constrained by observations. We will examine the feedback processes with more detail in the following Sections.

1.5.1 Negative feedback in massive galaxies

From the observational point of view, the detection of galactic outflows is the best evidence of AGN feedback at work[1]. These gas ejections reach velocity typically higher than $500 \ \mathrm{km \, s^{-1}}$ and extend on scale of several kpc (see Fabian 2012 for a review). They are multi-phase, as they involve several components of the ISM, from cold molecular gas to the ionized one (Rupke et al. 2017; Cicone et al. 2018; Fluetsch et al. 2019). These outflows may have a crucial impact on the star formation activity, by affecting the gas content of a galaxy.

In particular, AGN feedback has been invoked to explain the high-mass end of the stellar mass function (Fig. 1.5). There is indeed a discrepancy between the observed mass function of galaxies and the one predicted by numerical simulations of dark matter halos, scaled for the cosmic baryonic fraction (Naab & Ostriker 2017). This discrepancy affects both dwarf and massive galaxies. In particular, feedback from supernovae explosions and stellar winds has been invoked by models to explain the low-mass end of the stellar mass function. On the other hand, AGN would be effective in suppressing star formation in high-mass galaxies through the heating and ejection of the accreted gas (Naab & Ostriker 2017; Nelson et al. 2018; Weinberger et al. 2018).

In this context, AGN could exert a major role is the so-called "quenching" of star formation in spheroidal galaxies. It has been observed that massive ellipticals form most of their mass at $z > 1$ and passively evolve after that epoch (e.g. Glazebrook et al. 2004;

---

[1]We focus here on the so-called "radiative mode" of AGN feedback, consisting in fast gas ejections produced by a SMBH in a high accetion regime. A discussion on the "radio mode" feedback, i.e. feedback due to radio bubbles sorrounding galaxies and jets, is beyond the scope of this thesis.
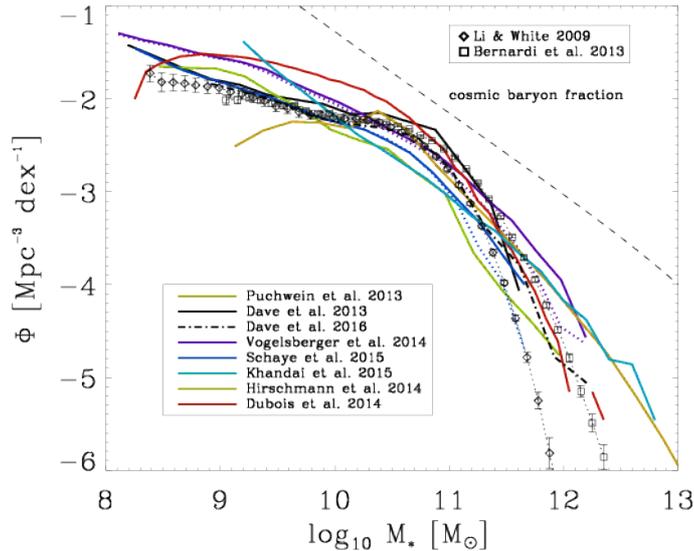
Figure 1.5: Mass functions of galaxies predicted by models (colored lines) compared to the one expected by the dark matter halos mass function and the cosmic baryonic fraction (dashed line). All the models include supernovae and AGN feedback, with the exception of Davé et al. (2013). The observed stellar mass functions from Li & White (2009) and Bernardi et al. (2013) are also shown. Figure from Naab & Ostriker (2017).

Cimatti et al. 2004, 2008; Onodera et al. 2015). Because of their high stellar density and size, considerably smaller compared to present-day ellipticals, the progenitors of these systems are thought to be compact star-forming galaxies at $1.5 < z < 3$ (e.g. van Dokkum et al. 2015) or at even higher redshift (Valentino et al. 2020). These objects are often characterized by a short depletion timescale inferred from the molecular gas content (Spilker et al. 2016; Barro et al. 2017; Tadaki et al. 2017), suggesting that they are rapidly exhausting their internal reservoir for star formation. However, new gas can be accreted from the circumgalactic and intergalactic medium (CGM/IGM) as shown by numerical simulations (Kereš et al. 2005; Dekel et al. 2009), which may keep sustaining the star formation activity.

To explain the quenching of star formation in spheroidal galaxies is thus necessary a mechanism that removes or heats the accreted gas, in order to make it not available to form stars. The main actor in this sense seems to be feedback from AGN. High-velocity winds driven by the AGN may be efficient in depleting the galaxy of the accreted gas, cutting off the fuel for star formation. This ejective feedback is implemented in models as a way to prevent both the BH and galaxy growth (e.g. King 2005; Springel et al. 2005; Di Matteo et al. 2005; Hopkins et al. 2016; Weinberger et al. 2017). Recent numerical simulations show that AGN may be crucial in populating the so-called "red sequence" in the color-mass plane of galaxies (Nelson et al. 2018). This is suggested also by the observations of Cimatti et al. (2013), who found the population of the red sequence by ellipticals between $z \sim 2.4$ and $z \sim 1.4$ and a decrease of the AGN activity in star-forming galaxies between the same redshifts, suggesting a connection between the two processes. However, if on the theoretical side AGN feedback is commonly invoked to explain the observed properties of galaxies, from the observational point of view we still lack a robust understanding of how AGN shape their hosts (Cresci & Maiolino 2018).

The mechanism converting a star-forming galaxy into a passive elliptical is still an open and trending topic and we will address it in Chapter 3 of this thesis.

1.5.2 Positive feedback: triggering of star formation inside outflows

According to models, AGN would not be effective only in suppressing star formation in a galaxy. Indeed, there are recent theories suggesting that molecular outflows driven by AGN and intense starbursts harbour the physical conditions to form stars. Star formation may be triggered by processes such as compression, fragmentation and cooling of the ambient medium either by the radiation pressure on dust (Ishibashi & Fabian 2015; Silk 2013; Zubovas et al. 2013a; Zubovas & Bourne 2017). This perspective in which stars form inside AGN and starburst-driven winds has been called "positive feedback", because this mechanism would contribute in the production of new stars in the host galaxy, rather than suppressing it. Rather than being an alternative mechanism to negative feedback, the positive one could represent a complementary process regulating star formation in galaxies.

Positive feedback could have several implications on galaxy formation and evolution. As reported by Gallagher et al. (2019), the stars formed in the outflow could contribute to the enrichment of the CGM and halo heating, to explain extragalactic supernovae and the $M_{\rm BH} - M_{\rm gal}$ relation (e.g., Marconi & Hunt 2003) between the BH mass and the mass of the spheroidal component of the host galaxy. At very high-redshift such a way of star formation could contribute to the reionization of the Universe due to the ionizing photons emitted by the outflowing stars (see Gallagher et al. 2019 for an in-depth discussion on these and other implications). Finally, since the stars formed in the outflowing gas would have the kinetic imprinting of the wind (i.e. high radial velocity), they could contribute to the building-up of the spheroidal component of galaxies, i.e. the bulge, the halo or even to the mass assembly of ellipticals (Ishibashi & Fabian 2014). In this scenario, the hypervelocity stars in the Milky Way halo as well as the stars with high radial orbits in the solar neighbourhood (Belokurov et al. 2018) could be associated to previous events of star formation inside outflows (Wang & Loeb 2018; Zubovas et al. 2013b). A formation process via outflows has also been suggested to explain a significant fraction of the halo stars in the Milky Way using cosmological simulations (Yu et al. 2020).

Observationally, studies reporting the detection of stars inside galactic outflows are quite rare. So far, the first promising results have been obtained by Maiolino et al. (2017); Gallagher et al. (2019) and Rodríguez del Pino et al. (2019). In Chapter 4 we will better highlight the findings of these works and discuss a new interesting observational perspective in this field.

1.6 Outline of this thesis

From the previous discussion, we notice that studying star formation in galaxies and understanding its evolution across cosmic time is a complex issue, as this process is regulated by several mechanisms.

In this thesis, we investigated the processes that fuel and quench star formation under two main perspectives. From one side, we focused on the study of cold gas in

high-redshift galaxies by using the [C II] emission line. In particular, we built the first [C II] luminosity function at $z \sim 5$ from a mm-selection of galaxies serendipitously detected in the ALPINE survey. As explained in Sect. 1.2, this kind of selection is particularly useful to unveil dusty objects. In particular, by using the [C II] line as a SFR tracer, we derived an estimate of the cosmic SFRD at early times that is sensitive to obscured star formation.

On the other side, we studied feedback on star formation in both its negative and positive version. Using multiwavelength spectroscopic data, we investigated the effectiveness of AGN in suppressing star formation in a massive galaxy at $z \sim 2$, which could be a possible progenitor of a quenched spheroidal galaxy. We then studied a sample of 70 nearby star-forming galaxies in order to unveil possible young stars formed inside galactic outflows.

This thesis is organized as follows:

Chapter 2 deals with the [C II] luminosity function at $z \sim 5$. We present the ALPINE ALMA Large Program and its legacy of serendipitous discoveries. We used the serendipitous sources to build the [C II] luminosity function and compared it with both theoretical and observational studies. We discuss also the overdense environment around star-forming galaxies at $z \sim 5$. Finally, we used the [C II] luminosity function to estimate the cosmic SFRD at $z \sim 5$.

Chapter 3 is devoted to the study of negative AGN feedback in GMASS 0953, a massive star-forming galaxy at $z \sim 2$. This galaxy is rapidly exhausting its gas reservoir due to its star formation activity and represents a possible progenitor of a passive spheroidal galaxy. We studied the kinematics of the ionized gas using spatially resolved spectroscopic data and compared it with the molecular gas motion. We found evidence of an AGN-driven outflow and discuss the impact of the outflow on the galaxy.

In Chapter 4 we study star formation inside galactic outflows. We used a sample of 70 star-forming galaxies to look for young stars inside outflows by measuring the velocity shifts of UV photospheric absorption lines. We investigated possible correlations between young stars inside the outflows and the SFR and AGN activity of the host galaxies. We also discuss a possible connection between molecular outflows and newly formed stars.

Finally, we present the concluding remarks and future prospects of this thesis in Chapter 5.

Chapter 2

The [C II] luminosity function at $z \sim 5$[1]

2.1 ALPINE: the ALMA Large Program to INvestigate [C II] at Early times

ALPINE is an ALMA large program that aims at the study of the [C II] emission and the dust continuum in 118 star-forming galaxies at $4.4 < z < 5.9$ (Le Fèvre et al. 2020; Béthermin et al. 2020; Faisst et al. 2020). This is the first statistical study of targeted [C II] emission at this cosmic epoch, right after the end of the reionization. As the galaxies are placed on the "main sequence" (e.g., Rodighiero et al. 2011; Speagle et al. 2014; Faisst et al. 2020), their analysis allows to investigate the cold ISM in normal star-forming galaxies (i.e., not extreme objects). The ALPINE targets have been UV-selected with 1500Å absolute magnitude $M_{1500} \leqslant -20.2$ mag and their redshifts are robustly constrained by UV-optical spectroscopy (Le Fèvre et al. 2015; Hasinger et al. 2018). The galaxies are located in well-studied sky regions, that is, the Cosmic Evolution Survey field (COSMOS; Scoville et al. 2007) and the Extended Chandra Deep Field-South (ECDFS; Giavalisco et al. 2004; Cardamone et al. 2010). For 75 out of the 118 targets (64% of the sample) the [C II] emission was successfully detected (Fig. 2.1) while only 23 sources show significant continuum emission (20 % of the sample). A comprehensive description of the targets catalogs is reported in Béthermin et al. 2020. Besides the study of the 118 targeted galaxies, the relatively large sky area covered by ALPINE (~ 27 arcmin^2) coupled with the richness in ancillary data make ALPINE ideal to study not only the central UV-selected galaxies but also sources serendipitously detected in the 118 ALMA pointings.

Up to now, ALPINE is obtaining several scientific highlights. Schaerer et al. (2020) studied the [C II] - SFR relation using the ALPINE targets, showing that there is no evolution of the local relation found by De Looze et al. (2014) (see also Chapter 1). By stacking the [C II] emission of the ALPINE galaxies, Ginolfi et al. (2020b) investigated star formation-driven outflows and their role in the chemical enrichment of the circumgalactic medium (CGM) at $z \sim 5$. The properties of the CGM were studied also by Ginolfi et al. (2020a), who found an interesting system of interacting galaxies at $z \sim 4.5$ with possible signatures of stripped gas. Furthermore, Fujimoto et al. (2020) analyzed the sizes of the [C II] emission, suggesting the existence of [C II] halos around star-forming galaxies. Fudamoto et al. (2020) studied the dust attenuation properties while Dessauges-Zavadsky et al. (2020) constrained the evolution of the molecular gas fraction and depletion timescale up to $z \sim 5.9$ by using the [C II] line as a molecular gas tracer. In addition, Khusanova et al. (2020) estimated the cosmic SFRD at $z \sim 4.5$ and

---

[1]Based on Loiacono F., et al., 2021, A&A, 646, 76.

2.1 ALPINE: the ALMA Large Program to INvestigate [C II] at Early times
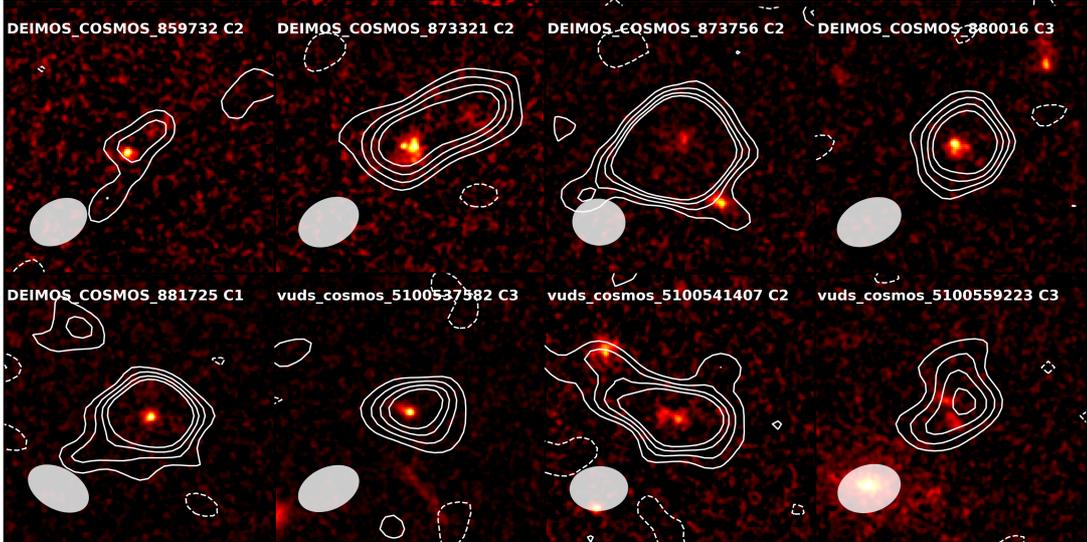
Figure 2.1: Example of the ALPINE galaxies with detected [C II] emission (ALMA data; white contour). The background images trace the rest-frame UV emission (HST-F814W; Koekemoer et al. 2007, 2011). The [C II] emission was detected in the 64% of the targets. Figure from Le Fèvre et al. (2020).

$z \sim 5.5$ by using the UV-selected ALPINE targets. New constrains have been derived also on the cosmic IR background by Béthermin et al. (2020). Finally, two papers have been devoted to the study of luminosity functions (LFs) of the [C II] line by using the ALPINE targets (Yan et al. 2020) and the serendipitous [C II] line emitters discovered in the ALPINE pointings (Loiacono et al. 2020). On the other hand, Gruppioni et al. (2020) used the the serendipitous sourced detected in continuum to build the IR LF up to $z \sim 6$.

This Chapter focuses on the [C II] LF at $z \sim 5$ derived from the serendipitous line emitters detected in ALPINE. This is the first [C II] LF based on galaxies purely selected for their [C II] emission. Despite being well-constrained at $z \sim 0$ from statistical samples, at high redshift, the number density of [C II] emitters represents an uncharted territory. To study their LF is crucial to constrain the semi-analytical models and cosmological zoom-in simulations (e.g., Pallottini et al. 2019). Furthermore, it is also pivotal for quantifying the SFRD at high redshift with an unbiased tracer that is not affected by obscuration.

This Chapter is organized as follows. In Sect. 2.2, we briefly describe the ALPINE data and the ancillary photometry. In Sect. 2.3, we present the search for the serendipitous lines and the fidelity and completeness assessment. Sect. 2.4 is devoted to the identification of the lines. In Sect. 2.5 we show the [C II] LF and compare it with other observational studies and models predictions. Finally, Sect. 2.6 deals with the cosmic SFRD.

Throughout this Chapter, we adopt a ΛCDM cosmology using $\Omega_{\Lambda} = 0.7$, $\Omega_{M} = 0.3$ and $H_0 = 70$ km s^{-1}Mpc^{-1}. We assume a Chabrier (2003) initial mass function (IMF).

2.2 Data description

2.2.1 ALMA datacubes

The ALPINE observations were carried out using ALMA band 7 during Cycles 5 and 6 for a total of ~ 70 hours (including overheads). Two frequency settings were adopted to observe two redshift windows at $4.40 < z < 4.58$ and $5.13 < z < 5.85$. The achieved noise is, on average, 0.14 Jy/beam $\mathrm{km\,s^{-1}}$ over a line width of 235 $\mathrm{km\,s^{-1}}$ and 39 μJy/beam over the continuum. The data reduction and processing was handled with the software *CASA* (see Béthermin et al. 2020 for a full description). The visibilities were imaged using a natural weighting of the uv plane, as the best compromise between spatial resolution and sensitivity. We used a pixel size of 0.15" and an image size of 256×256 pixels in order to properly sample the primary beam (~ 21" at 300 GHz). The final 118 datacubes have a channel width varying from 26 $\mathrm{km\,s^{-1}}$ (highest frequency setting) to 33 $\mathrm{km\,s^{-1}}$ (lowest frequency setting). The average spatial resolution is 0.85" $\times$ 1.13". The total area covered by each pointing is 0.41 arcmin^2. However, in order to guarantee an adequate sensitivity, we limited the search of the serendipitous lines to a smaller area (see Sect. 2.3.2 for the details). We also excluded a circle of 1" radius around the phase center to avoid the emission due to the central UV targets. This entails a final effective area of 27.42 arcmin^2 (0.23 arcmin^2 per pointing) where the serendipitous sources can be detected[2].

2.2.2 Ancillary photometry

Since ALPINE observed extensively studied fields, all the sources located in the 118 pointings benefit from a wealth of multiwavelength ancillary data (see Faisst et al. 2020 for a comprehensive description). The UV to near–infrared photometry is widely covered by the COSMOS–2015 and 3D–*HST* catalogs (Laigle et al. 2016; Brammer et al. 2012) and *HST* imaging (Koekemoer et al. 2007, 2011). These catalogs also contain estimates of the photometric redshifts, which were used to guide the line identification (see Sect. 2.4). In addition, for the two fields there are also *Spitzer*–IRAC images at 3.6, 4.5, 5.8 and 8 μm (Capak et al. 2012; Ashby et al. 2013; Guo et al. 2013; Sanders et al. 2007; Laigle et al. 2016), MIPS (Dickinson et al. 2003; Le Floc'h et al. 2009) and *Herschel* data (Lutz et al. 2011; Elbaz et al. 2011). Also *Chandra* data are available for the sources located in the COSMOS field (Marchesi et al. 2016). Finally, at the longest wavelengths, deep JVLA observations at 3 GHz provide estimate of the radio continuum (Smolčić et al. 2017).

2.3 Search for serendipitous lines in ALPINE

We exploited the ALPINE datacubes to look for emission lines detected by chance in the 118 ALMA pointings. We saw in Chapter 1 that using serendipitous lines is particularly useful to perform statistical studies (e.g., LFs) as these sources do not suffer from selection biases. However, we will discuss that this is not exactly our case,

---

[2]We note that this survey area is higher than the area reported by Béthermin et al. 2020 since we included in our estimate a region where the primary beam attenuation reaches the 90%, while in Béthermin et al. 2020, the 80% region has been considered.

as we found strong clustering around the central ALPINE targets that impacts the statistics of serendipitous sources (see Sect. 2.4).

2.3.1 Code description

We performed the search for the serendipitous lines using *findclumps* (Decarli et al. 2016), a code designed to look for sources without any prior knowledge of their frequency or spatial position, which have already been exploited in the ASPECS survey (e.g., Walter et al. 2016; Decarli et al. 2019b). The robustness of this line search method has been successfully tested by González-López et al. (2019); see their work for details. In short, the algorithm performs a floating average of the channels over a range of kernels (number of channels) and searches for peaks exceeding a given signal-to-noise ratio (S/N). The latter is defined as the peak flux density as measured in the averaged map divided by the root mean square (RMS) computed within the entire map.

We executed the search on the 118 ALPINE datacubes adopting a S/N threshold of 3. For each pointing the search was repeated on datacubes of different channel width, from ~ 90 km s^{-1} to 550 km s^{-1}, since these values are compatible with the typical widths of mm-lines at high-z (Capak et al. 2015; Aravena et al. 2019). The probability of a detection is indeed maximized when the channel width is on the order of the full-width at half-maximum (FWHM) of the line, while it is lowered when the channel width is larger or narrower.

After the search, we removed the double detections from the output list, that is, all the peaks at a distance lower than the beam size and in contiguous channels for each detection. We also repeated the search after subtracting the continuum for the lines for which its emission was also detected in order to obtain the S/N referring to the line emission only (for the continuum source-detection method, see Béthermin et al. 2020). Moreover, for those lines detected in datacubes with different channel widths, we considered the detection with the highest S/N as the final entry for our catalog. In this way, we obtained the final list of the line candidates, where a mixture of real lines and spurious detections (i.e., noise peaks exceeding the S/N threshold) is expected.

2.3.2 Fidelity

In order to disentangle the genuine lines from the noise peaks in the output list, we compared the number of the positive peaks detected in the datacubes (i.e., real lines and noise peaks) with the number of negative peaks above the threshold as a function of the S/N. Unlike the positive ones, the negative peaks indeed provide the distribution of the pure noise of our data. This comparison provides the fidelity, that is, the probability that one detection is a genuine line. Following the approach of Decarli et al. (2016), we defined the fidelity f as:

$$f(S/N) = 1 - \frac{N_{\mathrm{neg}}(S/N)}{N_{\mathrm{pos}}(S/N)}, \qquad (2.1)$$

where N_{neg} and N_{pos} are the number of negative and positive peaks, respectively. Defined in this way, the fidelity looks like a function of solely the S/N of a detection. We note that, in principle, there are other factors that could influence it. For instance, the fidelity could be also a function of the line width since, for two detections of equal S/N, a larger line has a higher fidelity than a narrower one (see González-López et al.
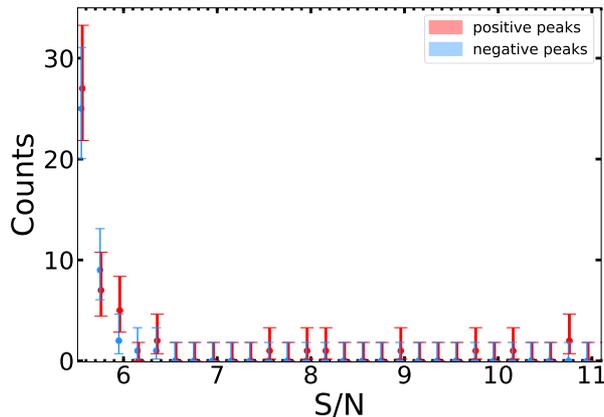
Figure 2.2: Number of positive (red) and negative (i.e., noise; blue) peaks detected in the 118 ALPINE pointings as a function of the S/N. The errorbars are the Poissonian uncertanties. We can see that for S/N > 5.8 the number of positive peaks becomes higher than the number of the negative ones as the number of genuine detections with regard to spurious sources increases. We note that there are two positive peaks with S/N = 28.18 and S/N = 15.97 detected in the 118 pointings (see Fig. 2.7), which are out of scale of this plot.

2019). Moreover, the fidelity can also depend on the line location in the field of view (FOV) since the sensitivity within the primary beam is not uniform. However, because of the low statistics of the positive and negative peaks above S/N = 5.6 (below ten counts per bin even considering the 118 pointings; see Fig. 2.2), it was not possible to split the peaks in sub-samples based on their distance from the pointing center and their width. This S/N range is indeed crucial for assessing the fidelity, as the number of genuine detections starts to be significant compared to the noise peaks at S/N~ 5.8 (Fig. 2.2). We thus consider only one fidelity curve that is valid for the entire sample (Fig. 2.3). We note that the curve was computed after having excluded the peaks located in the regions with a primary beam attenuation larger than 90% as we do not expect sources at those radii. We also excluded the region within 1" from the phase center to remove the positive peaks due to the central targets. The inclusion of the central targets would bias indeed the fidelity to higher values. We note that the fidelity is very steep, jumping from 0.2 to 0.8 in a narrow range of S/N.

We used the fidelity to define the final catalog of the serendipitous lines. The fidelity threshold adopted at this step is crucial since the fraction of genuine detections in the final catalog depends on it. We included the lines with a fidelity higher than 85% (corresponding to a S/N = 6.30 cutoff), that is, there is a very low probability that they are spurious sources (see also the results of González-López et al. 2019; Decarli et al. 2020). This sample includes 12 robust line detections, with 10/12 sources with fidelity equal to unity. We added two more lines with lower fidelity (~ 50%, corresponding to S/N~ 5.98) based on the fact that they present an optical/NIR counterpart[3] (see Sect. 2.4). This provides a final catalog of 14 robust serendipitous line detections over the entire ALPINE pointings.[4] We note that the possibility that a (low) fraction of

---

[3]We note that in addition to present a counterpart, one of the sources with fidelity ~ 50% (i.e., S460378, see Table 2.3) has been detected also in continuum with high significance (Béthermin et al. 2020), so despite its low fidelity, it is likely to be associated to genuine emission.

[4]We note that among the detections in the final catalog, there is one source (S848185, see Table 2.1) that is located at the periphery of the primary beam, i.e., in a region with very poor sensitivity
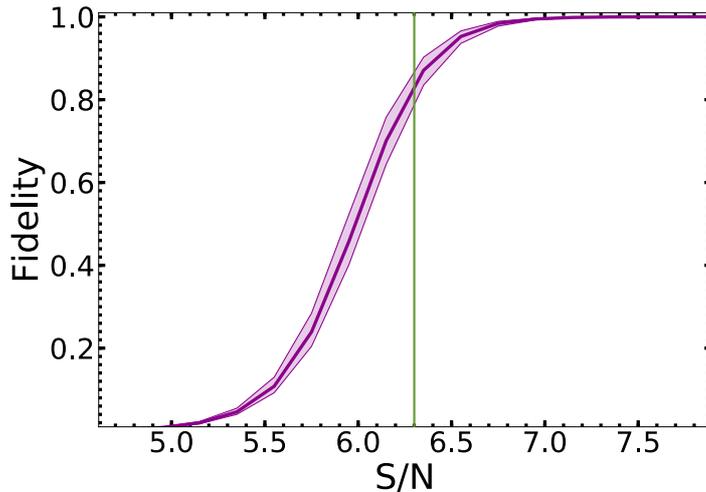
Figure 2.3: Fidelity curve (purple solid line) for the serendipitous lines detected in ALPINE. The shaded area corresponds to the 1σ errorbars. The fidelity was computed by comparing the number of positive (genuine lines and noise peaks) and negative (only noise) peaks detected in the 118 ALPINE pointings. We see that the fidelity is a very steep function of the S/N. We adopted a fidelity threshold of 85% (corresponding to a S/N cutoff of 6.3; green vertical line) for the final catalog of the serendipitous lines.

spurious sources with fidelity < 1 entering our sample does not constitute a problem in the computation of the [C II] LF, as each line is weighted by its fidelity value (see Sect 2.5).

It is equally true that the adopted fidelity cut certainly excludes some genuine detections with low S/N from our catalog. Indeed, if we push the fidelity down to 20% (S/N = 5.69), we find ten more sources. According to their fidelity, we expect that the fraction of true sources is low ($\sim 30\%$). However, their exclusion could have an impact on the derivation of the LF (see Sect. 2.5). We address this point in Sect. 2.5.

2.3.3   Completeness

Given the purpose of the present analysis, we need to also estimate the completeness of the sample, that is, the fraction of recovered lines with respect to the underlying population. We assessed the completeness by simulating ~ 50000 Gaussian-like lines with various peak flux F and FWHM and by injecting them in datacubes containing pure noise representative of the survey (0.14 Jy/beam km s^{-1} over a line width of 235 km s^{-1}). We injected the lines in random locations in the FOV and along the spectral axis, splitting them in groups of 15 lines per datacube in order to not artificially increase the source confusion. We simulated point sources (0.78" $\times$ 1.16") since the sources in our catalog are point-like or marginally resolved. However, we note that recent studies reported the existence of extended [C II] structures (e.g., Fujimoto et al. 2019, 2020; Ginolfi et al. 2020a,b), which may cause incompleteness for some faint objects (see Fig. 5 in Fujimoto et al. 2017). The simulated FWHM range is between 50 and 550 km s^{-1}, while the peak flux varies between 1.0 mJy/beam and 12 mJy/beam in order

---

($\lesssim 20\%$). Despite this, the high S/N (~ 16) of the detection makes it one of the most reliable sources in our sample.
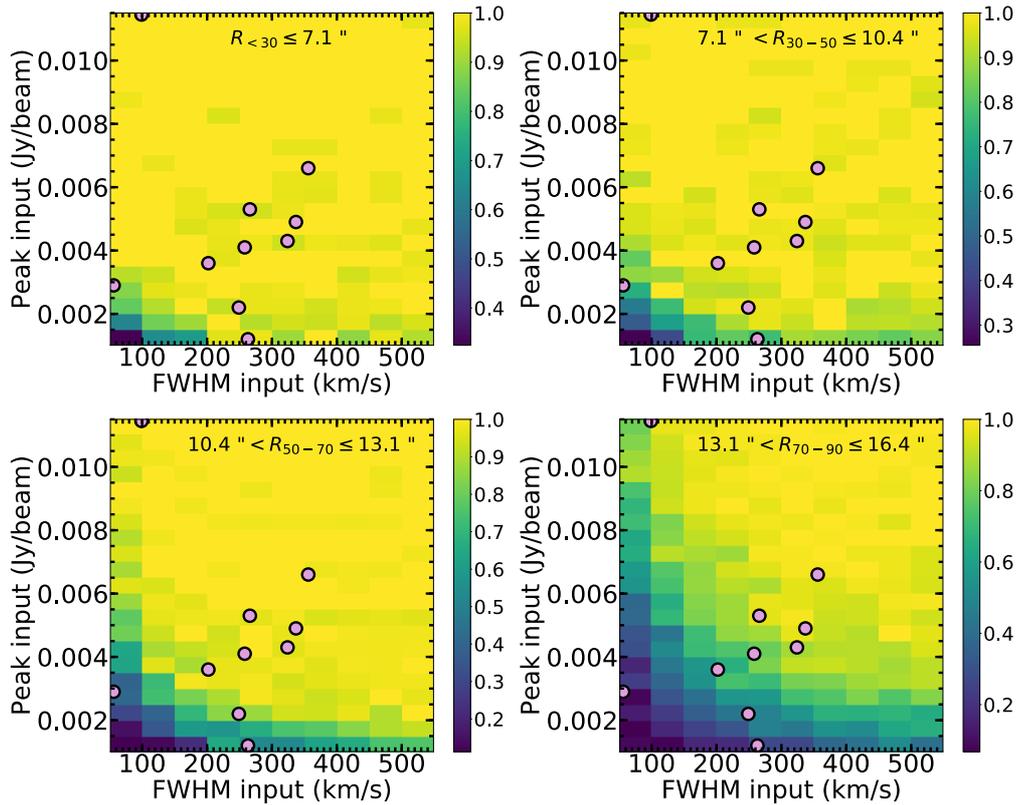
Figure 2.4: Completeness (color scale) as a function of the flux peak and the FWHM of a line. The four diagrams correspond to the $R_{<30}$, R_{30-50}, R_{50-70}, and R_{70-90} regions respectively. As is evident from their comparison, the completeness is a strong function of the line location in the FOV because of the degrading sensitivity from the phase center to larger radii. The lines used to build the [C II] LF (see Sect. 2.5) are also shown (filled circles), except for the two brightes ones (i.e., S848185 and S842313), which are located outside the plotted ranges and have completeness equal to 1 everywhere in the FOV. We show the [C II] serendipitous detections in all the panels, independently from the line location in the FOV, since we computed their completeness in each ring when building the LF (see Eq. 2.3).
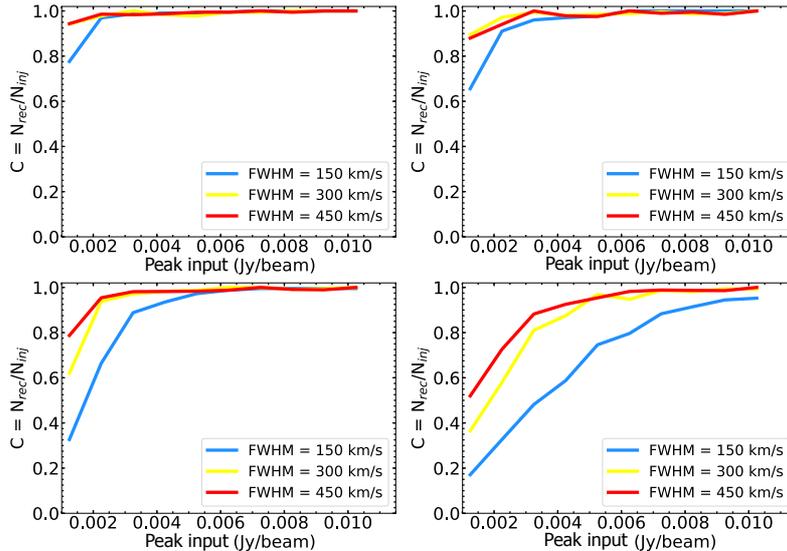
Figure 2.5: Completeness curves as a function of the flux peak for fixed FWHM in four regions with radii $R_{<30}$ (distance from the phase center $R_{<30} \leq 7.1$"), R_{30-50} (7.1" $< R_{30-50} \leq 10.4$"), R_{50-70} (10.4" $< R_{50-70} \leq 13.1$"), R_{70-90} (13.1" $< R_{70-90} \leq 16.4$"), defined on the basis of the primary beam attenuation. The curves correspond to 150, 300, 450 $\mathrm{km\,s^{-1}}$ (reported in blue, yellow and red respectively). We can see that completeness is a strong function of the line location and width.

to widely sample the parameter space of the detected lines (see Fig. 2.4). In particular, for each line the primary beam attenuation is taken into account, that is, its peak flux is lowered based on the primary beam response depending on its spatial position. We hence derived the completeness C in the $j-$th cell of the (FWHM, F) grid as:

$$C^j(\mathrm{FWHM}, F) = \frac{N_{\mathrm{rec}}^j(\mathrm{FWHM}, F)}{N_{\mathrm{inj}}^j(\mathrm{FWHM}, F)}, \qquad (2.2)$$

where N_{inj}^j and N_{rec}^j are the number of the injected lines and of the lines recovered by *findclumps* in the cell respectively. We considered cells of 50 $\mathrm{km\,s^{-1}}$ and 0.5 mJy/beam width. This cell size allows us to accurately evaluate the completeness, with an average number of 60 lines in each cell. We note that completeness is a strong function of the line location in the FOV since the sensitivity decreases significantly as the distance from the phase center increases. We thus evaluated it locally, splitting the lines in four regions based on the primary beam response. In particular, we defined four rings with radius $R_{<30}$, R_{30-50}, R_{50-70}, and R_{70-90}, in which the primary beam attenuation goes from zero to a 30% (distance from the phase center $R_{<30} \leq 7.1$"), from 30% to 50% (7.1" $< R_{30-50} \leq 10.4$"), from 50% to 70% (10.4" $< R_{50-70} \leq 13.1$"), and from 70% to 90% (13.1" $< R_{70-90} \leq 16.4$"). We computed the completeness for each of these regions. We avoided the separation in narrower rings since it would have implied a poor statistics of fake sources to adequately sample the completeness.

The diagrams showing the completeness in the four rings are presented in Fig. 2.4. It seems clear from the plots that, for equal FWHM and peak flux, lines that are easily detected close to the phase center may become more difficult to detect when observed in the outskirts of the FOV. In addition, at a fixed flux peak, the completeness is higher for larger lines. We also show the location of the lines used to build the [C II]

Figure 2.6: Images cutouts of the 12 serendipitous lines used to build the [C II] LF. The *HST*-ACS 0.78 μm (Koekemoer et al. 2007, 2011) and *Spitzer*–IRAC 4.5 μm (Capak et al. 2012) are reported. The white contour shows the [C II] emission in steps of 2σ (lowest level at 3σ). We indicate with a white cross the location of the serendipitous detection while the red cross shows the position of the central target. We can see that for 6 out of 12 lines the distance between the central target and the serendipitous line is < 3", hence, there is a possibility that we are witnessing interacting systems. For S5100822662, the [C II] emission is blended with that of the central target.

LF (see Sect. 2.5.1 and Table 2.1) in the parameter space (FWHM, F). All the lines have a completeness higher than 95% in the two most internal regions except for two cases that have completeness between 90% and 70%. In the remaining less sensitive rings the completeness is still higher than 65% in all the cases except for three sources with completeness values below 50%. This fact guarantees that we applied minimal completeness corrections to our lines when evaluating the LF (see Sect. 2.5).

We present also the completeness curves as a function of the flux peak for fixed FWHM (Fig. 2.5). We can see that at fixed flux peak the completeness is obviously higher for larger lines.

2.4 Identification and sources properties

In order to identify the detected lines, we cross–matched their spatial position with the entries in the COSMOS–2015 and 3D–*HST* photometric catalogs (Brammer et al. 2012; Laigle et al. 2016). The astrometry offsets between these catalogs and the ALMA maps

Table 2.1: Catalog of the serendipitous line emitters in ALPINE (confirmed and candidates; the latter are marked with an *). The sources names are labeled according to the ID number of the UV target in the same pointings, preceded by the letter "S" that stands for "serendipitous". The reported parameters were estimated using a Gaussian fit (see Fig. 2.7) to the line emission. Also, the RA and Dec coordinates, the de-convolved sizes, and the distance from the central target (in arcsec) are reported. We show also the redshift separation Δz between the central target and the serendipitous [C II] line in the same pointing (see Sect. 2.4.2). The only galaxy in the "field" sample is S510327576 (see Sect. 2.5). The continuum flux density was measured by Béthermin et al. (2020). We report also the two CO line detections.

ID	Line	RA (deg)	Dec (deg)	S/N	Frequency (GHz)	FWHM (km s⁻¹)	Line flux (Jy km s⁻¹)	Continuum flux (mJy)	Optical/NIR counterpart	Ancillary redshift	z_{line}	$|\Delta z|$	log L_{line} (L⊙)	Size (arcsec)	Fidelity	Distance (arcsec)
S842313	[C II]	150.22704	2.57671	28.18	343.124	889 ± 35	8.45 ± 0.29	8.24 ± 0.09	yes	spec-z	4.5389 ± 0.0001	0.0148	9.72	0.89" × 0.45"	1.00	1.17
S848185	[C II]	150.08626	2.58895	15.97	301.839	472 ± 20	11.57 ± 0.65	5.983±0.227	yes	spec-z	5.2965 ± 0.0002	0.0034	9.96	0.91" × 0.61"	1.00	15.17
S665626	[C II]*	150.3076	2.31126	10.76	340.752	324 ± 19	1.47 ± 0.12	0.392±0.087	no	...	4.5775± 0.0001	0.00020	8.96	0.66" ± 0.46	1.00	6.35
S5101209780	[C II]	150.38937	2.36906	10.66	341.275	356 ± 19	2.50 ± 0.18	...	yes	photo-z	4.5686± 0.0001	0.0014	9.19	1.65" × 1.26"	1.00	1.64
S818760	[C II]*	150.47784	2.54207	10.25	341.450	202 ± 12	0.78 ± 0.06	0.425±0.104	no	...	4.56609± 0.00008	0.0048	8.69	not resolved	1.00	2.73
S787780	[C II]	149.98694	2.4967	9.02	344.866	258 ± 14	1.13 ± 0.08	0.398± 0.106	yes	spec-z	4.51095± 0.00009	0.00005	8.84	not resolved	1.00	2.49
S510327576	[C II]	150.11117	1.78692	8.14	355.894	337 ± 23	1.75 ± 0.16	...	yes	photo-z	4.3405± 0.0002	0.2194	9.00	1.1" × 0.84"	1.00	7.15
S873321	[C II]	150.01341	2.62712	8.0	308.730	266 ± 39	1.50 ± 0.29	...	yes	spec-z	5.1560± 0.0003	0.0018	9.05	1.26" ± 0.44"	1.00	12.69
S378903	[C II]	150.29589	1.86892	7.5	295.858	249 ± 26	0.58±0.08	...	yes	photo-z	5.4238±0.0002	0.0059	8.67	not resolved	1.00	6.50
S510822662	[C II]*	149.74141	2.08131	6.39	344.256	56 ± 7	0.17 ± 0.03	...	no	...	4.52071± 0.00004	0.00021	8.02	not resolved	0.89	1.32
S859732	[C II]*	149.9989	2.60632	6.34	343.096	99 ± 15	1.21 ± 0.24	...	no	...	4.5393± 0.0001	0.0075	8.87	not resolved	0.86	12.07
S5100969402	[C II]	150.33384	2.28427	5.99	340.402	263 ± 38	0.32± 0.06	...	yes	photo-z	4.5832± 0.0002	0.0047	8.30	not resolved	0.51	2.31
S5110377875	CO(7–6)	150.38494	2.40665	9.85	354.109	183 ± 9	1.35± 0.09	3.512 ± 0.163	yes	photo-z	1.27793 ± 0.00002	...	7.60	0.88" ± 0.59"	1.00	6.53
S460378	CO(5–4)	150.04929	1.9996	5.97	295.935	855 ± 102	1.11 ± 0.18	0.680 ± 0.117	yes	photo-z	0.9472 ± 0.0001	...	7.12	not resolved	0.48	7.99

are on the order of 0.1" (Faisst et al. 2020). In addition, we checked for counterparts also in the SPLASH (Capak et al. 2012), UltraVista-DR4 (McCracken et al. 2012), 24 μm–selected (Le Floc'h et al. 2009) and 3 GHz-selected JVLA catalogs (Smolčić et al. 2017). Moreover, we also visually inspected the images from UV to mid–infrared (MIR) wavelegths in order to look for faint emissions not reported in the catalogs. We classified a galaxy as a physical counterpart of a serendipitous line if their spatial distance is less than 1". The choice of this value derived from the distance distribution between the serendipitous lines and all the galaxies lying within 10", which clearly presents a minimum for a distance $\sim$ 1" for all the catalogs.

Based on the photometric or spectroscopic redshift available, we identified eight lines as [C II] and two lines as $CO(J_{up} = 7, 5)$ transitions. The remaining four detections have an ambiguous identification because of the lack of an optical/NIR or uncertain photometric redshift from ancillary data[5]. All the images and spectra of the serendipitous lines are reported in Figure 2.7. We refer to a future paper for an analysis of the CO emitting galaxies (Loiacono et al., in prep.). Hereafter, we focus on the [C II] emitters and on the ambiguous lines (i.e., 12 objects in total).

2.4.1 [C II] serendipitous emitters at $4.3 < z < 5.4$

We identified eight lines as [C II] based on the photometric or spectroscopic redshift of the optical/NIR infrared counterpart available from ancillary data. Namely, four out of eight detections have an UV-optical spectroscopic redshift (M. Salvato, private communication; Capak et al. 2008, 2011). The remaining four sources have photometric redshifts compatible with [C II] emission (Laigle et al. 2016). The sources have redshift of $4.3 < z < 5.4$, which is as expected given the spectral coverage of ALPINE. We note that among the serendipitous [C II] emitters, we recovered the well-studied sub-mm galaxies of AzTEC–C17 (referred to here as S842313; Laigle et al. 2016; Schinnerer et al. 2008; Jones et al. 2017) and AzTEC–3 (S848185; Capak et al. 2011; Riechers et al. 2010, 2014).

In addition to these eight detections, we found four lines whose identification based on the available photometry is ambiguous. Two of them (S818760 and S859732) do not present any counterpart in the available catalogs or in the multiwavelength images (from UV to MIR). The lack of counterparts suggests that these emissions are produced from highly dusty and high-z sources or from gas-rich galaxies with low stellar masses. The most likely associations are thus [C II] at $4 < z < 6$ or CO transitions at lower redshifts. However, S818760 is located within 3" and has a velocity separation of < 300 km s^{-1} from the central target in the same pointing (see Fig. 2.6). As a consequence, it is very likely that it is produced by a companion or interacting source with the UV-target emitting [C II] but also proving to be optically faint (see also Jones et al. 2020). A similar argument applies to S5100822662[6]. We note that the narrow FWHM of this

---

[5]We note that if we consider the sources with a fidelity down to 20%, nine out of the ten new sources do not show any optical/NIR counterpart. There is only one detection associated to a galaxy with a photometric redshift that makes the line emission compatible with a CO(4–3), CO(5–4) or [C I] transition.

[6]We note that this particular source was included also in the LF of Yan et al. (2020), as they used the total flux of the central target vuds cosmos 5100822662 (see also Fig. 2.6), which was not deblended from the serendipitous companion (see Béthermin et al. 2020). However, since the latter respects the criterion to be a non-target source (i.e., distance from the phase higher than 1"), we included it in our calculations. We note that its exclusion from our sample does not alter the result
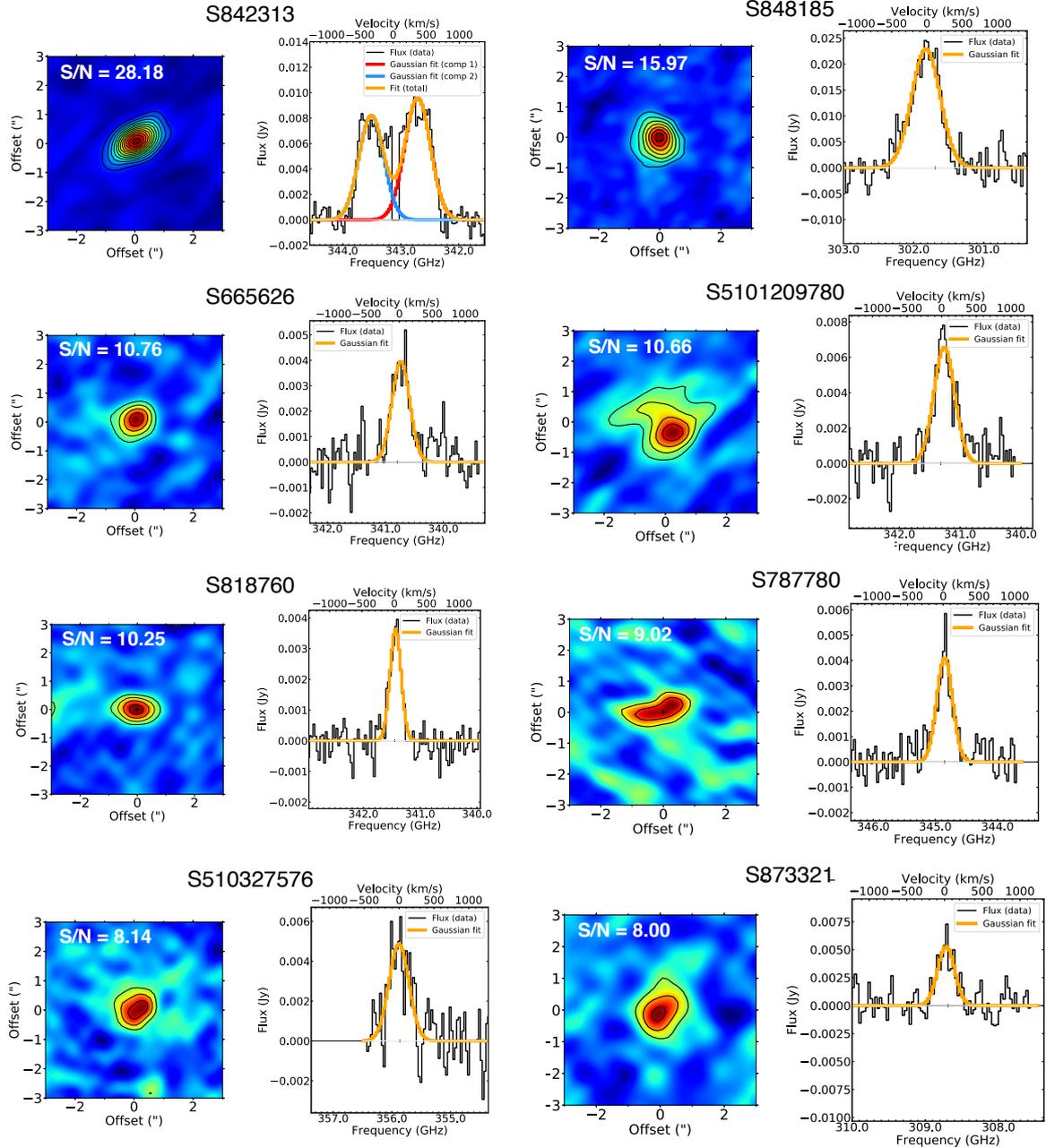
Figure 2.7: Continumm-subtracted ALMA maps and spectra of the 14 serendipitous lines found in the 118 ALPINE pointings. Each panel is labeled according to the number of the ALPINE source in the same pointing. We report the contours in steps of 2σ. The lowest level corresponds to 3σ. We fitted the line emission (black) using a sigle Gaussian component (orange). In the case of S842313, we fitted the line profile using two Gaussian components (cyan and red); the total model is shown in orange. For S5100822662, the serendipitous source is the small blob above the ALPINE target. The blob is marked with a cross and we present a spectrum extracted from its peak spaxel.

28
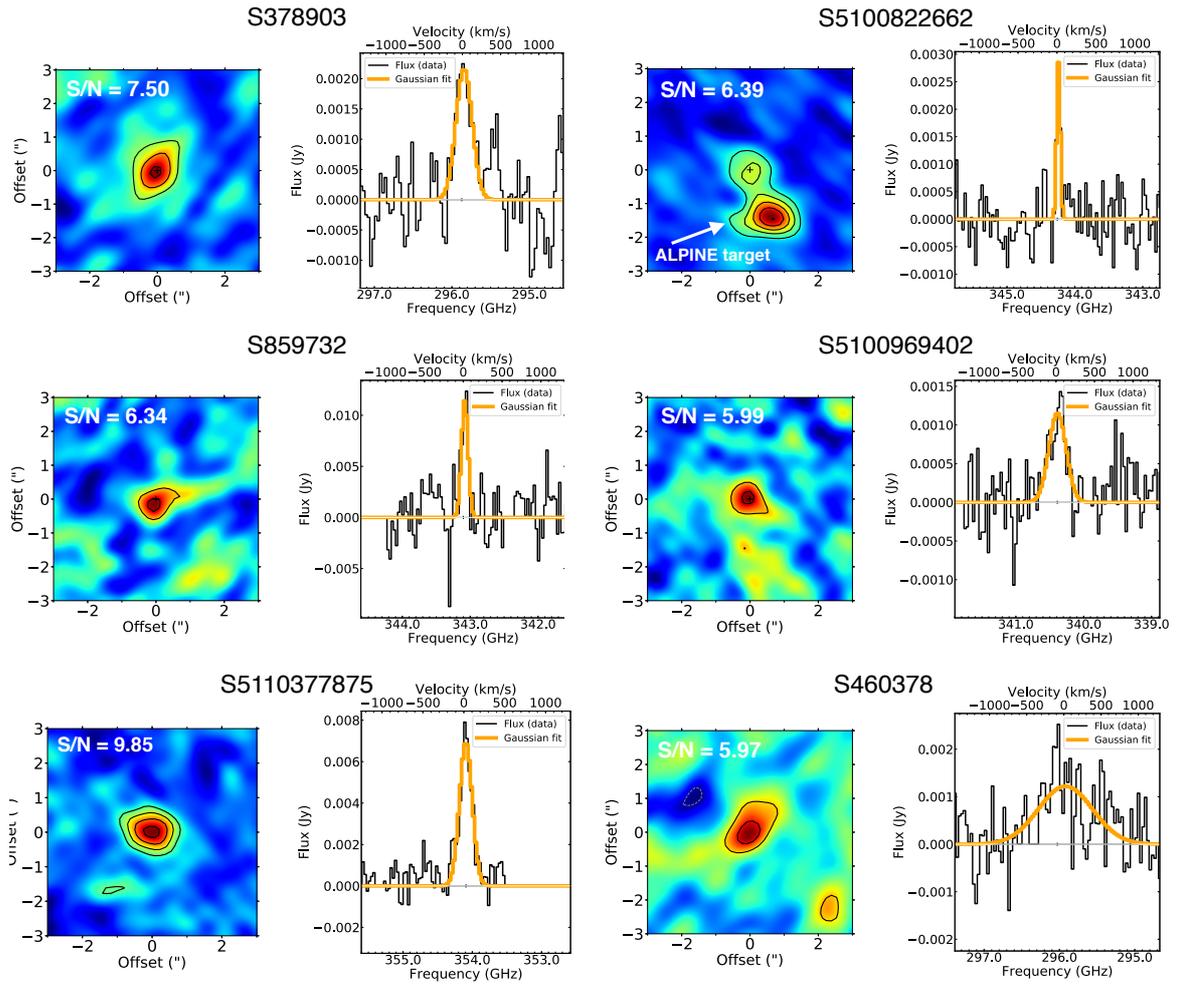
Figure 2.7: (continued) Continumm-subtracted ALMA maps and spectra of the 14 serendipitous lines found in the 118 ALPINE pointings.

line (~ 50 km s^{-1}, see Table 2.3 and Figure 2.7) could be suspicious and indicative of a spurious line, despite the high fidelity (89%) of the detection. However, this source has been detected in two independent ALPINE pointings targeting the same galaxy (i.e., vuds cosmos 5100822662 and DEIMOS COSMOS 514583, see Béthermin et al. 2020 for the details) so the notion that the spurious emission is due to a noise peak is very unlikely. Moreover, S5100822662 is detected in the multiwavelength photometric images (see Fig. 2.6), suggesting that the detection is indeed genuine. Based on the Laigle et al. (2016) catalog, it has a photometric redshift of 0.69. However, the strict association with the ALPINE target in the same pointing (Fig. 2.6) favors a high-z interpretation for this source with the ALMA emission likely due to the [C II] line. We also cannot rule out that the emission in the photometric images is produced by a foreground source that is not related to the ALMA detection (see also Pavesi et al. 2018a). Finally, S665626 does not present any counterpart in any other band apart from K–band UltraVista image (Romano et al. 2020). This source was studied in detail by Romano et al. (2020) and their modeling seems to favor a [C II] interpretation rather than a CO line. Follow-up observations are needed to unambiguously confirm the nature of these four sources.

In the rest of this thesis, we assume that the four unidentified lines are due to [C II] emission. We used both them and the confirmed [C II] to build the LF (Sect. 2.5). We note that the exclusion of the unidentified lines from it does not alter significantly any of the results. The optical/NIR images of the 12 serendipitous [C II] lines (confirmed and candidates) are shown in Fig. 2.6.

We estimated the main properties of the [C II] lines (i.e., frequency, FWHM, total fluxes) by performing a single-component Gaussian fit to the continuum subtracted spectrum, with the exception of source S842313, where two Gaussians were adopted to model the line profile (Fig. 2.7) as it shows signs of rotation (Jones et al. 2017; see also Sect. 2.4.2 for further details about this source). To compute the line flux, we used the peak flux if the source size is comparable with the beam or we extracted it from a 3σ aperture in case the emission is resolved. To distinguish between resolved and unresolved sources, we compared the number of pixels within a 3σ aperture with the beam size in pixels. In case the number of pixels exceeds the beam size, we labeled the source as resolved. Otherwise, we considered the source as not resolved. We note that this procedure gives consistent results with an independent measurement of the sources sizes obtained with the 2D fitting tool of *CASA*, which performs a deconvolution of the line with the beam and returns the deconvolved sizes of the resolved sources.

We also measured the line fluxes on the moment zero maps, but we do not report them here since they show consistent results.

All the fitted values are reported in Table 2.1.

2.4.2 Overdensities around the central UV-targets

The detection of eight confirmed [C II] lines in targeted [C II] observations of $4 < z < 6$ galaxies suggests that we are witnessing possible overdensities around the central UV-selected galaxies. This is highlighted by the velocity separation Δv between the central target and the serendipitous line in the same pointing. Indeed, seven out of eight [C II] lines have $|\Delta v| < 750$ km s^{-1}, corresponding to a redshift separation $|\Delta z| < 0.0154$.

---

significantly.

Such a velocity difference suggests that the two galaxies in the same pointing could be physically connected or associated to the same large-scale structure. An extended protocluster at $z \sim 4.5$ (PCI J1001+0220) in the COSMOS field was discovered by Lemaux et al. (2018). Capak et al. (2011) found another protocluster of galaxies in COSMOS at higher redshift ($z \sim 5.3$; AzTEC–3 protocluster). In fact, some of the serendipitous lines in our sample (e.g., S848185) are well known members of these protoclusters. However, there are other detections in our catalog that could constitute potential new members of these protoclusters. This is likely valid for two confirmed [C II] emitters (S5101209780, S5100969402) and one [C II] candidate (S665626) that lie in the spatial region corresponding to PCI J1001+0220 and have a redshift in the range $4.53 < z < 4.6$ (Lemaux et al. 2018, 2020) while other three [C II] lines (two candidates and one confirmed) are possibly located in the outskirts of the same protocluster (Fig. 2.8; see also Ginolfi et al. 2020a). Further observations are necessary to confirm whether these three galaxies on the periphery are part of a greater structure associated with this protocluster. The same applies to the other sources in our sample (S787780, S873321, S378903 and S5100822662) that show a very low velocity separation with the UV-target in the same pointing but at the moment, it is unclear whether they are part of possible unknown protoclusters.

Besides the low velocity and redshift separation, we also see that for four out of eight confirmed [C II] lines, the spatial separation from the central target is less then 3", corresponding to a physical distance of < 20 kpc at $z \sim 5$ (Fig. 2.6). The number of sources increases to six if we include also the [C II] candidates S818760 and S5100822662. These sources are galaxies that are likely interacting with the central targets. This is also suggested from the [C II] morphologies, which appear irregular as we can see for S5101209780 (Fig. 2.6). This source has been found to be part of a merging system of two massive galaxies ($M_\star \gtrsim 10^{10} M_\odot$) including two small satellites (Ginolfi et al. 2020a). Also large FWHM (> 500 km s^{-1}) could be indicative of a merger. This scenario has been indeed suggested to explain the emission of S842313 (FWHM $= 889 \pm 35$ km s^{-1}; see Capak et al. 2008; Schinnerer et al. 2008). However, the regularity of the velocity field suggests that a disc interpretation is favored for this source (Jones et al. 2017).

Therefore, we could be in presence of two kind of overdensities: one on a very small scale (< 20 kpc) due to galaxy pairs or mergers and another on a larger scale (up to ~ 90 kpc, i.e., the maximum distance allowed by the size of our pointings), related to possible more extended structures. We will analyze the overdense environment in more detail in a future paper (Loiacono et al., in prep.). The effect of clustering around the central UV targets has been taken into account when building the [C II] LF (see Sect. 2.5).

2.4.3   Relation between [C II] luminosity and SFR

Within the sample of the serendipitous [C II] lines, there are five sources for which also the continuum has been detected (Béthermin et al. 2020; Gruppioni et al. 2020). It is well known that there is a correlation between the [C II] luminosity and the SFR (De Looze et al. 2014; see also Chapter 1). Since the latter is well-traced by the total IR luminosity (8-1000 μm), we used the five lines to test if this relation is also valid at $z \sim 5$. We included also the two unconfirmed [C II] lines for which the ALMA continuum has been detected (S818760 and S665626).
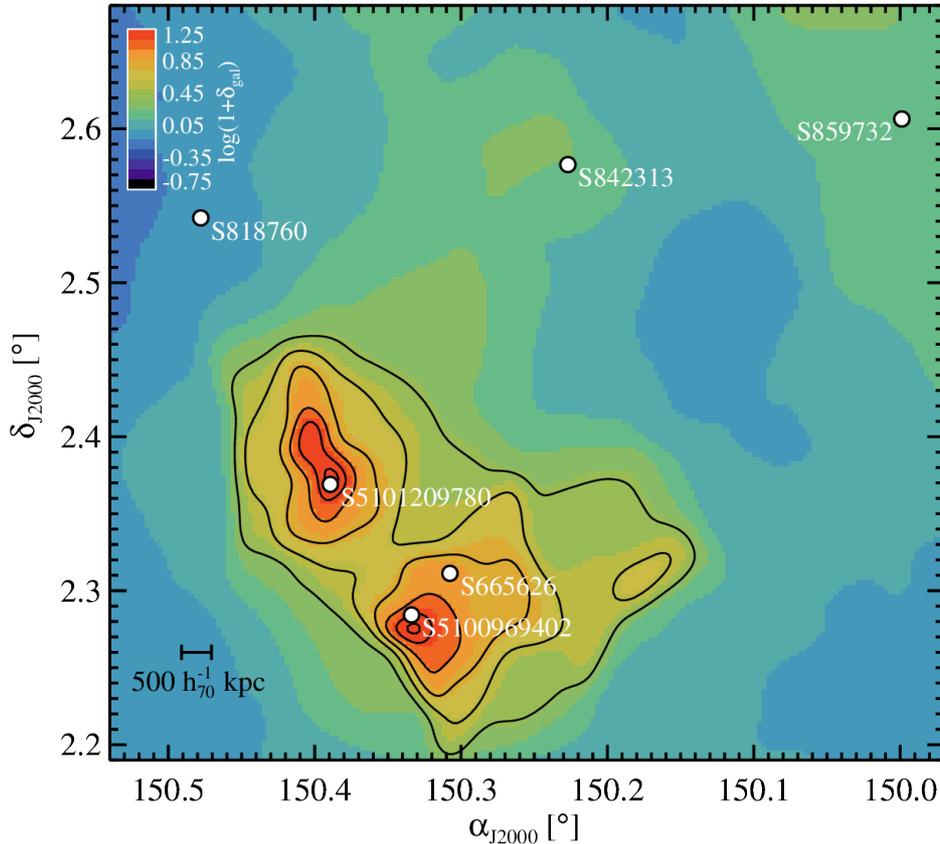
Figure 2.8: Galaxy overdensity map of the PCI J1001+0220 protocluster at $z \sim 4.5$ (Lemaux et al. 2018). The contour levels correspond to 2.5, 3.75, 5, 6.25, 7.5, 8.5σ. We see that three serendipitous sources (S665626, S5101209780 and S5100969402) are clearly associated to the protocluster, as their location is very close to two density peaks. On the other hand, S842313, S818760 and S859732 lie in the periphery of the overdense region of PCI J1001+0220.

The spectroscopic data used to construct this map combines VUDS, zCOSMOS, and followup Keck/Deep Imaging Multi–Object Spectrograph (DEIMOS; Faber et al. 2003) observations. These spectroscopic data are used in conjunction with COSMOS–2015 photometric redshifts (Laigle et al. 2016) to generate the galaxy density map following Monte Carlo Voronoi tessellation technique (see Cucciati et al. 2018; Ginolfi et al. 2020a; Lemaux et al. 2020 for details on the method and data).
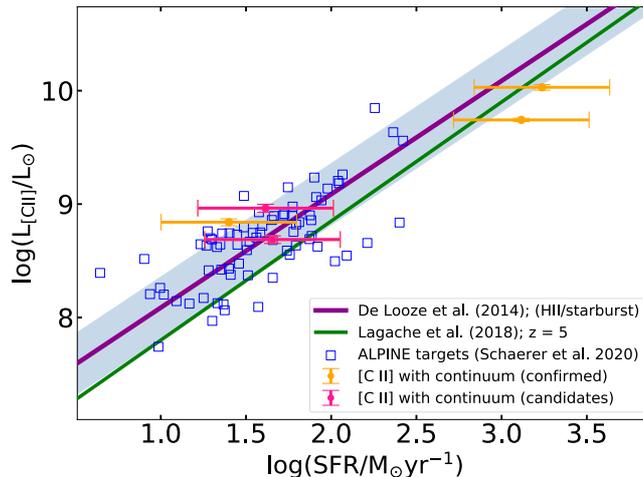
Figure 2.9: SFR–$L_{[C\ II]}$ relation for the five serendipitous lines detected in continuum. The SFR of the serendipitous sources was computed from the IR luminosity. We can see that the sample is quite consistent at 1σ (colored area) with the De Looze et al. (2014) relation (purple line), suggesting that the contribution from the UV–traced SFR is negligible. We compare our results also with the models of Lagache et al. (2018) at $z = 5$ that suggest a slightly different slope. We also show the ALPINE UV–targets from Schaerer et al. (2020). Both the serendipitous sources and the ALPINE targets seems to suggest no evolution of the relation of De Looze et al. (2014).

The [C II] fluxes were converted to luminosities using Eq. 1 from Solomon et al. (1992) and we propagated the errors from the fitted quantities in Table 2.1. The total IR luminosity L_{IR} was estimated from a SED fitting of the galaxies. We assumed the template of a star-forming galaxy that reproduces most of the *Herschel* galaxies at $z \sim 2 - 3$ (Gruppioni et al. 2013). We note that the uncertainty on the total IR luminosity can be up to a factor of 5 depending on the assumed dust temperature (see Faisst et al. 2017; Fudamoto et al. 2020). This uncertainty accounts for about a factor ~ 2.5 on the derived SFR, which we assumed as the typical error of this quantity. Then the L_{IR} was converted to SFR using the Kennicutt (1998a) relation.

If we compare our values with the local relation of De Looze et al. (2014) (see their Table 3, case HII/starburst), we can see that they are broadly consistent within the 1σ errorbars (Fig. 2.9). On the other hand, our points suggest a slightly different slope compared to the model predictions at $z = 5$ of Lagache et al. (2018). The same trend is also shown by the ALPINE targets (Schaerer et al. 2020; Béthermin et al. 2020), which do not present any evidence of evolution of the SFR–$L_{[C\ II]}$ relation between $z \sim 0$ and $z \sim 5$. The only difference is that compared to the central UV-galaxies, the serendipitous sources reach higher SFRs and [C II] luminosities. In addition, we note that the SFR of the ALPINE targets takes into account both the UV and IR estimates; otherwise the UV–targets would not lie on the De Looze et al. (2014) relation (see Schaerer et al. 2020 for the details). On the other hand, we considered the IR-derived SFR only for the serendipitous galaxies. This means that the serendipitous sources detected both in line and continuum have SFRs dominated by the IR emission, with little or negligible contribution from the UV.

Therefore, both the ALPINE targets and the serendipitous sources appear to independently suggest that there is no significant variation of the relation of De Looze
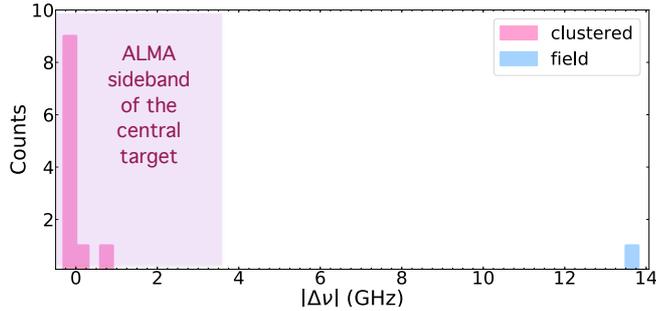
Figure 2.10: Offset in frequency between the central UV target and the serendipitous [C II] in the same pointing. We see that the distribution is non-uniform, with several sources lying at a frequency (and hence a redshift) close to that of the central target. We thus defined two subsamples (named "clustered" and "field," respectively) and evaluated two distinct LFs in order to account for any bias due to overdense regions. The separation between the two sample relies on the frequency width of one ALMA sideband (3.6 GHz), corresponding to a velocity separation $\gtrsim 2000 \, \mathrm{km \, s^{-1}}$.

et al. (2014) up to $z \sim 5$.

2.5 The [C II] luminosity function at $z \sim 5$

2.5.1 Building the LF: "clustered" and "field" sources

The 12 [C II] lines (eight confirmed and four candidates) were used to build the LF. Since their first use by Schmidt (1968), LFs are fundamental tools to explore the global properties of galaxies from the UV to IR/mm wavelengths and their evolution across cosmic time.

We populated each luminosity bin dlogL according to the relation:

$$\Phi(L) \mathrm{d} \log L = \Sigma_j \frac{F_j(\mathrm{S/N})}{\Sigma_k C_j^k(\mathrm{FWHM}, F) V^k(A, z)}, \tag{2.3}$$

where $\Phi(L) \mathrm{d} \log \mathrm{L}$ is the number density of [C II] emitters, F_j and C_j^k are the fidelity and completeness of the j-th source associated to the comoving volume V^k. The latter was evaluated for the regions $R_{<30}$, R_{30-50}, R_{50-70}, and R_{70-90} in order to take into account the completeness variation in the FOV, hence the k index goes by the four rings.

We note that the term $\Sigma_k C_j^k(\mathrm{FWHM}, F) V^k(A, z)$ in Eq. 2.3 corresponds to the maximum volume in which a galaxy could be observed, that is, $V_{\max}$ (Schmidt 1968), due to the variation of the survey sensitivity inside the FOV (see also Riechers et al. 2019). Only the sources with completeness equal to unity everywhere in the FOV could have been observable, indeed, within the total comoving volume V_{TOT} covered by the 118 ALPINE pointings. The total comoving volume was evaluated as $V_{\mathrm{TOT}} = \Sigma_i^{118} A_i \Delta D_c(z_i) = 9810 \, \mathrm{Mpc^3}$, where A_i is the area with a primary beam attenuation $< 90\%$ covered by each ALPINE pointing and $\Delta D_c(z_i)$ is the difference between the comoving distances of the [C II] line at the beginning and at the end of the ALMA sidebands for the i-th pointing. This difference was computed after having excluded three to four channels at the beginning and at the end of each sideband to account for border effect (i.e., noisy channels). We note that we excluded the central $R < 1$"

region from each pointing in the computation of the volume.

Then, as the luminosity bin size, we considered 0.5 dex in order to have at least one source per bin. The adopted bin spacing is 0.25 dex in luminosity. Although the bins are not independent, this choice offers the advantage of better highlighting the luminosity distribution of the sample. We point out that we did not split the [C II] lines in different redshift bins because of the poor statistics, hence, our LF refers to an average redshift $z \sim 5$. As done in Sect. 2.4.3, we evaluated the [C II] luminosities following Solomon et al. (1992) (see Table 2.1 for the values). The errorbars associated to each luminosity bin are computed as the Poissonian uncertainties corresponding to 1σ since the source number in each bin is small (Gehrels 1986), thus constituting the primary uncertainty.

Before computing the LF, we splitted the [C II] lines in two subsamples. As we see in Sect. 2.4, seven out of eight confirmed [C II] have a redshift separation from the central targets in the same pointings $|\Delta z| < 0.0154$ (corresponding to a velocity separation < 750 km s^{-1}). This number increases to 11 out of 12 if we include also the four unconfirmed [C II]. This means that their LF could be not representative of the field galaxy population since it is likely biased by the presence of overdensities around the UV-selected targets. The only exception is S510327576, which has a redshift separation of $|\Delta z| = 0.2195$ ($|\Delta v| \sim 1.2 \times 10^4$ km s^{-1}) and is not, thus, related to the central target. This could be the only [C II] line not associated to clustered structures, that is, the only genuine field source in our sample.

In order to study the effect of clustering on the LF, we thus considered two separate subsamples, each of them containing the lines with a frequency offset from the central target lower or higher than one ALMA sideband ($\Delta \nu \sim 3.6$ GHz; see Fig. 2.10). This separation corresponds to a redshift difference $\gtrsim 0.04$ and to a velocity separation $\gtrsim 2000$ km s^{-1} (see also Hennawi et al. 2010 who used a similar velocity separation in a study on quasars pairs). In this way we defined the "clustered" and "field" subsamples, containing 11 and 1 sources, respectively. Also the survey volume was split consistently, obataining a total comoving volume of 5026 Mpc^3 for the clustered subsample and 4784 Mpc^3 for the field one. Thus we built a separate [C II] LF for each sub–sample (Fig. 2.11 and Table 2.2). The median luminosity of the clustered sample ($\log (L/L_\odot) = 8.96 \pm 0.14$) is very similar to the luminosity of the field one ($\log (L/L_\odot) \sim 9.0$). However, we recall that the field LF is based on one object only and therefore it could also present galaxies at higher luminosity that we do not detect for the limited survey volume. Despite the similar median luminosity, the clustered LF shows objects with luminosity of about one order of magnitude higher than the field.

If this trend were confirmed by a larger sample of galaxies, it would highlight a dependence between clustering and the [C II] luminosity, as has already been shown based with other tracers (e.g., Hawkins et al. 2001).

For completeness, we report also the LFs including sources with a fidelity as low as 20% (see Fig. 2.12, left panel). In Sect. 2.3.2, we cut indeed our catalog of serendipitous detections at a fidelity of 85%, with only one [C II] line (S5100969402) having a fidelity of $\sim 50\%$ in order to study a very robust sample. However this sample is obviously incomplete at low luminosity. We thus calculated the clustered and field LFs for two new subsamples, in which we included also low fidelity (i.e., low luminosity) sources. The fidelity cut of 20% adds nine lines to our catalog of [C II] emitters (we excluded one single source that is possibly associated to CO emission; see Sect. 2.4). We note that none of these lines presents an optical/NIR counterpart, hence their redshift is

Table 2.2: LFs for the clustered and field sample considering the eight confirmed and four candidates [C II]. We reported also the number of sources in each luminosity bin. We indicated with the bold font the values corresponding to independent luminosity bins.

$\log (L/\mathrm{L_\odot})$	$\log (\Phi_{\mathrm{clust}}/\mathrm{Mpc}^{-3}\mathrm{dex}^{-1})$	N_{clust}	$\log (\Phi_{\mathrm{field}}/\mathrm{Mpc}^{-3}\mathrm{dex}^{-1})$	N_{field}
8.25	$\mathbf{-2.94^{+0.36}_{-0.45}}$	**2**	...	...
8.50	$-2.87^{+0.29}_{-0.34}$	3	...	...
8.75	$\mathbf{-2.65^{+0.22}_{-0.24}}$	**5**	...	...
9.00	$-2.69^{+0.22}_{-0.24}$	5	$-3.37^{+0.52}_{-0.77}$	1
9.25	$\mathbf{-3.09^{+0.36}_{-0.45}}$	**2**	$\mathbf{-3.37^{+0.52}_{-0.77}}$	**1**
9.50	$-3.40^{+0.52}_{-0.77}$	1	...	...
9.75	$\mathbf{-3.10^{+0.36}_{-0.45}}$	**2**	...	...
10.00	$-3.40^{+0.52}_{-0.77}$	1	...	...

unconstrained from ancillary data. Therefore, for these sources we can only assume that their emission is due to [C II]. Based on their individual fidelities we expect that only ~ 3 out of the 9 lines are genuine detections, thus this new sample is expected to contain a high fraction of spurious sources. We see that the shapes of both clustered and field LFs remain relatively unchanged, with the field LF sampled by more sources at this point. Also, in this case, the field sources lie at lower luminosities compared to the clustered sample. However, this is not surprising because as the fidelity is reduced, the line flux decreases and, hence, we expect the population of the low luminosity bins only for both field and clustered sources.

Finally, in Sect. 2.4.2 we show that the clustered sources are possibly part of two different types of overdensity – one associated to interactions and mergers (scale < 20 kpc) with the central UV-selected galaxy and the other associated to a more extended structure (up to ~ 90 kpc). In order to overcome the bias introduced by the interacting systems, we excluded from the LF the six sources with a spatial distance of < 3" from the central target (Fig. 2.6). We report the derived LF in Fig. 2.12 (right panel). The new points are consistent within the errors with the LF computed using all the clusterd sources. Overall, the faint end of the LF is lower compared to the case in which all the 11 clustered [C II] are considered. However, this has a negligible effect on the derivation of quantities, such as the fitted parameters of the Schechter function and the SFRD (see Sects. 2.5.3 and 2.6).

2.5.2 Comparison with observations and models

Luminosity functions from ALPINE

In this section, we discuss our LFs in relation to those from other works (Fig. 2.11). Overall, we consider the field LF as representative of the average population of galaxies while the clustered LF is likely biased to an high-density environment that is due to clustering around the central UV targets. The galaxies of the clustered sample are indeed companions of the ALPINE targets (see Sect. 2.5.1), which might not have been observed in a pure blind survey. We remind the reader that the field LF is based on one object only, thus in general our conclusions need to be further constrained by future observations with more galaxies.

We start by comparing our results with the other $z \sim 5$ LFs based on the ALPINE
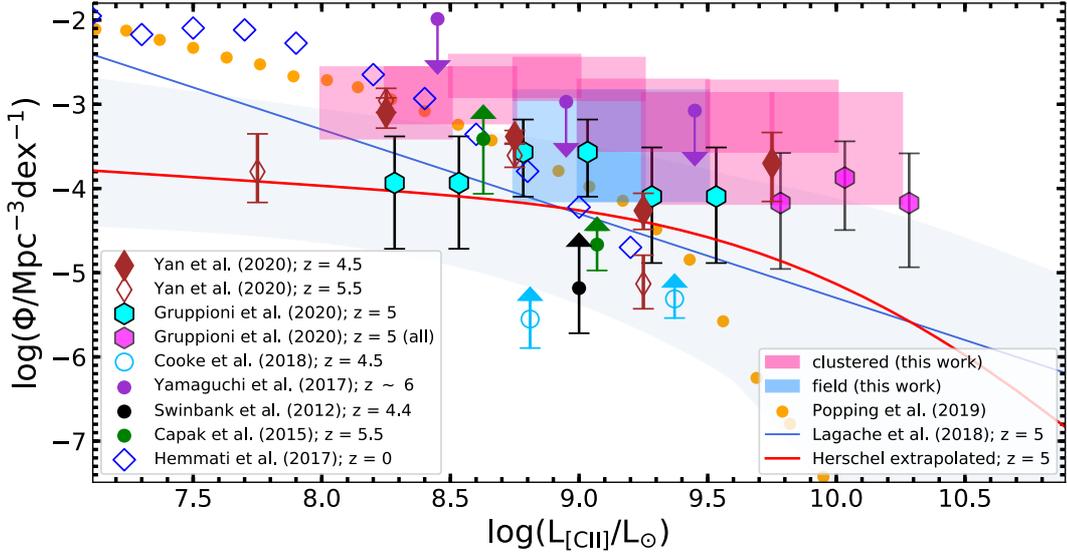
Figure 2.11: [C II] LFs at $z \sim 5$ from the serendipitous sources in ALPINE compared to other works in the literature. We split the lines in two subsamples, called "clustered" (pink) and "field" (azure), respectively, and we built two separate LFs. Compared to the clustered LF, the field one lies at lower luminosities. We compare our [C II] LFs at $z \sim 5$ with other [C II] LFs at high and low-z. Overall, the estimates from the clustered sample lie above the LFs of the ALPINE targets (Yan et al. 2020) likely because they include UV-dark galaxies and because of the clustering effect. On the other hand, the field LF seems to be quite consistent with the targets ones except in the case of the highest luminosity bin. There is agreement between the field [C II] LF and the IR-derived [C II] LF based on the ALPINE serendipitous sources detected in continuum (Gruppioni et al. 2020). The agreement persists at $L_{[C\ II]} > 10^{9.5} L_\odot$ for the clustered sample if the companions of the central targets are included in the IR-derived [C II] LF of Gruppioni et al. (2020). The clustered LF is up to $>$ 1 dex higher than the local [C II] LF (Hemmati et al. 2017). Also the field LF predicts an excess of [C II] emitters at $L_{[C\ II]} > 10^9 L_\odot$, suggesting a possible evolution of the [C II] LF between $z \sim 5$ to $z \sim 0$. The field LF appears in agreement with the models predictions of Popping et al. (2019).
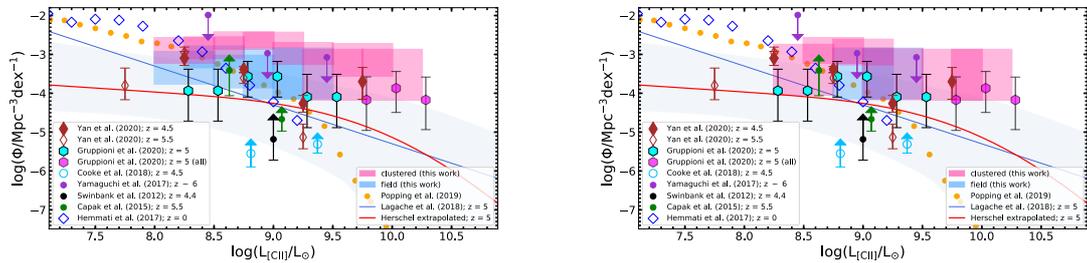
Figure 2.12: [C II] LFs at $z \sim 5$ of the serendipitous sources in ALPINE including the sources with low fidelity (left panel). Compared to the clustered LF, the field one lies at lower luminosity. Both LFs result compatible with those based on the sources with higher fidelity. The main difference is at the low luminosity end since more sources are included in this sample. Right panel: [C II] LF at $z \sim 5$ of the clustered sources after removing the six [C II]–emitters associated to interacting galaxies with the central targets (see Fig. 2.6). Compared to the LF including all the clustered sources, this one results in lower values at the faint end.

data. First of all, we consider the [C II] LFs presented in the companion paper of Yan et al. (2020). These LFs were built using the 75 [C II] central UV targets in the two redshift ranges $4.40 < z < 4.58$ and $5.13 < z < 5.85$. Globally, we see that the clustered LF predicts more [C II] emitters than the Yan et al. (2020) sample. This was expected due to clustering effects and also because the LF of the central targets is based on UV-selected galaxies, hence it is likely to be missing the most obscured galaxies. On the other hand, the field LF is quite consistent with the targets LFs, showing a slight excess in the highest luminosity bin.

Thereafter, we compare our sample with the LF based on the sources serendipitously detected in the rest-frame FIR continuum (Gruppioni et al. 2020; Béthermin et al. 2020). The 118 ALPINE pointings have indeed revealed a wealth of serendipitous continuum emitters across a wide range of redshifts. These sources were used to build a LF at 250 μm (rest-frame) and a total IR LF from $z = 0.5$ to $z = 6$ (see Gruppioni et al. 2020 for details). For the purposes of our comparison, we considered the IR LF in the highest redshift interval $4.5 < z < 6$, where the companions of the central targets have been removed (green water hexagons; see Table 4 of Gruppioni et al. 2020). The IR luminosities (8-1000 μm) were first converted to SFRs according to the Kennicutt (1998a) relation. We note that the computed SFRs do not include the UV contribution, therefore, they can be considered as lower limits. However, we do not expect the UV contribution to be significant since the sources are selected to be dusty (i.e., FIR/sub-mm emitters). The SFRs were then used to derive the [C II] luminosities following the De Looze et al. (2014) relation (case of HII/starburst), scaled for a Chabrier (2003) IMF. Globally, the clustered LF presents a higher number density (up to about 1 dex) and higher luminosity objects than the IR-derived [C II] LF of Gruppioni et al. (2020). The difference in the lower luminosity bins is, however, enhanced by the fact that these bins are strongly incomplete in the continuum survey (see Béthermin et al. 2020). On the other hand, there is agreement between the field LF and the LF derived from Gruppioni et al. (2020). However, if we show the IR-derived [C II] LF that also includes the companions of the central targets for $L_{\text{[C II]}} > 10^{9.5} L_{\odot}$ (magenta hexagons; see Gruppioni et al. 2020), we find that in this luminosity range the clustered [C II] LF and the IR-derived [C II] LF are nicely consistent within the errorbars. This is due to the fact that some of the sources included in these luminosity bins are the same, clustered around the central targets, detected both in line and in continuum.

Observed luminosity functions at high and low-z

Now we can move on to comparing our results to other works in the literature, at both high and low-z (Fig. 2.11). We see that our LFs are consistent with previous estimates at $z = 4.4$ and $z \sim 5$ from Swinbank et al. (2012) and Capak et al. (2015). Swinbank et al. (2012) started from an original 870 μm selection of galaxies with LABOCA (Weiß et al. 2009) and considered the only two galaxies for which the [C II] line was detected in a subsequent ALMA follow-up. However, the low continuum detection rate of the ALPINE targets (20%; Béthermin et al. 2020) compared to the line detection rate (64%) suggests that a considerable fraction of [C II] emitting galaxies can be missed when starting from continuum pre-selected samples, hence the LF of Swinbank et al. (2012) likely provides a lower limit to the number density of the [C II] emitters. In case of the estimate from Capak et al. (2015), we use the value reported in Hemmati et al. (2017). Also, in this case, the data likely provide a lower limit to the true distribution, since the targets of Capak et al. (2015) are Lyman break galaxies, that is,

UV-selected objects and, hence, [C II]-bright but optically-faint objects are not taken into account in this LF. Moreover, in this estimate the [C II] serendipitous emitters in the ten pointings of Capak et al. (2015) are not considered (e.g., AzTEC–3, Riechers et al. 2010; CRLE, Riechers et al. 2010).

Our values are consistent with the lower limit to the [C II] LF of Cooke et al. (2018). This study also provides a lower limit because it considers [C II] emitting galaxies pre-selected based on their SCUBA2 850 μm flux density (Geach et al. 2017).

We also compared our estimates with measurements at higher redshift (Yamaguchi et al. 2017). The points in Yamaguchi et al. (2017) represent upper limits to the [C II] LF at $z \sim 6$. We can see that the field LF is consistent with the upper limits. On the other hand, the clustered LF seems to predict more [C II] emitters than Yamaguchi et al. (2017) at $L_{[C \text{ II}]} = 10^{8.75} L_\odot$ and that is probably because it is biased in favor of an overdense environment.

It is interesting to additionally compare our work with an extrapolation of the *Herschel* LF at $z \sim 5$ (Gruppioni et al. 2013; Gruppioni et al., in prep.). The extrapolation was performed using the SCUBA2 number counts (Geach et al. 2017) to constrain the evolution at high redshift (Gruppioni & Pozzi 2019). The IR luminosities were thus converted to SFRs using the Kennicutt (1998a) relation and the SFRs were transformed in [C II] luminosities following De Looze et al. (2014). We note that the same approach has been already used for deriving the CO LF in Vallini et al. (2016), which successfully reproduces the observed CO LF of ASPECS (Decarli et al. 2019b). Interestingly, we see that the global shapes of the clustered LF and the *Herschel*–derived one are in good agreement, with both LFs predicting [C II] emitters with very high luminosities ($L_{[C \text{ II}]} > 10^9 L_\odot$), with at least some of the discrepancy coming from the fact that the *Herschel* extrapolation was not intended to account for the clustering inherent in the ALPINE serendipitous sample.

Finally, we discuss how the $z \sim 5$ [C II] LF compares with the $z \sim 0$ values (Hemmati et al. 2017) to underline potential evolutionary effects. We can see that the clustered LF shows a strong evolution both in number density (up to > 1 dex) and in luminosity between $z \sim 0$ and $z \sim 5$. The field LF suggests also a possible excess of objects at $L_{[C \text{ II}]} > 10^9 L_\odot$ compared to the local value. The two LFs are however consistent within 2σ. A higher statistics for the field sample is necessary to draw robust conclusions about any evolutionary trend that is independent from clustering.

Theoretical predictions

We also compare our results with model predictions for the early Universe (Fig. 2.11). First of all, we considered the models for the [C II] LF by Popping et al. (2019). These are semi-analytical models that include radiative transfer modeling. We can see that the clustered [C II] LF predicts a higher number of objects than the models expectations at $z \sim 5$, with a disagreement that rises with increasing luminosity. A similar disagreement with models predictions is seen also for the CO LFs at high-z (Riechers et al. 2019) and for the IR LF at $z \sim 2$ (Gruppioni et al. 2015). On the other hand, the field LF appears quite consistent with the models. Further statistics would be useful to constrain the bright end of the field LF and disentangle if it remains flat at $L_{[C \text{ II}]} > 10^9 L_\odot$ (as for the clustered sample) or if it declines as shown by models.

Then we examine the predictions at $z \sim 5$ by Lagache et al. (2018). This is also a semi-analytic model combined with a photoionization code. We note that at luminosities between $10^9 L_\odot$ and $10^{10.5} L_\odot$ the Lagache et al. (2018) curve is not very
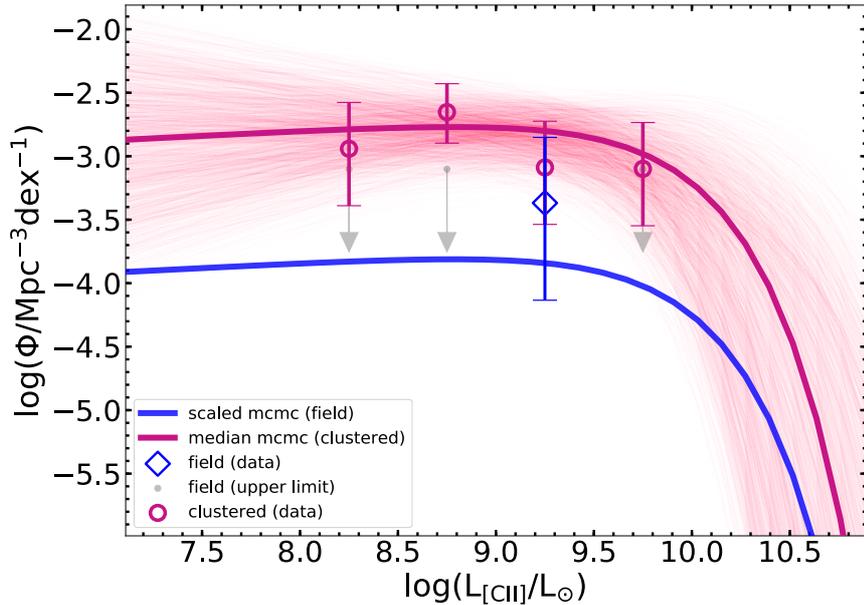
Figure 2.13: Schechter functions for the clustered (pink) and field (azure) [C II] LFs. We show also the observed LFs corresponding to independent luminosity bins (same color code) and the 2σ upper limits for the field LF (grey arrows). We fitted $\log \Phi^*$, $\log L^*$, and α for the clustered LF using a Markov Chain Monte Carlo (MCMC) method. We assumed for the field sample the same α and $\log L^*$ of the clustered LF and we scaled the normalization of the clustered LF by a factor of 11 (corresponding to the ratio between the number of clustered and field sources). The shaded area (pink; clustered sample) shows the MCMC realizations within the 16th and 84th percentile, hence, it corresponds approximately to 1σ errorbars. In case of the scaled field LF, the 1σ errors (blue area) were computed from the uncertainties of $\log \Phi^*$ of the clustered sample and the Poissonian uncertainty (at 1σ) on 11 counts.

different from the *Herschel* extrapolation. Compared to Popping et al. (2019), this model predicts more [C II] emitters at $L_{[C\ II]} > 10^{9.5}\mathrm{L}_{\odot}$, with luminosities consistent with the observed values for the clustered sample. However, we see that our observed LFs (especially the clustered one) show a higher number density of objects (> 1 dex), which is not predicted by this model.

2.5.3 Fitting with a Schechter function

We performed a fit to the [C II] LFs with the Schechter (1976) function written in logarithmic form (Fig. 2.13). Given the element of luminosity $\mathrm{d}\log L$, the number of objects $\Phi(L)\mathrm{d}\log L$ falling in the bin is:

$$\phi(L)\mathrm{d}\log L = \ln 10 \ \Phi^* \left(\frac{L}{L^*} \right)^{\alpha+1} \exp^{-\frac{L}{L^*}} \mathrm{d}\log \mathrm{L}, \qquad (2.4)$$

where α is the faint-end slope and L^* and Φ^* are the luminosity and the value of the LF at the "knee", respectively. For simplicity, we fitted the $\log \Phi(L)$ and thus also the logarithms of L^* and Φ^*. We fitted the clustered LF only because of the low statistics of the field LF and the only one independent bin. Before performing the fit, we rebinned the clustered and field LF adopting a bin spacing of 0.5 dex instead of 0.25 dex (the bin

Table 2.3: Schechter parameters for the clustered and field LFs. We report the uncertainties corresponding to the 16th and 84th percentile ($\sim 1\sigma$).

Parameter	Clustered sample	Field sample
$\log\left(L^*/\mathrm{L}_\odot\right)$	$9.88^{+0.54}_{-0.55}$	9.88 (fixed)
$\log\left(\Phi^*/\mathrm{Mpc}^{-3}\mathrm{dex}^{-1}\right)$	$-3.01^{+0.44}_{-0.61}$	$-4.05^{+0.62}_{-0.72}$
α	$-0.92^{+0.56}_{-0.44}$	- 0.92 (fixed)

width in Sect. 2.5.1). This ensures that the number counts in the bins are independent as well as the uncertainties on the fitted points.

To derive a first estimate of the fitted parameters, we performed a fit based on the maximum likelihood criterion. The best-fit values were used as initial guesses for a Markov Chain Monte Carlo (MCMC) method with the Python package *emcee* (Foreman-Mackey et al. 2013). We assumed uniform priors for α, $\log L^*$, $\log \Phi^*$. We preferred uniform priors over Gaussian ones as they represent the simplest possible choice since the probability distribution of these parameters is not known a priori. We note that the knee of the clustered LF is quite unconstrained by our data. This fact could clearly impact the derivation of the cosmic SFRD (see Sect. 2.6). In order to estimate $\log L^*$, we thus limited the upper boundary for the luminosity prior to 10.5, corresponding to an IR luminosity of $10^{13.5}\mathrm{L}_\odot$ and assuming a fiducial ratio between [C II] and IR luminosity of 10^{-3} (Díaz-Santos et al. 2013). This is a reasonable upper boundary to the IR luminosity motivated by pre-existing IR LFs at lower redshifts (Gruppioni et al. 2013; Vallini et al. 2016). The validity of the $L_{\mathrm{[C\ II]}}$–SFR relation where the latter quantity is derived from continuum estimates for our sample (see Sect. 2.4.3) suggests that this is a trustworthy assumption.

The best values for α, $\log L^*$, $\log \Phi^*$ for the clustered LF are reported in Table 2.3. These values were evaluated as the medians of the posterior probability distributions. The reported uncertainties correspond to the 16th and 84th percentile of the posteriors (equivalent to about 1σ in the case of Gaussian posteriors).

We then computed the Schechter function for the field LF as well. Since it was not possible to directly fit the data, we scaled Φ^* by a factor $1/11$ (i.e., the ratio between the number of field and clustered sources) based on the assumption that the shape of the two LFs is similar. In this way, the integration of the LF over the accessible volume and luminosity predicts a number of sources equal to the observed one (i.e., one source); see also Marshall et al. (1983). Moreover, this approach has the advantage of being independent of the binning of the LF. We obtained a value for $\log\left(\Phi^*/\mathrm{Mpc}^{-3}\mathrm{dex}^{-1}\right) = -4.05^{+0.62}_{-0.72}$ where the errors were propagated from the uncertainty on $\log \Phi^*$ of the clustered sample and the Poissonian error on the ratio 11:1.

We note that an alternative approach to derive the Schechter function for the field LF would be to directly fit the single observed data point, including in the fit also the upper limits to the field LF for the bins with no detections. The upper limits to the field LF can be determined by following the Poissonian statistics for zero counts (Figure 2.13; we reported the 2σ upper limits); see also Gehrels (1986). However, we did not use this approach due to the low statistics of the field LF, as the fit would have been more influenced from the three independent bins with the upper limits than from
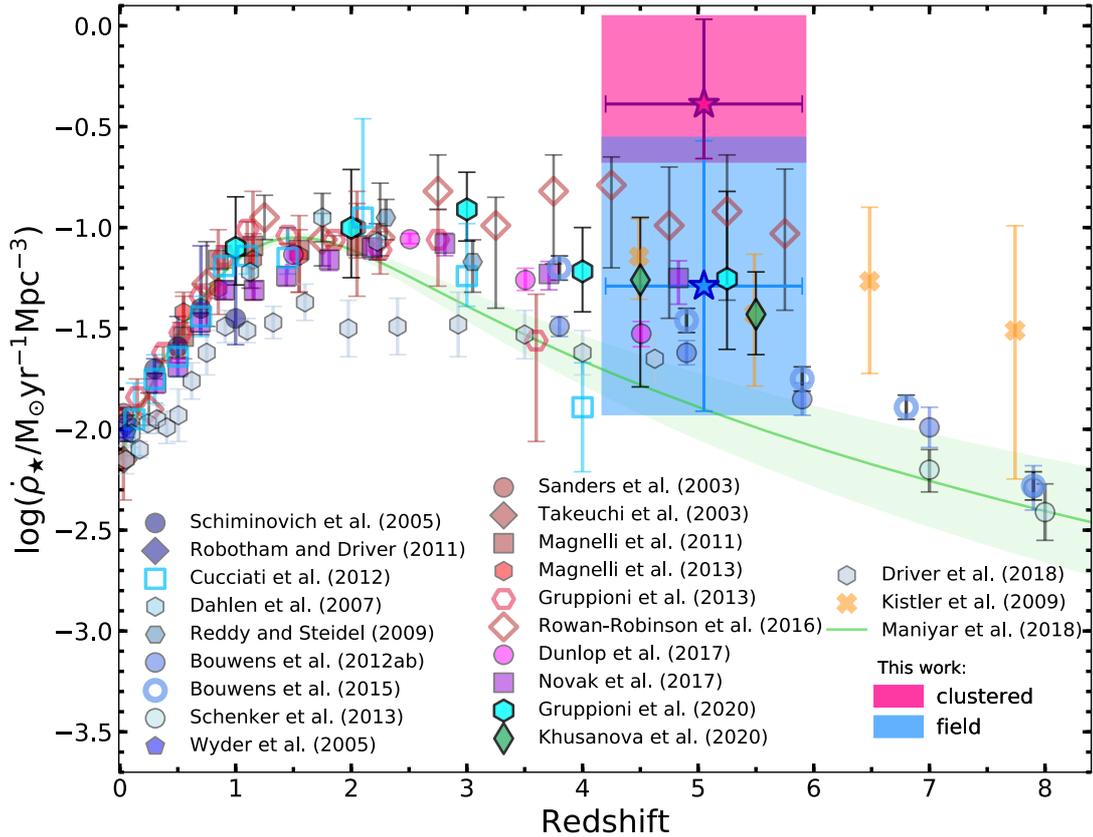
Figure 2.14: Cosmic SFRD across cosmic time. Both the estimates from the "field" and "clustered" samples are shown (azure and pink box respectively). We compare our measurements with estimates available from the literature based on multiwavelength observations. The SFRD derived from the clustered [C II] LF at $z \sim 5$ is about one order of magnitude higher than the current measurements at that redshift. On the other hand, the SFRD of the field sample spans values compatible with both UV and IR-derived estimates, with an average value a factor of ~ 1.6 higher than the estimates based on UV surveys. We consider the SFRD from the field sample as representative of the overall galaxy population since the clustered estimate is biased by overdensities around the targeted [C II].

the observed data point.

The Schechter functions of the clustered and field samples were used to estimate the cosmic SFRD (Sect. 2.6).

2.6 Cosmic star formation rate density at $z \sim 5$

We know that the [C II] line is a SFR indicator (De Looze et al. 2014). Therefore the [C II] LF providing the total [C II] luminosity budget can be used to estimate the cosmic SFRD. First, we integrated the Schechter functions for the field and clustered sample in order to obtain the [C II] luminosity density $\rho_{L_{[C\ II]}} = \int \Phi(L')L' \mathrm{d} \log \mathrm{L}'$. We considered in the integration all the luminosities higher than $10^7 \mathrm{L}_\odot$. However, integrating from lower luminosities does not alter significantly the final estimates because the faint-ends of the LFs are quite flat. In case of the clustered sample, the integration was performed for all the realizations of the MCMC. On the other hand, for the field sample, we integrated the best curve and the curves corresponding to the 1σ errorbars. Then we converted the luminosity densities to SFRDs using the relation (see Table 3 of De Looze et al. 2014; case HII/starburst)

$$\log \dot{\rho}_\star = -7.06 + 1.00 \log \rho_{L_{[C\ II]}} + \log 0.94, \tag{2.5}$$

where $\dot{\rho}_\star$ is the SFRD and the last term accounts for scaling the De Looze et al. (2014) relation from a Kroupa (2001) to a Chabrier (2003) IMF. We note that the working assumption of a non-evolving $L_{[C\ II]}$–SFR relation is not trivial (Vallini et al. 2015; Carniani et al. 2018). However, as we mention in Sect. 2.4.3, it seems to work at least for the serendipitous [C II] detected in continuum. Furthermore, the validity of this conversion is independently confirmed by the ALPINE targets which, as discussed in Béthermin et al. (2020) and Schaerer et al. (2020), lie within 1σ on the De Looze et al. (2014) relation. In this way, for the clustered sample we obtained a SFRD probability distribution based on all the MCMC realizations. We considered the median value of the distribution as the best estimate of the SFRD from the clustered sample and as done previously, we reported the uncertainties corresponding to the 16th and 84th percentile (Table 2.4). On the other hand, for the field sample, we considered the SFRD value corresponding to the integration of the best curve with the associated errorbars (see Fig. 2.13).

In Fig. 2.14, we compare our results with previous estimates from the literature[7] that are based on UV surveys (Schiminovich et al. 2005; Wyder et al. 2005; Dahlen et al. 2007; Reddy & Steidel 2009; Robotham & Driver 2011; Bouwens et al. 2012a,b; Cucciati et al. 2012; Schenker et al. 2013; Bouwens et al. 2015) as well as IR, mm, and radio selections of galaxies (Sanders et al. 2003; Takeuchi et al. 2003; Magnelli et al. 2011, 2013; Gruppioni et al. 2013; Rowan-Robinson et al. 2016; Dunlop et al. 2017; Novak et al. 2017). We also show the measurements derived from optical/NIR observations (Driver et al. 2018) and gamma-ray bursts (Kistler et al. 2009). We also plot the models predictions of Maniyar et al. (2018) based on the cosmic microwave background. Finally, we compare our results with other independent measurements of the SFRD based on the ALPINE data. In particular, we show the results derived from the serendipitous sources detected in continuum (Gruppioni et al. 2020) and the SFRD

---

[7]For works prior to 2014, we show the values reported in Table 1 of Madau & Dickinson (2014), except for Kistler et al. (2009), which is not included in the table.

Table 2.4: Cosmic SFRD from the clustered and field [C II] LFs.

	Clustered	Field
$\log\left(\frac{\dot{\rho}_{\star}}{\mathrm{M}_{\odot}\mathrm{yr}^{-1}\mathrm{Mpc}^{-3}}\right)$	$-0.39^{+0.42}_{-0.27}$	$-1.29^{+0.72}_{-0.62}$

inferred from the ALPINE central targets (Khusanova et al. 2020).

We can see that the SFRD derived from the clustered sample is almost $10\times$ higher than the field value and the current estimates of the SFRD at $z \sim 5$ from the literature. The high SFRD value predicted by the clustered sample could be indicative of the reversal of the SFR-density relation at high-z. This could be driven by the higher stellar mass content of clustered galaxies and by mechanisms due to the environment (Lemaux et al. 2020). However, we recall that only a fraction of the sources in the clustered sample are part of well-known overdensities (see Fig. 2.8 and Sect. 2.4.2), while the others are associated to galaxy pairs and mergers. A further investigation of the environment around these sources will be an important goal for future observations and facilities (e.g., JWST). We consider the SFRD computed using the field sample as the most likely estimate of the cosmic star formation activity at $z \sim 5$. The measurement based on the clustered LF could indeed be biased by companions around the targeted [C II], which might not have been observed if we had started from a purely "blind" survey. Therefore, the clustered estimate may not be representative of the overall population of galaxies.

We do know that a relevant question deals with the relative contribution of the unobscured versus obscured star formation across cosmic time (see Chapter 1). The former is well-sampled by UV surveys from $z \sim 0$ up to $z \sim 10$ (Bouwens et al. 2015; Oesch et al. 2018). On the other hand, the latter is captured by surveys at longer wavelengths, typically IR and sub-mm. As we discussed in the Introduction, the obscured star formation is well constrained by statistically robust samples up to $z \sim 3$, whereas at higher redshift, its contribution to the total budget of star formation is quite uncertain. If we look at the average value of the SFRD based on the field LF, we can see that it is a factor of ~ 1.6 higher than the measurement based on UV surveys (Bouwens et al. 2015). This means that there might be a fraction of (obscured) star formation that is not captured by UV surveys. However, when looking at the errors, we see that our estimate varies between values that are completely consistent with the UV estimates (i.e., neglible obscured star formation) to values that are about ten times higher than the UV measurements. A scenario consisting of a significant fraction of dust-obscured star formation already in place at $z > 4$ is suggested by IR, mm, and radio selections of galaxies (Bouwens et al. 2015; Novak et al. 2017; Gruppioni et al. 2020). Because of the large uncertainties, our measurement does not allow us to assess the importance of obscured versus unobscured star formation at $z \sim 5$. Further observations of larger volumes of the sky are thus necessary to better constrain the [C II]-derived SFRD.

Chapter 3

The multiwavelength kinematics of GMASS 0953[1]

3.1 Massive galaxies at $z \sim 2$

Over the last twenty years our knowledge of massive galaxies (stellar mass $M_\star \gtrsim 10^{11}$ $M_\odot$) has made a leap forward thanks to large observing campaigns targeting these objects (e.g., Mignoli et al. 2005; Kurk et al. 2013; Förster Schreiber et al. 2009; Wisnioski et al. 2019). Investigating these systems is pivotal to shed light on the mechanisms that regulate the mass assembly inside galaxies, expecially at the peak epoch of both star formation and nuclear activity (i.e., $z \sim 2$; Madau & Dickinson 2014).

The advent of integral field spectroscopy brought a revolution in the study of $z \sim 2$ massive galaxies. Spatially resolved observations at the NIR wavelengths unveiled that rotating discs are common in these objects (Förster Schreiber et al. 2006, 2009; Wisnioski et al. 2015), with important implications for their growth mode. The interplay between AGN and their hosts has been deeply investigated through spatially resolved observations of ionized outflows traced by strong emission lines (e.g. Harrison et al. 2012; Genzel et al. 2014; Carniani et al. 2015b) while at the sub-millimeter wavelengths interferometers as NOEMA and ALMA have provided key information on the molecular gas content of massive systems through CO lines and dust emission (e.g. Scoville et al. 2016; Tacconi et al. 2018).

Nevertheless, a number of questions remain open. A first issue concerns the quenching of star formation in massive spheroids. As we discussed in Chapter 1, AGN feedback is actually suggested by models to be the main actor of this process. However, more observational constraints are needed as the details of this mechanism are poorly understood.

Another key issue concerning $z \sim 2$ massive galaxies relates to the kinematics of the ISM. Using rotation curves to investigate the kinematics of $z \sim 2$ discs provides important constraints on the dark matter content and on the evolution of scaling relations such as the Tully-Fisher (Tully & Fisher 1977) whose matching is an important test bench for theoretical models (e.g. Ferrero et al. 2017). Most of the studies at $z \sim 2$ uses the ionized phase of the ISM to trace the kinematics of massive galaxies, which has been deeply investigated from large programs such as SINS (Förster Schreiber et al. 2009) and KMOS3D (Wisnioski et al. 2015). The ionized gas has though the drawback to be more affected compared to the cold gas by non-circular motions (e.g., outflows), which may make this tracer, if considered alone, not representative of the overall kinematics (e.g., Lelli et al. 2018). A multiwavelength approach that employs different ISM tracers (e.g., molecular, ionized), is hence required in order to build a robust picture of

---

[1]Based on Loiacono F. et al., 2019, MNRAS, 489, 681.

45
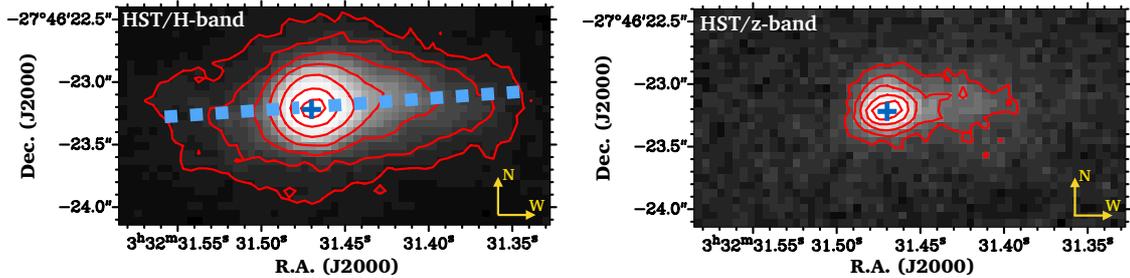
Figure 3.1: H-band (1.6 μm, left panel) and z-band (0.85 μm, right panel) images of GMASS 0953 (HST/WFC3 and ACS). The lowest contour is at 5σ. The blue crosses show the emission peak, which we take as the photometric and dynamical center of the galaxy. The central region appears extremely bright and compact with an effective radius $R_e \sim 2.5$ kpc, estimated from the H-band image (van der Wel et al. 2014). The dashed line indicates the major axis (position angle $\phi = 94°$).

the kinematics of $z \sim 2$ objects. At the moment this kind of studies is rare, regarding just a scanty number of high-z galaxies (see for example Genzel et al. 2013; Chen et al. 2017; Herrera-Camus et al. 2019; Lelli et al. 2018; Übler et al. 2018) because of the lack of multiwavelength spectroscopic data at high redshift.

In this Chapter, we report a multiwavelength study of the $z \simeq 2.226$ galaxy GMASS 0953. This is a massive, compact star-forming galaxy, which hosts an obscured AGN. This source has been already studied by Talia et al. (2018), who investigated its molecular gas content revealing the existence of a rotating disc traced by the CO(J=6-5) line. Moreover, Popping et al. (2017) found a very short depletion timescale for the molecular gas, which implies that the galaxy is rapidly consuming its gas reservoir and it will likely evolve into a passive system. The present analysis integrates the aforementioned picture adding information on the ionized gas kinematics. In particular, we discuss how the ionized gas motions relate to the molecular phase and what is the effect of the AGN feedback on the galaxy. In our analysis, we used NIR observations of [O III] $\lambda5007$ and Hα combining a slit spectrum, obtained with the Gemini Near InfraRed Spectrograph (GNIRS), with integral field data collected by the Spectrograph for INtegral Field Observations in the Near Infrared (SINFONI) and the K-band Multi-Object Spectrograph (KMOS). The use of different instruments that work at similar wavelengths has the advantage to corroborate the results arising from independent measurements and provides also complementary details.

This Chapter is organized as follows. In Sect. 3.2 we describe the main properties of GMASS 0953 while Sect. 3.3 concerns the data analysis. The multiwavelength kinematics is discussed in Sect. 3.4 and Sect. 3.5. Finally, we study the AGN feedback in Sect. 3.6.

We adopt a ΛCDM cosmology with $\Omega_\Lambda = 0.71$, $\Omega_{\mathrm{M}} = 0.29$ and $H_0 = 69.6$ km s^{-1}Mpc^{-1}. In this cosmology $1''$ corresponds to 8.4 kpc at $z \simeq 2.226$. We assume a Chabrier (2003) IMF.

3.2 GMASS 0953: a global portrait

GMASS 0953 (also known as K20-ID5, GS3-19791, 3D-HST GS30274, e.g. Daddi et al. 2004; Popping et al. 2017; Wisnioski et al. 2018) is a massive star-forming galaxy at $z \simeq 2.226$ located in the Chandra Deep Field South (CDFS; Giacconi et al. 2002) (see Table 3.1 for the main properties of the galaxy). It presents an irregular morphology (Fig. 3.1), visible in both the HST/WFC3 (H-band, 1.5 μm) and HST/ACS (z-band, 0.85 μm) images, which appears bright and compact in the central region ($R_{\mathrm{eff,H-band}} \sim 2.5$ kpc, corresponding to 0.3″; van der Wel et al. 2014), showing also an off-nuclear emission to the west, interpreted as an asymmetric stellar disc or a merger remnant (Wisnioski et al. 2018; van Dokkum et al. 2015).

The galaxy was selected among the AGN-hosts of Cimatti et al. (2013), which represent a subsample of the GMASS survey (Kurk et al. 2013), including active galaxies with a stellar mass $M_\star > 10^{10}$ M$_\odot$ and a X-ray luminosity $L_X > 10^{42.3}$ erg s^{-1}. The AGN activity of GMASS 0953 was inferred from the X-ray luminosity $L_X \sim 5 \times 10^{44}$ erg s^{-1} corrected for obscuration (Dalla Mura et al., in prep.) and the hardness ratio[2] HR = 0.6 (Luo et al. 2017), both higher than those measured in purely star-forming systems (Norman et al. 2004). The optical emission line ratios are also consistent with an AGN (Newman et al. 2014) even if shock ionization by a strong galactic wind is also possible (van Dokkum et al. 2005). Indications of outflowing material, likely boosted by the AGN, were observed in the rest-frame optical spectrum (Förster Schreiber et al. 2014; Genzel et al. 2014), in the UV absorption lines (Cimatti et al. 2013) and we found further evidence in this thesis. On the other hand, the AGN activity does not emerge from the UV emission lines. This was verified by the measurement of the line ratios of C IV $\lambda 1550$, He II $\lambda 1640$ and C III] $\lambda 1909$ using MUSE data (P. Rosati, private communication). These ratios place GMASS 0953 closer to the observed star-forming galaxies than to the AGN in the diagnostic diagram of Feltre et al. (2016), likely because of the high obscuration ($N_H = 4.4^{+4.7}_{-1.7} \times 10^{24}$ cm^{-2}, Dalla Mura et al., in prep.).

Thanks to the available photometric spectral energy distribution (SED[3]) from the UV to sub-mm wavelengths, we estimated several properties of the galaxy. The stellar mass $M_\star = (1.15 \pm 0.10) \times 10^{11}$ M$_\odot$ was evaluated from the SED decomposition applying a modified MAGPHYS code (da Cunha et al. 2008) that includes the AGN component, relevant in the mid-infrared (Berta et al. 2013), as done by Delvecchio et al. (2014). The derived infrared luminosity L_{IR} in the rest-frame 8 - 1000 μm, corrected for the AGN contribution, was used to estimate the star formation rate SFR$_{\mathrm{IR}}$ = 214 ± 20 M$_\odot$yr^{-1} through the Kennicutt (1998b) relation, rescaled to a Chabrier (2003) IMF. The stellar mass and the SFR place GMASS 0953 on the main sequence at $z \sim 2$ (e.g. Daddi et al. 2007).

The kinematical properties of GMASS 0953 were investigated by Förster Schreiber et al. (2009), who inferred an upper limit for the dynamical mass $M_{\mathrm{dyn}} < 5.8 \times 10^{11}$ M$_\odot$. Wisnioski et al. (2018) modelled the Hα kinematics revealing a disky structure extending up to 13 kpc with an average rotation velocity of 200 km s^{-1}. Evidence of rotation on a smaller scale was found by Talia et al. (2018) studying the CO (J=6-5) transition produced by a rapidly rotating ($V_{\mathrm{CO}} = 320^{+92}_{-53}$ km s^{-1}) and very compact

---

[2]The hardness ratio is defined as HR = (H - S)/(H + S) where H and S are the photon counts in the hard (2-10 keV) and soft (0.5-2 keV) X-ray band respectively.

[3]The photometric SED of GMASS 0953 was obtained collecting data from MUSIC (Grazian et al. 2006), SPITZER/MIPS (Magnelli et al. 2011), Herschel/PACS (Magnelli et al. 2013) and SPIRE (Roseboom et al. 2010), ALMA (Popping et al. 2017; Talia et al. 2018; Ueda et al. 2018).

Table 3.1: Main properties of GMASS 0953. Column description: (1), (2) sky-coordinates of GMASS 0953 in the *HST*/WFC3 *H*-band image. (3) Redshift derived from the [O III] $\lambda5007$ narrow line. (4) Effective radius measured on the *HST*/WFC3 *H*-band image (van der Wel et al. 2014). (5) Stellar mass derived from SED fitting. (6), (7) Star formation rate derived from the infrared luminosity and from Hα. (8) X-ray intrinsic luminosity (Dalla Mura et al., in prep.). (9) Hardness ratio (Luo et al. 2017). (10) Column density (Dalla Mura et al., in prep.). (11) Color excess derived from the Hα and Hβ line ratio. (12) Electron number density evaluated from the [S II] $\lambda\lambda6716$, 6731 line ratio.

R.A.	Dec.	z	$R_{\rm eff,H-band}$	$M_\star$	SFR$_{\rm IR}$	SFR$_{\rm H\alpha}$	L_X(2-10 keV)	HR	$N_{\rm H}$	E(B-V)	$n_{\rm e}$
(J2000)	(J2000)		(kpc)	($10^{11}{\rm M_\odot}$)	(M$_\odot$ yr^{-1})	(M$_\odot$ yr^{-1})	(erg s^{-1})		($10^{24}{\rm cm^{-2}}$)		(cm^{-3})
(1)	(2)	(3)	(4)	(5)	(6)	(7)	(8)	(9)	(10)	(11)	(12)
3:32:31.4	-27:46:23.2	2.226	2.5	1.15 ± 0.10	214 ± 20	498 ± 33	5×10^{44}	0.6	$4.4^{+4.7}_{-1.7}$	0.8 ± 0.3	~ 500

core ($R_{\rm CO} = 0.75 \pm 0.25$ kpc). Talia et al. (2018) found also a short depletion timescale for the molecular gas ($\tau_{\rm dep} < 150$ Myr) and a low molecular gas fraction ($f_g < 0.2$) in agreement with Popping et al. (2017), which imply that GMASS 0953 might quickly cease its star formation activity, likely turning into a passive galaxy.

3.3 Data analysis

In the sections below we describe the spectroscopic dataset and the line fitting methods that we used to evaluate the physical properties of GMASS 0953. We also discuss the derivation of total flux maps from the integral field data, which show the spatially resolved emission line morphology. We focus in particular on the [O III] $\lambda5007$ and Hα lines that are then used to model the kinematics (see Sect. 3.4)

3.3.1 GNIRS one-dimensional spectrum

We used the data of Kriek et al. (2008) (see van Dokkum et al. 2005 for the details) obtained with the GNIRS spectrograph (Elias et al. 2006) at the Gemini South Observatory. They consist of a one-dimensional and two-dimensional spectra, publicly available, that cover the range 1.0 - 2.5 μm with a resolving power $R \sim 1800$.

Several emission lines are present such as [O II] $\lambda\lambda3727$, 3729, [OIII] $\lambda\lambda4959$, 5007, Hα, Hβ, [N II] $\lambda\lambda6548$, 6584 and the [S II] $\lambda\lambda6716$, 6731 doublet (Fig. 3.2, top panel).

We analyzed the one-dimensional spectrum through line fitting. The analysis was carried out with SPECFIT (Kriss 1994), a spectral fitting tool that runs in the Image Reduction and Analysis Facility (IRAF) environment. The galaxy emission was modelled with a linear continuum and eight Gaussian components, one for each line. We divided the spectrum into two ranges including Hβ, [O III] $\lambda\lambda4959$, 5007 (1.5 - 1.7μm) and Hα, [N II] $\lambda\lambda6548$, 6584, [S II] $\lambda\lambda6716$, 6731 (2.0 - 2.3 μm) on which we performed two fits separately. The ratio between the line centroids of oxygen, nitrogen and sulfur doublets was fixed to the theoretical one (0.990, 0.995 and 0.998 respectively). We initially used two Gaussian functions to reproduce [O III] $\lambda\lambda4959$, 5007. However, both the lines show a broad, blueshifted wing, detected at 3σ and 5σ of significance for [O III] $\lambda4959$ and [O III] $\lambda5007$, that is not reproduced by one Gaussian. In order to account for these emissions, we performed a second fit adding two other Gaussians (Fig. 3.2, middle panel). This addition improved significantly the reduced
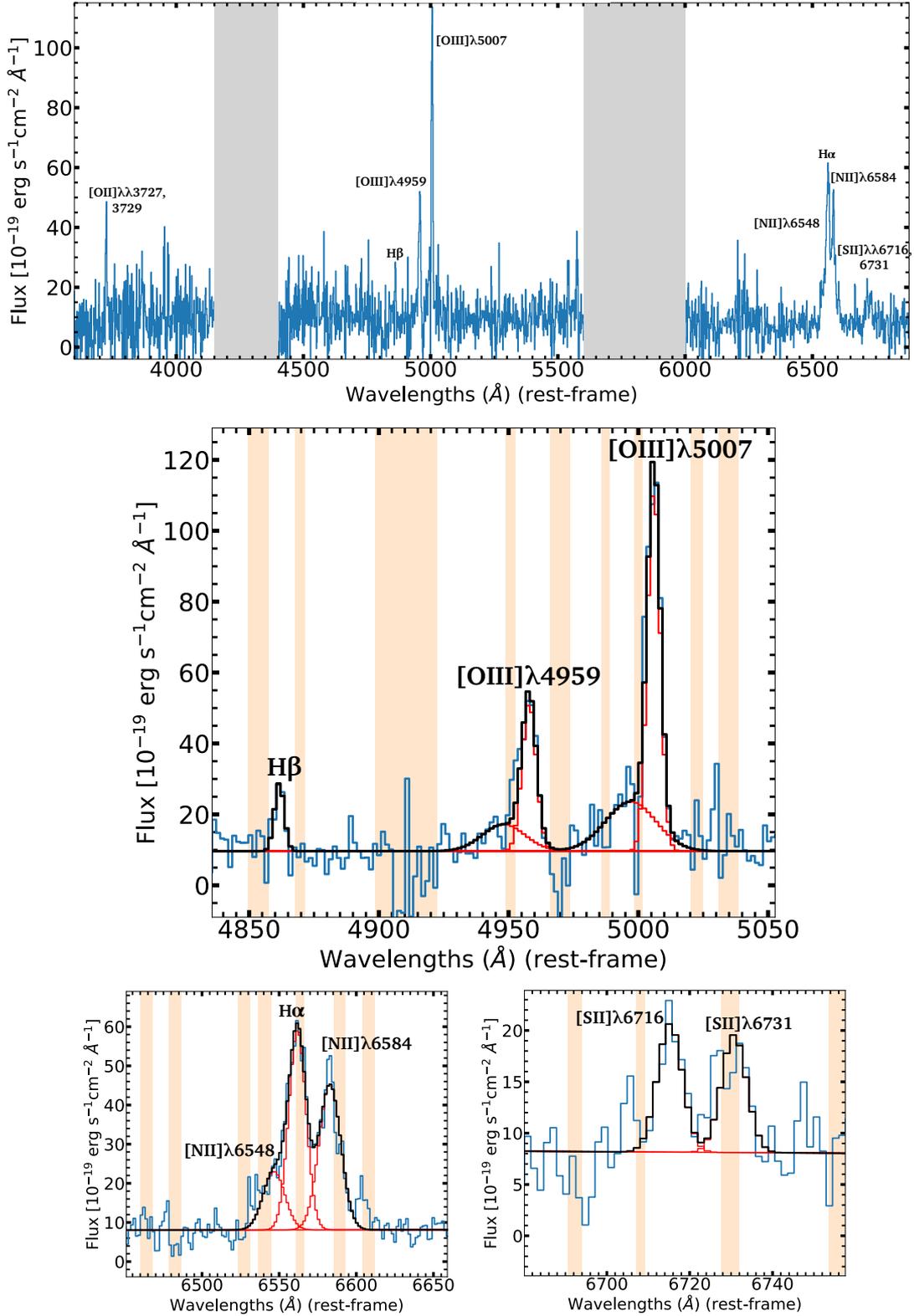
Figure 3.2: Top panel: GNIRS one-dimensional spectrum. Middle panel: line fits of Hβ and [O III] $\lambda\lambda$4959, 5007. Bottom panels: line fits of [NII] $\lambda\lambda$6548,6584 and Hα (left) and [S II] $\lambda\lambda$6716,6731 (right, fit (b) of Table 3.2). The black line represents the model superimposed on the data (blue line), with the single components in red. The vertical bands show the location of the atmospheric lines. The profile of [O III] $\lambda\lambda$4959, 5007 shows a blueshifted wing that was modelled with a broad Gaussian function (FWHM ~ 1270 km s^{-1}).

Table 3.2: Emission line properties derived from the line fitting of the GNIRS spectrum. Letter (a) refers to the line fit of the [S II] $\lambda\lambda6716, 6731$ doublet in which only the centroids ratio was fixed to the theoretical value while letter (b) indicates the fit in which the FWHM of [S II] $\lambda6731$ was matched to the FWHM of [S II] $\lambda6716$ calculated in fit (a) (see Sect. 3.3.1).

Line	Flux	Line centroid	FWHM
	$(10^{-19}$ erg s^{-1} cm$^{-2})$	(rest-frame, Å)	(km s^{-1})
Hβ	278 ± 58	4862.4 ± 0.4	264 ± 63
[OIII]$\lambda4959$ (narrow)	936 ± 125	4958.7 ± 0.2	394 ± 40
[OIII] $\lambda4959$ (broad)	501 ± 157	4949 ± 2	1170 ± 389
[OIII] $\lambda5007$ (narrow)	2084 ± 249	5006.8 ± 0.2	354 ± 31
[OIII] $\lambda5007$ (broad)	1099 ± 262	4998 ± 2	1376 ± 356
[NII] $\lambda6548$	847 ± 107	6547.4 ± 0.5	756 ± 78
Hα	2312 ± 108	6562.6 ± 0.3	604 ± 30
[NII] $\lambda6584$	2120 ± 149	6583.7 ± 0.5	756 ± 78
[SII] $\lambda6716$ (a)	307 ± 58	6715.9 ± 0.6	319 ± 79
[SII] $\lambda6731$	327 ± 73	6731.4 ± 0.6	413 ± 92
[SII] $\lambda6716$ (b)	307 ± 58	6716.0 ± 0.5	319 ± 79
[SII] $\lambda6731$	282 ± 59	6731.5 ± 0.5	319 ± 79

chi-square χ^2_{dof} from 1.23 to 1.01. The new fitted components have a FWHM ~ 1270 km s^{-1}, much broader in comparison to those already fitted (FWHM ~ 370 km s^{-1}). The blueshifted component of [O III] $\lambda5007$ is also clearly visible in the GNIRS two-dimensional spectrum (broad component in Fig. 3.7, left panel).

In the case of Hα and [N II] $\lambda\lambda6548, 6584$ we note that the fitted line widths result considerably larger than the FWHM of other elements (Table 3.2). This could be due either to the overlapping of several sky lines, which may alter the line profiles, or to the presence of blueshifted components, hidden by the line blending, that were not modelled separately (Fig. 3.2, bottom left panel). The latter interpretation could be supported by the blueshifted emission affecting the Hα profile after the subtraction of the [N II] $\lambda\lambda6548, 6584$ models from the KMOS spectrum (see Sect. 3.3.3 and Fig. 3.7, right panel).

In the [S II] $\lambda\lambda6716, 6731$ case, two fits have been performed. If only the centroids ratio is fixed, the FWHM of [S II] $\lambda6731$ results indeed higher than the one relative to [S II] $\lambda6716$ (Table 3.2, fit (a)). However, the [S II] $\lambda6731$ emission is affected by a sky line (Fig. 3.2, bottom right panel) that likely alters its profile. In order to account for this uncertainty, we performed a second fit in which the line widths were matched to the FWHM of [S II] $\lambda6716$ (i.e. the more reliable one) calculated in the first fit.

All the parameters derived from line fitting are reported in Table 3.2. The fitted values are consistent with the ones found by van Dokkum et al. (2005) despite of the addition of the broad [O III] $\lambda\lambda4959, 5007$ components.

We used the fitted quantities to evaluate some global properties of GMASS 0953 like dust obscuration, the SFR and the electron number density. Assuming a Calzetti et al. (2000) extinction curve, we estimated the color excess $E(B - V) = 0.8 \pm 0.3$ from the line ratio of Hα and Hβ. This value indicates that GMASS 0953 is a highly obscured system (see also van Dokkum et al. 2005). Before calculating the color excess, the

fluxes of Hα and Hβ were corrected for the stellar continuum absorption considering an equivalent width EW = 4 ± 1 Å (van Dokkum et al. 2005). Then we derived the SFR$_{\mathrm{H}\alpha}$ = 498 ± 33 M$_\odot$yr^{-1} using the de-reddened Hα through the Kennicutt (1998b) relation, rescaled to a Chabrier (2003) IMF. This value is higher than the one obtained using the infrared luminosity, likely because of the AGN contamination (see also Sect. 3.3.3).

Finally, we measured the electron number density n_{e} from the [S II] $\lambda\lambda6716, 6731$ line ratio calculated in the two fits. Both ratios are compatible with an electron number density of 500 cm^{-3} (Osterbrock & Ferland 2006), which can vary in the range $100 < n_{\mathrm{e}}$ [cm^{-3}] $< 2 \times 10^3$ because of the uncertainties in the line ratios. Values of $n_{\mathrm{e}} \sim 500$ cm^{-3} are typical of AGN narrow line regions. However, it is highly reasonable that the galaxy ISM also contributes to it because of the large size of the ionized gas, that extends over the entire galaxy as visible from the SINFONI and KMOS maps (Fig. 3.3 and Fig. 3.12).

3.3.2 SINFONI integral field spectrum

We analyzed the data of GMASS 0953 from the SINS survey (see Förster Schreiber et al. 2009 for the observation details and data reduction) carried out with the SIN-FONI (Eisenhauer et al. 2003) integral field spectrograph (IFS) at the ESO Very Large Telescope (VLT). They consist in a data-cube covering the H-band (1.5 - 1.7 μm) with a resolving power $R \sim 2900$ and a channel width of 1.95 Å containing the sky-subtracted data. The visible lines are Hβ and the [O III] $\lambda\lambda4959, 5007$ doublet. The observation is seeing limited with a PSF of 0.7$''$. We verified the SINFONI astrometry in order to properly overlap the emission line maps on the HST images of GMASS 0953 as explained in Sect. 3.3.4.

The SINFONI data-cube (and also the KMOS one) was handled using the software GIPSY (van der Hulst et al. 1992). We focused in particular on the [O III] $\lambda5007$ narrow line fitted in the GNIRS spectrum, which we used for the kinematic modelling due to its high brightness, and on the [O III] $\lambda5007$ blueshifted component. The total flux map, which shows the [O III] $\lambda5007$ narrow line morphology, was derived co-adding $N = 17$ channels after masking out all the pixels with a signal-to-noise ratio $F/\sigma < 1$ and removing by hand (channel by channel) the instrumental noise peaks present in the field of view. We considered as the typical noise in one channel the average standard deviation $\sigma = 1.7 \times 10^{-20}$ erg s^{-1}cm^{-2}Å^{-1} of the signal in the channels without emission from the galaxy. The noise of the [O III] $\lambda5007$ map was estimated by the relation $\sigma_{\mathrm{TOT}} = \sigma\sqrt{\bar{N}}$, where $\bar{N} = 9$ is the average number of co-added channels at each pixel position in the map. Due to the masking process, the number of co-added channels is not constant for all the pixels.

From the map[4] (Fig. 3.3, top left panel), the [O III] $\lambda5007$ narrow line emission appears quite extended (see Fig. 3.12 for a visual comparison with the $HST/WFC3$ image). Moreover, the flux distribution is very asymmetric, with the western side much brighter than the eastern one. The asymmetry in the flux distrubution is visible also in the GNIRS two-dimensional spectrum (narrow component in Fig. 3.7, left panel).

Then, after a by eye inspection of the whole data-cube, we stacked the channels without emission lines or sky subtraction residuals to obtain the continuum radiated by

---

[4]We point out that the [O III] $\lambda5007$ map was not continuum subtracted because the contributed continuum flux on $N = 17$ channels is very low (less of 2σ significance).
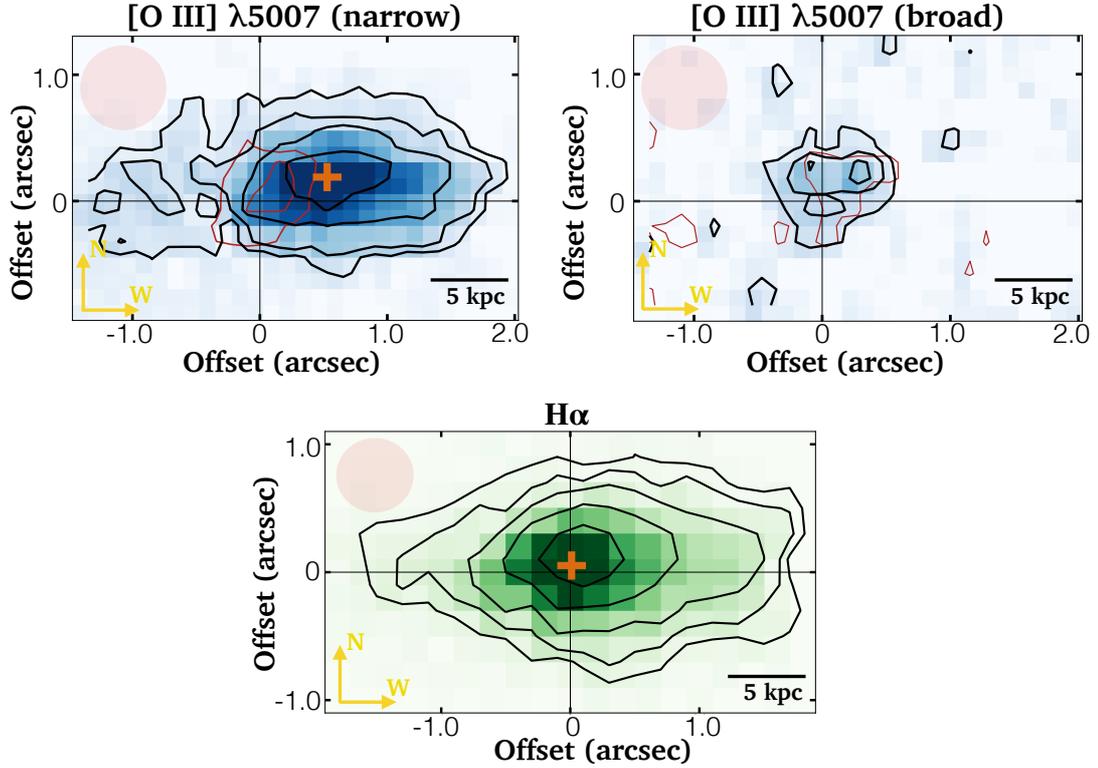
Figure 3.3: Emission line maps extracted from the SINFONI and KMOS data-cubes. Top panels: narrow and broad component of [O III] λ5007 (black contours and colors). Flux contour levels are at 3, 6, 12, 24σ for the [O III] λ5007 narrow line and at 2, 4, 6σ for the [O III] λ5007 broad component. The red contour shows the continuum emission stacked on the entire spectrum (left panel) and on $N = 18$ channels (right panel), i.e. the same number of co-added channels for the [O III] λ5007 blueshifted component. Compared to the center of GMASS 0953 (0″ offset in the map) the [O III] λ5007 narrow line morphology appears asymmetric, concentered in the western region of the galaxy, as indicated also by the off-centered emission peak (orange cross); on the other hand the [O III] λ5007 blueshifted line emits close to the nuclear region. Bottom panel: Hα emission. Flux contour levels are at 3, 6, 12, 24, 48σ. Compared to the [O III] λ5007 emission Hα shows a more symmetric morphology, with the emission peak (orange cross) close to the center. All the maps are centered on the peak of the *HST/H*-band image. The beam size of SINFONI and KMOS is shown in pink.
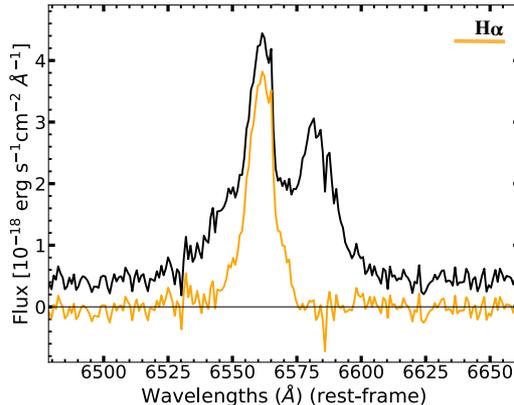
Figure 3.4: Hα and [N II] λλ6548, 6584 emission lines (KMOS data). We show the Hα emission (orange) after the subtraction of [N II] λλ6548, 6584 and stellar continuum (black).

the galaxy. The continuum emission is produced by the inner region of GMASS 0953 (Fig. 3.3, top left panel) and it originates from the stellar component; however, also a contribution from the obscured AGN is possible. This is indeed less affected by dust extinction at rest-frame optical wavelengths than in the UV, where the nuclear activity of GMASS 0953 does not emerge (see Sect. 3.2). In order to properly overlap the SINFONI line maps to the *HST* images of the galaxy (see Sect. 3.3.4), we evaluated the coordinates of the continuum peak fitting the stacked emission with a two-dimensional elliptical Gaussian. We observe that there is a shift of $0.58'' \pm 0.24''$ (equivalent to 4.9 ± 2.0 kpc) between the fitted coordinates and the [O III] λ5007 narrow line peak (cross in Fig. 3.3, top left panel), evaluated also through a two-dimensional Gaussian fit. It is not clear why the [O III] λ5007 emission peaks off-center in GMASS 0953. We may speculate that the emission peak could be due to a star formation clump in the western side of the galaxy, a shock in the ISM or it could be a consequence of a past merger (Wisnioski et al. 2018; van Dokkum et al. 2015). Observations with better spatial resolution are necessary to constrain the emission mechanism.

The detection of blueshifted emission with respect to the [O III] λ5007 narrow line, corresponding to the broad component fitted in the GNIRS spectrum (Fig. 3.2, middle panel), was confirmed by the SINFONI data, which also provided its spatial position. Adding $N = 18$ channels from 4974 Å to 4995 Å (rest-frame wavelengths), we obtained a 6σ detection localized near the galaxy center (Fig. 3.3, top right panel). In order to assess if this emission was truly due to [O III] λ5007 and not to the stellar continuum, which also peaks near the galaxy center, we compared it to the continuum flux of $N = 18$ co-added channels, i.e. the same number of stacked channels for the [O III] λ5007 broad component. These channels were selected at wavelengths close to the oxygen line. As evident from the comparison of the contours, the blueshifted component is significantly brighter than the continuum, hence it traces a genuine emission from the [O III] λ5007 line[5]. This component is clearly visible also by looking at the position-velocity (pv) diagram extracted one pixel above the major axis of the galaxy (Fig. 3.7, middle panel). It appears like an evident off-set emission from the [O III] λ5007 narrow line reaching a velocity difference from the bulk of the galaxy emission

---

[5]In the [O III] λ4959 case an emission near the galaxy center was also detected but it was only slightly brighter than the continuum level so we do not report it.

of ~ -1200 km s^{-1}.

3.3.3   KMOS integral field spectrum

To model the Hα kinematics, we employed integral field data from the KMOS^{3D} survey (Wisnioski et al. 2015), which investigates the kinematics of galaxies at $0.7 < z < 2.7$ using the NIR spectrograph KMOS (Sharples et al. 2013) at the VLT. GMASS 0953 is one of the compact, massive galaxies in the sample of Wisnioski et al. (2018). It was observed with a resolving power $R \sim 3965$ at Hα wavelengths and a spatial resolution of 0.59″. The spectrum covers the range 1.95 - 2.3 μm with a channel width of 2.8 Å and an average noise of 1.6×10^{-20} erg s^{-1}cm^{-2}Å^{-1} in each channel. The visible lines are Hα, [N II] $\lambda\lambda6548$, 6584 and the [S II] $\lambda\lambda6716$, 6731 doublet. For the observation details and the data reduction see Wisnioski et al. (2015).

In order to study the kinematics of Hα, we carried out a line fit to subtract the stellar continuum and the nitrogen emission that is partially mixed with the Hα line (black line in Fig. 3.4), as already seen in the GNIRS spectrum (Fig. 3.2, bottom left panel). The line fit was performed in each pixel of the KMOS data-cube containing the stellar and [N II] $\lambda\lambda6548$, 6584 emission (Fig. 3.5). We selected a region of 5×5 pixels corresponding to the galaxy central part because the nitrogen and the stellar emission were mainly confined in a region of this size (~ 6.7 kpc). For each pixel we extracted a spectrum that was modelled with three Gaussians and a linear continuum. The centroids ratio of the [N II] $\lambda\lambda6548$, 6584 doublet and Hα was fixed to the theoretical one (0.995 for the [N II] $\lambda\lambda6548$, 6584 lines and 0.998 for the [N II]$\lambda6548$ and Hα ratio); we also imposed the same FWHM for the nitrogen lines and fixed their intensity ratio to 1:3[6]. We then subtracted from each pixel in the data-cube the corresponding [N II] $\lambda\lambda6548$, 6584 models and the continuum level. In this way we obtained a data-cube that contains only the Hα emission, which was used to study the kinematics (orange line in Fig. 3.4). We then stacked the channels with the line ($N = 25$) to obtain the total flux map (Fig. 3.3, bottom panel). In comparison to the [O III] $\lambda5007$ emission, the Hα morphology appears much less asymmetric, with the line peak closer to the galaxy center. The central position of the peak may support the substantial contribution to the line from the AGN, which explains the discrepancy between the Hα derived SFR and the one inferred from the IR luminosity (see Sect. 3.3.1).

3.3.4   Astrometry

We verified the astrometry of the SINFONI data against the *HST* imaging of GMASS 0953. During the analysis we observed indeed that a spatial offset is present between the SINFONI field of view and the HST images of GMASS 0953 (Fig. 3.6, left panel). In order to properly overlap the maps of [O III] $\lambda5007$ on the *HST* images, we adjusted the data-cube coordinates imposing the matching between the peak of the SINFONI stacked continuum and the light peak determined in the *HST/H*-band image. The coordinates of the peaks were both calculated through a two-dimensional Gaussian fit. The correction resulted in a shift of + 1.26″ in R.A. and + 2.16″ in Dec. applied to the data-cube coordinates, after which we could nicely superimpose the SINFONI line

---

[6]We executed also a fit in which the intensity ratio of [N II] $\lambda\lambda6548$, 6584 was left free, but it showed no significant differences.
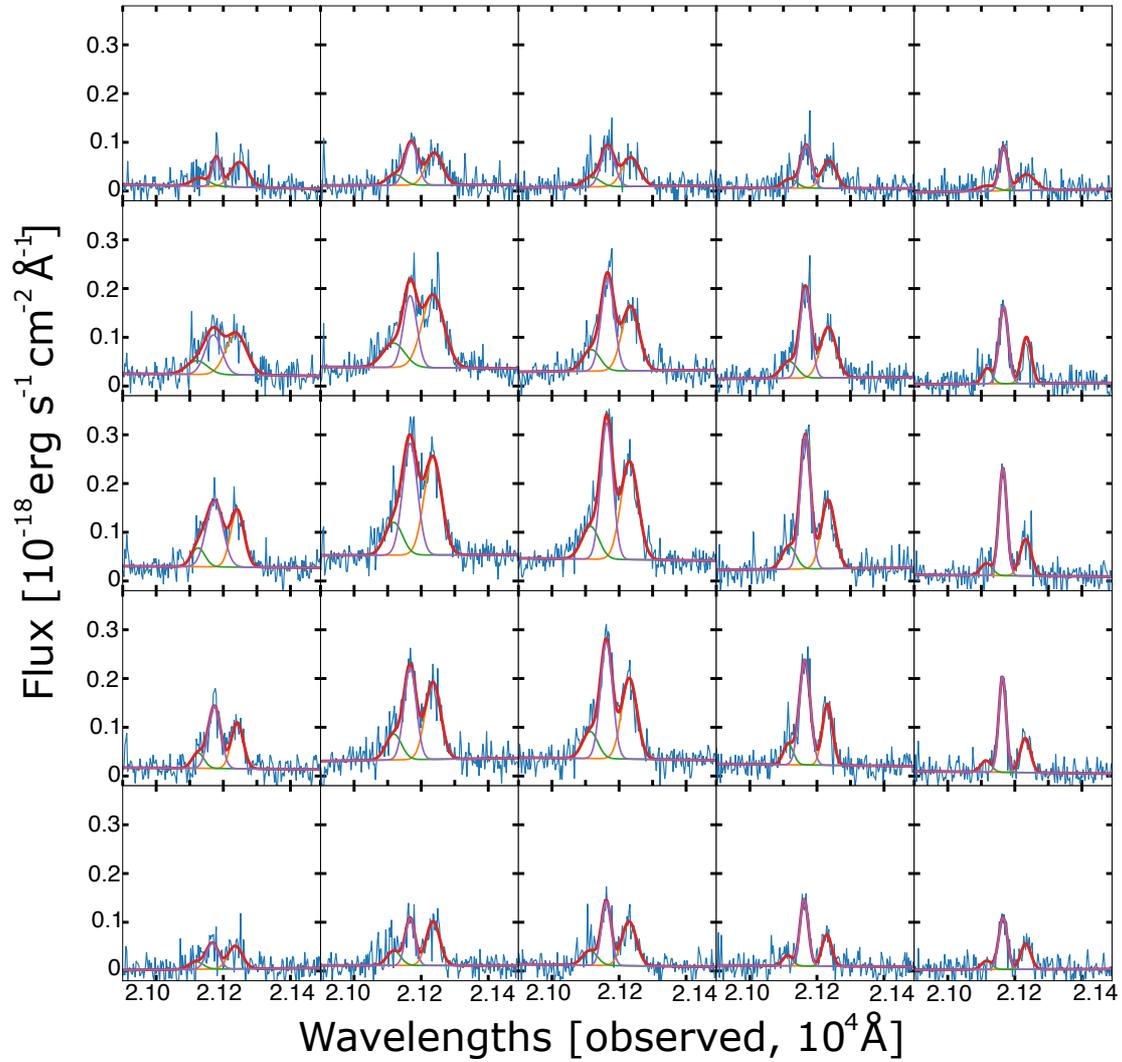
Figure 3.5: Line fit of Hα and [N II] λλ6548, 6584 (KMOS data). Each spectrum was extracted from a pixel belonging to a section of 5 × 5 pixels, which corresponds to the central region of GMASS 0953. We modelled the data (blue line) with three Gaussian components and a linear continuum (colored lines). The centroids ratio of the [N II] λλ6548, 6584 doublet and Hα was fixed to the theoretical one. We imposed the same FWHM for the nitrogen lines and their flux ratio was fixed to 1:3. The total model is overlayed in red.
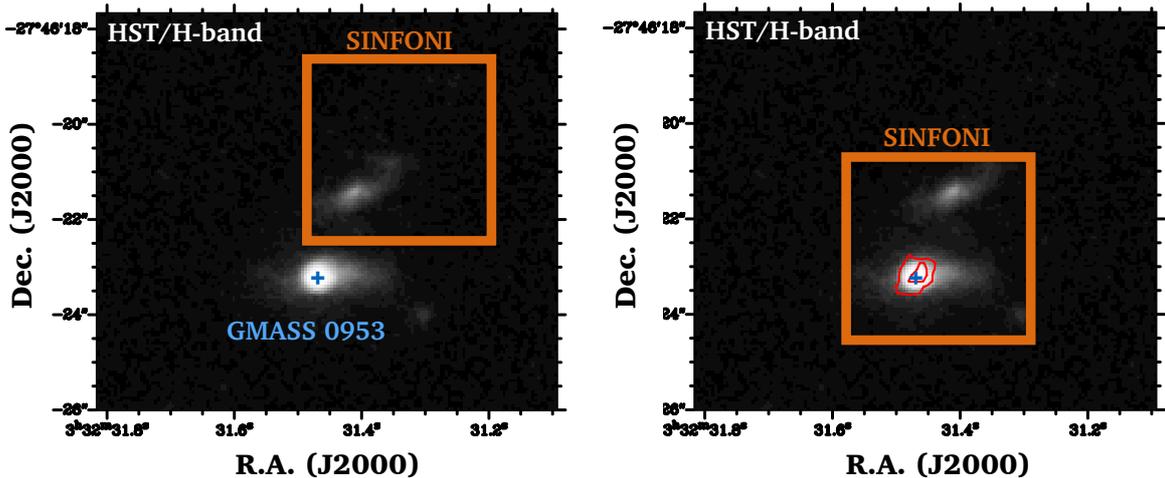
Figure 3.6: Overlap of SINFONI field of view (orange square) on the HST/H-band image of GMASS 0953 before (left panel) and after (right panel) the correction of the datacube coordinates. The red contours trace the SINFONI stacked continuum while the cross indicates the H-band surface brightness peak which we used as a reference to align the continuum peak. The source at the top is a foreground galaxy.

maps on the *HST* images (Fig. 3.6, right panel).

We verified also the astrometry of the ALMA data studied by Talia et al. (2018) (see Sect. 3.5) with respect to the *HST* images of GMASS 0953. The systematic offset between ALMA and the *HST* data in the GOODS-South is a well known problem that was underlined in many works (e.g., Maiolino et al. 2015, Dunlop et al. 2017). We applied the correction of Franco et al. (2018) determined for the object AGS13: this acronym refers indeed to GMASS 0953, which was studied also in that work. We shifted the coordinates of - 0.087″ in R.A. and + 0.291" in Dec. In this way we could correctly overlap also the dust continuum of the galaxy on the *HST* images of GMASS 0953 (Fig. 3.13).

3.4 Kinematic modelling

The SINFONI and KMOS data were used to perform a study of the kinematics of the [O III] λ5007 narrow line and Hα. The two lines show a large-scale velocity gradient that we analyzed in detail (Fig. 3.7). In particular, we worked under the hypotesis that the observed velocity gradients are due to gas rotation and we modelled the line emission as if it were produced by a rotating disc. In Sect. 3.4.3 we also discuss an alternative interpretation of the velocity gradient.

3.4.1 Signatures of an ionized disc

As suggested by an inspection of the GNIRS two-dimensional spectrum (Fig. 3.7, left panel), the [O III] λ5007 narrow line emission appears tilted along the slit, showing a large-scale velocity gradient that could be due to gas rotation. The emission extends over $\sim 3''$, corresponding to 25 kpc. This large-scale gradient has been confirmed by the pv diagram of [O III] λ5007 extracted roughly along the major axis of GMASS
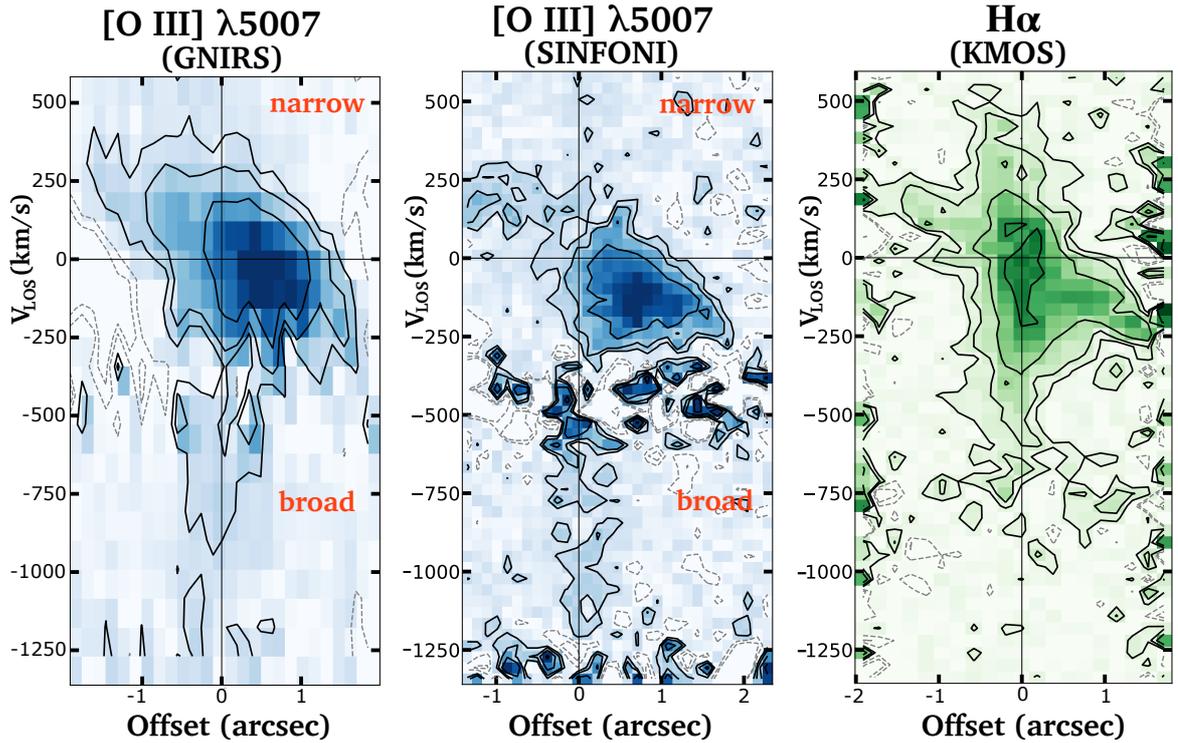
Figure 3.7: Position-velocity (pv) diagrams of [O III] λ5007 and Hα roughly along the major axis of GMASS 0953 extracted from the GNIRS two-dimensional spectrum (left), SINFONI (middle) and KMOS (right) data-cubes. Flux contour levels are at ± 2, ± 4, 8, 16σ. Both the [O III] λ5007 and Hα lines present a large-scale velocity gradient that extends up to 500 km s^{-1} at the external radii and goes far beyond in the central region. However, in the Hα case, a contamination from the [N II] $\lambda\lambda$6548, 6584 residuals is possible. The central excess up to ~ -1200 km s^{-1} presented by [O III] λ5007 in both the GNIRS and SINFONI pv diagrams corresponds to the broad blueshifted component fitted in the GNIRS one-dimensional spectrum.

0953 (see Fig. 3.1, top panel) using the SINFONI data (middle panel in Fig. 3.7). Before the extraction, the data-cube channel separation was converted into velocity after determining $\lambda_{\rm rest} = (\lambda_{50}^B + \lambda_{50}^R)/2$, i.e. the average value between the wavelengths λ_{50} where the flux of the global [O III] $\lambda5007$ profile is 50% of the peak, with 'B' and 'R' that refer to the blue and red side of the line profile respectively. This quantity was set to zero for simplicity and allowed us to fix the channel velocity spacing to Δv = 36.6 km s^{-1} at the [O III] $\lambda5007$ wavelengths[7].

The emission of the [O III] $\lambda5007$ narrow line covers about 500 km s^{-1} with the western, bright side of the galaxy moving in our direction while the eastern, dimmer part is globally redshifted. Because of an atmospheric line, it is not clear if the galaxy emission reaches velocity higher than -300 km s^{-1}, which would be hidden by the sky-subtraction. The large-scale gradient extracted from the SINFONI data is consistent with the observed velocity in the GNIRS two-dimensional spectrum, even if the latter shows a slightly higher velocity for the receding half probably because of the better sensitivity and lower spectral resolution.

As we noted in Sect. 3.3.2, in the central region of GMASS 0953 the [O III] $\lambda5007$ gradient extends up to ~ -1200 km s^{-1} (broad component in Fig. 3.7, middle panel). The interpretation of this blueshifted emission, which is not due to gas rotation, will be discussed in Sect. 3.6.

Interestingly, a large-scale velocity gradient is also shown by Hα (Fig. 3.7, right panel). The line shows a slightly asymmetric morphology, not marked as in the [O III] $\lambda5007$ case, with the redshifted half more clearly visible. The emission from the external regions shows the same velocity gradient of the [O III] $\lambda5007$ line for both sides while, in the inner part, it extends up to 500 km s^{-1} for the red half and goes far beyond on the blue side. This blueshifted emission, which extends on a smaller scale ($\sim 0.8''$, corresponding to ~ 6.7 kpc) with a velocity up to -700 km s^{-1}, highlights the presence of a possible blueshifted component also in Hα, though we point out a probable contamination from the residuals of the [N II] $\lambda6548$ subtraction. Evidence of a blueshifted component necessary to reproduce Hα and the [N II] $\lambda\lambda6548, 6584$ doublet was found by Förster Schreiber et al. (2014) and Genzel et al. (2014), who interpreted it as a nuclear outflow linked to the AGN activity of the galaxy.

A velocity gradient, extending in the same direction of the [O III] $\lambda5007$ and Hα large-scale observed gradients, is also shown by the CO(J=6-5) line, which traces a high density, compact molecular disc hosted by GMASS 0953 (Talia et al. 2018). This fact suggests that the galaxy harbors a multi-phase disc that includes both an ionized and a molecular component (see Sect. 3.5).

3.4.2   Three-dimensional disc modelling

We interpreted both the [O III] $\lambda5007$ and Hα large-scale velocity gradient as due to a rotating disc that we modelled with the publicly available software $^{\rm 3D}$BAROLO (Di Teodoro & Fraternali 2015). This is an algorithm based on the tilted-ring model (Rogstad et al. 1974) that derives rotation curves through a three-dimensional modelling of data-cubes. In this approach, the rotation velocity and the velocity dispersion are computed directly comparing the observed data-cube with an artificial one that simulates an IFS observation, avoiding the extraction of the two-dimensional velocity

---

[7]For Hα the channel velocity spacing is 39.8 km s^{-1}. The $\lambda_{\rm rest}$ value was used also to convert the wavelengths of the GNIRS two-dimensional spectrum into velocity.

field. The latter is indeed affected by beam smearing (Begeman 1987), a problem due to the low spatial resolution (e.g. atmospheric seeing) that spreads the line emission within a region on the adjacent ones. The result is that the observed velocity gradients are artificially flattened with a consequent increase of the line broadening, which makes the kinematical parameters derived from the two-dimensional velocity field less reliable (see Di Teodoro & Fraternali 2015 and Di Teodoro et al. 2016 for more details). On the other hand, a three-dimensional modelling is not affected by beam smearing because the PSF of the observation is taken into account through a convolution step, performed to build mock data with the same spatial resolution of the observed ones.

To reproduce the data, the code builds a three dimensional disc model, formed by N rings of width W, for which the parameters that minimize the residuals between the data-cube and the model-cube are calculated. These parameters, both geometrical and kinematical, are the rotation velocity $V(R)$, the velocity dispersion $\sigma(R)$, the inclination angle i (90° for edge-on discs), the position angle ϕ of the major axis, the dynamical center (x_0, y_0), the systemic velocity V_{sys}, the disc scale height z_0 and the gas surface density Σ.

We applied the algorithm to [O III] $\lambda5007$ and Hα independently, fixing all the rings parameters except $V(R)$ and $\sigma(R)$. The galaxy was divided into five rings with radii from $0.175''$ (1.5 kpc) to $1.575''$ (13.2 kpc) and a width of $0.35''$, corresponding to about half the PSF. This choice entails that $V(R)$ and $\sigma(R)$ of a ring are not fully independent of the fitted values for the closer ones. For the position angle, we chose $\phi = 94°$ after producing pv diagrams for different position angles and considering the one with the most extended emission.

The disc inclination in the ^{3D}BAROLO model was determined by comparing the shape of the Hα total flux map with synthetic maps obtained for fixed inclination angles (from 60° to 85°) using an azimuthally averaged Hα surface brightness profile (Fig. 3.8). We used the Hα line instead of [O III] $\lambda5007$ because of the higher flux of the receding half, which allows to better examine the geometry of the disc. This (by eye) comparison allowed us to exclude inclination angles lower than 70° and greater than 80° and as a fiducial average value we took $i = 75°$ for all the rings. The reliability of our choice was confirmed by the residuals between the data and the model evaluated for different inclination angles, which show a minimum corresponding to $i = 75°$. Therefore we fixed $i = 75°$ for both the [O III] $\lambda5007$ and Hα disc models. We considered the uncertainty due to the inclination angle in the range $70° < i < 80°$ when we calculated the errorbars of the [O III] $\lambda5007$ and Hα rotation velocity. However, given the high value of i, the uncertainty on the inclination does not have a big impact on the derived rotation velocity.

For the dynamical center we used the coordinates of the emission peak in the HST/H-band image while we left the disc scale height z_0 to the default value (150 pc): due to the low spatial resolution the disc scale height is unresolved, hence the thickness has a negligible effect. Finally, we adopted for the gas surface density Σ a locally averaged normalization, in which the flux in each pixel of the disc model is equalled to the flux in the corresponding pixel in the data. In this way the inhomogenities that may affect a ring, as in the [O III] $\lambda5007$ case, can be reproduced.

After setting the disc parameters as described above, we launched ^{3D}BAROLO obtaining two best-fit model-cubes that simulate the [O III] $\lambda5007$ and Hα line emission. In order to compare the disc model with the data, we inspected the pv diagrams extracted along the major axis (Fig. 3.9). The observed [O III] $\lambda5007$ and Hα emission
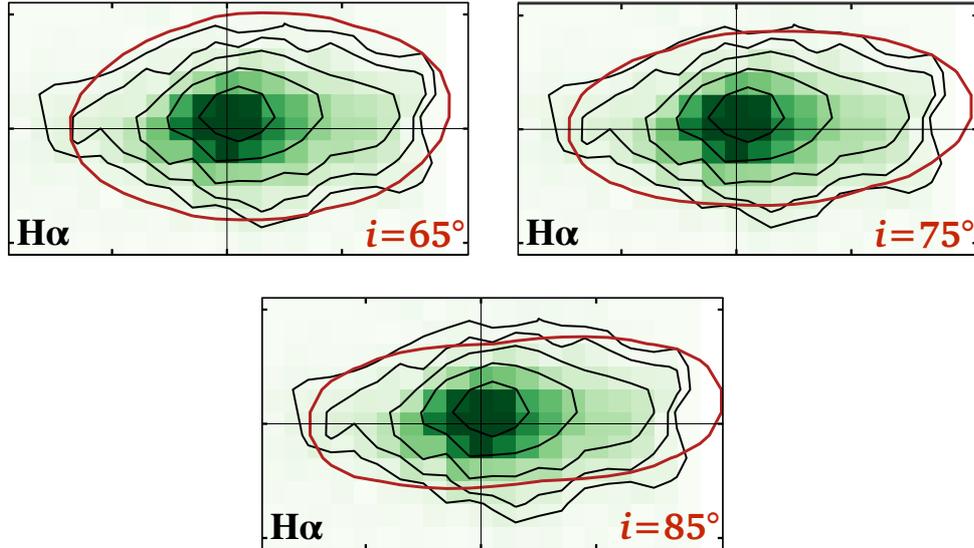
Figure 3.8: Comparison between the Hα flux map (black contour and colors) and the model maps (red contour, 3σ level) obtained using an azimuthally averaged Hα profile for fixed inclination angles. The inclination angle was varied from $i = 60°$ to $i = 85°$. We report here the models corresponding to $i = 65°$ and $i = 85°$ (top and bottom panel) and the one with $i = 75°$ (middle panel), which we fixed as the disc inclination. The more plausible inclination angles are included in the range $70° < i < 80°$ while for $i < 70°$ and $i > 80°$ the model varies significantly from the data.

is well reproduced by the model. However, some differences are present. For example, the model slightly overestimates the line broadening for both [O III] $\lambda5007$ and Hα in the outer rings ($R \sim 1.8''$) of the approaching side. The disc model also does not reproduce the emission in the central region, with possible repercussions on $V(R)$ and $\sigma(R)$ of the internal rings. This effect is particularly prominent in the Hα case.

The fitted rotation curves nicely show consistent values of $V(R)$ for the two lines in each ring (Fig. 3.10). The rotation velocity decreases between the first two rings and appears to slightly increase going outwards for both [O III] $\lambda5007$ and Hα. We note that the rise of the velocity between the second and the first ring could be intriguing, as it could be indicative of a bulge (see Lelli et al. 2016a). However, as we will see below, the errorbars associated to these rings could be not reliable. We will thus discuss in more detail the rise of the velocity in the central part of GMASS 0953 by using another tracer (see Sect. 3.5).

We assessed the reliability of the best-fit velocities simulating new model-cubes in which we varied the fitted $V(R)$ in order to visually verify if different values of the rotation velocity worsened or improved the pv diagram reproduction (see Swaters et al. 2009 for the details about a similar "trial-and-error" procedure in this context). This test was carried out adopting an azimuthal surface density profile for Σ instead of the local normalization because in this way the simulated pv diagrams present a smoothed and symmetric emission that makes it more straightforward to see variations in their shape. For both [O III] $\lambda5007$ and Hα we found that the shape of the pv diagram is not sensitive to large variations of $V(R)$ for the first two rings, meaning that the associated errorbars are underestimated. This could be due to instrumental effects,
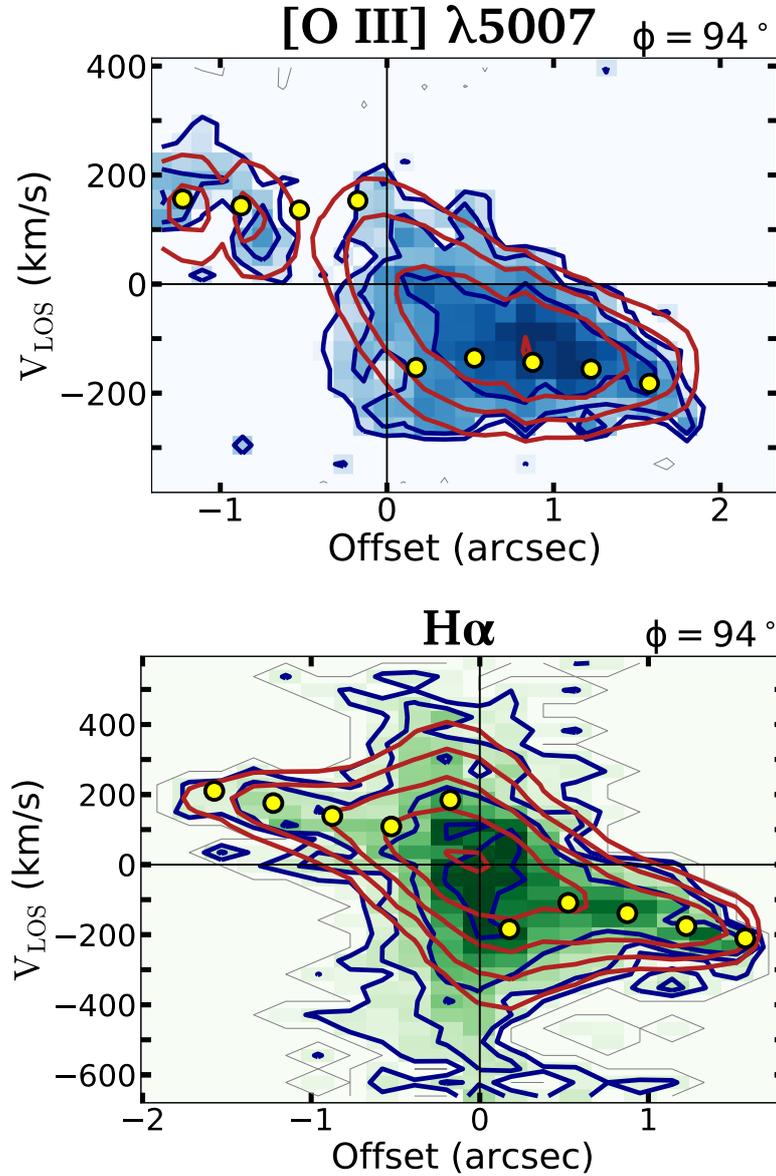
Figure 3.9: Position-velocity diagrams of the [O III] $\lambda5007$ narrow line (top panel) and Hα (bottom panel) extracted along the major axis ($\phi = 94°$) of GMASS 0953. Blue contour and colors refer to the data while the ^{3D}Barolo disc model is marked in red. Flux contour levels are at ±2, 4, 8, 16, 32σ. The yellow dots show the rotation curve projected along the line of sight.
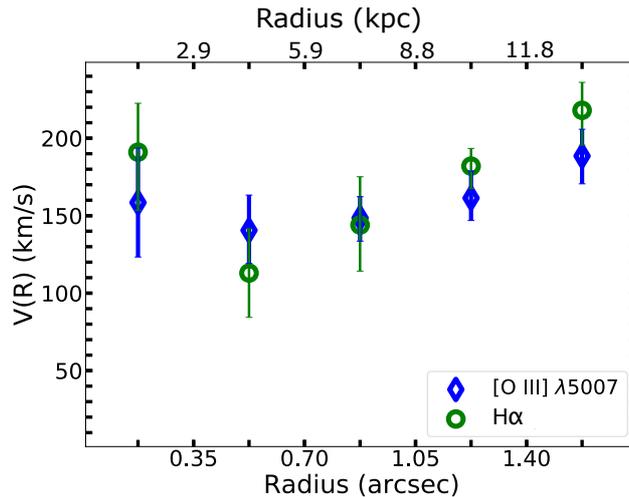
Figure 3.10: Rotation curve of [O III] λ5007 (blue diamonds) and Hα (green circles). The rotation velocity decreases between the first two rings and increases going outwards. The V(R) values are in agreement within the errors for both the lines in all the rings.

as the first two rings lie inside the same resolution element. On the other hand, we consider reliable the fitted rotation velocity and errors of the external three rings as significantly lower or higher values of $V(R)$ would not reproduce the data.

We repeated the test for the velocity dispersion $\sigma(R)$. The evaluation of this parameter is particularly complex because of the low spatial and spectral resolution of our data and the relatively high inclination of the galaxy. We could derive only an upper limit of $\sigma(R) < 160$ km s^{-1} for [O III] λ5007 and $\sigma(R) < 90$ km s^{-1} for Hα at large radii, which we obtained rejecting the $\sigma(R)$ values that do not reproduce the pv diagram.

After this analysis, as a representative rotation velocity of the disc, we took the weighted average $V(R)$ of [O III] λ5007 and Hα of the last ring ($R \sim 13$ kpc), which amounts to $V_{\rm ion} = 203^{+17}_{-20}$ km s^{-1}. The associated errors were estimated considering both the fitted ones and the uncertainties due to the inclination angle.

3.4.3 An alternative interpretation of the velocity gradient

In Sect. 3.4.2 we modelled the kinematics of [O III] λ5007 and Hα under the hypotesis that the velocity gradient of the two lines was produced by a rotating disc. This is the more straightforward assumption we can do given the limited spatial resolution of our data. However, velocity gradients in the gas kinematics can also be originated by other phoenomena. In particular, galactic-scale winds can produce velocity gradients similar to that observed in GMASS 0953, with the emission coming from the approaching/receding cone blueshifted and redshifted respectively. This can be seen in observations of local galaxies. One of the best studied cases of galactic winds in the nearby Universe concerns the starburst galaxy M82. The wind, due to vigorous star formation in the centre, has been observed in several gas phases (e.g. Schaaf et al. 1989; Shopbell & Bland-Hawthorn 1998; Leroy et al. 2015). Recently, Martini et al. (2018) investigated the kinematics of the M82 wind using HI observations resolved on the scale of 0.4 kpc. The wind extends over 10 kpc from the galaxy center and the
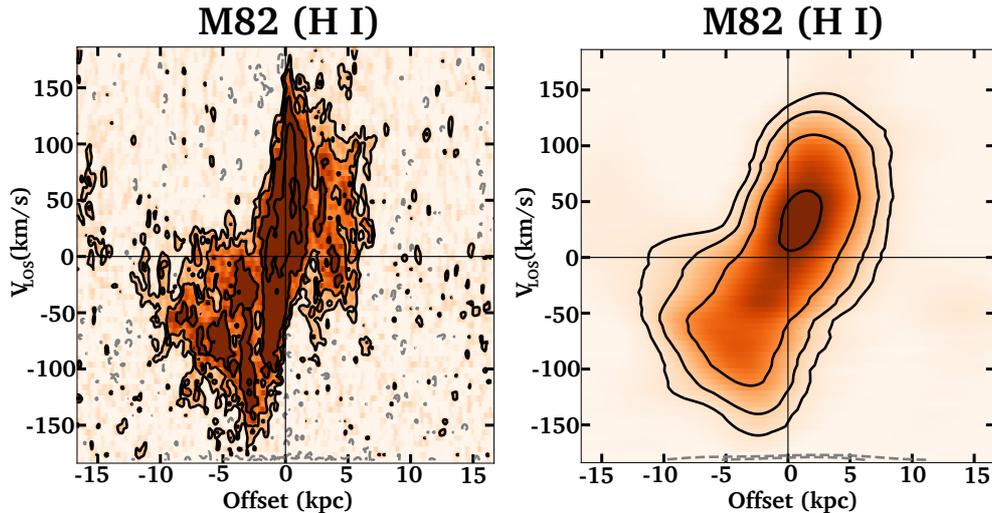
Figure 3.11: Position-velocity diagrams along the HI wind in the local starburst M82 (Very Large Array and Green Bank Telescope data; Martini et al. 2018). Left panel: original data with a spatial resolution of 0.4 kpc. Right panel: smoothed data with a spatial resolution of 4.65 kpc. The smoothed emission appears roughly similar to the observed velocity gradient of Hα and [O III] λ5007 in GMASS 0953 suggesting that the interpretation of gas velocity gradients may be ambiguous when using data of low spatial resolution.

observed pv diagram (Fig. 3.11, left panel) presents some interesting analogies with those of [O III] λ5007 and Hα in GMASS 0953 (Fig. 3.7). Clearly, a direct comparison of the pv diagrams is difficult because of the different spatial resolution of the two observations. Therefore, we smoothed the M82 data in order to have the same number of resolution elements of GMASS 0953 along the pv diagram. This corresponds to a new spatial resolution of 4.65 kpc. We found that the analogy persists after the smoothing (Fig. 3.11, right panel) in terms of the global shape of the pv diagram, the asymmetric flux distribution and the observed declining velocity from the inner to the outer regions. Despite these similarities, the above comparison is not trivial at least for two reasons: i) we are comparing two different gas phases, i.e. ionized vs neutral, which have different physical properties; ii) we are comparing a local starburst galaxy without AGN activity with a high-redshift active galaxy. Keeping this in mind, our experiment suggests that when looking at the pv diagram of [O III] λ5007 and Hα a wind interpretation cannot be ruled out with our data. However, the wind scenario appears quite unlikely in GMASS 0953 since the wind would move along the projected major axis of the galaxy and not in a perpendicular direction, as observed in other low and high-redshift sources (Heckman et al. 1990; Lelli et al. 2018). Moreover, the connection between a putative large-scale wind and the outflow described in Sect. 3.6 would remain unclear.

3.5 The multi-phase disc of GMASS 0953

From the kinematics modelling presented in Sect. 3.4.2, it emerges that GMASS 0953 may host an ionized disc extending up to $R \sim 13$ kpc with a rotation velocity $V_{\mathrm{ion}} = 203^{+17}_{-20}$ km s^{-1} at the largest radius. The existence of the disc is highlighted

by two lines analyzed independently, which show two consistent rotation curves. The Hα kinematics of GMASS 0953 was modelled also by Wisnioski et al. (2018), who found a rotation curve that is broadly consistent with our estimate at large radii, though a direct comparison between the two rotation curves is made difficult by the differences in the adopted disc modelling and beam smearing correction. The existence of extended ionized discs, dominated by rotation, have been found also in other star-forming galaxies at $z \sim 2$ with compact stellar morphology (van Dokkum et al. 2015; Wisnioski et al. 2018).

Rotation does not concern only the ionized phase of the ISM. According to Talia et al. (2018), GMASS 0953 harbors a very compact ($R_{CO} = 0.75 \pm 0.25$ kpc) molecular disc traced by the CO(J=6-5) line, with a rotation velocity $V_{CO} = 320^{+92}_{-53}$ km s^{-1}, i.e. higher although compatible at 2σ with our Hα inner value. All the three lines show velocity gradients with consistent position angle that are aligned with the major axis of the stellar component. The latter represents possibly a nearly edge-on disc that is visible in the *HST* image of the galaxy (Fig. 3.12). These findings suggest that GMASS 0953 hosts a multi-phase disc, with rotation affecting the galaxy from small to large scales and peaking in its central regions. The joint existence of a cold and an ionized disc in high-z massive galaxies was also found by Übler et al. (2018) and Herrera-Camus et al. (2019). In the very inner region of GMASS 0953, we considered $V_{CO} = 320^{+92}_{-53}$ km s^{-1} of the molecular disc a reliable measure of the rotation velocity. As we discussed in Sect. 3.4.2, the internal points of the [O III] $\lambda5007$ and Hα rotation curve are dominated by large uncertainties and they could be compatible with the CO(J=6-5) rotation. Declining rotation curves in the central part of galaxies are observed both in local and distant objects (Spekkens & Giovanelli 2006; Noordermeer et al. 2007; de Blok et al. 2008; Genzel et al. 2017). In particular, in local galaxies they have been clearly associated to the presence of large bulges (e.g. Lelli et al. 2016a).

The ionized gas also provides the $V(R)$ value on a larger scale, hence we can use it to estimate a lower limit to the dynamical mass of the galaxy. Under the hypothesis of pure circular motions, the dynamical mass contained within the radius $R \sim 13$ kpc amounts to $M_{dyn} = RV_c^2/G > (1.3^{+0.2}_{-0.3}) \times 10^{11}$ M$_\odot$ where, as the circular velocity V_c, we considered the V_{ion} value. Our estimate constitutes only a lower limit to the dynamical mass because the circular velocity V_c may be larger than the fitted rotation velocity V_{ion}. To estimate V_c both Hα and [O III] $\lambda5007$ may require an asymmetric drift correction (Binney & Tremaine 2008) that is probably negligible for CO(J=6-5) because of the gas lower temperature and velocity dispersion. We have not attempted to apply this correction due to the large uncertainties of our velocity dispersion (see Iorio et al. 2017 for the details). The lower limit for the dynamical mass results consistent with the stellar mass evaluated using SED fitting (see Sect. 3.2) and also with the upper limit of Förster Schreiber et al. (2009).

It is interesting to see where GMASS 0953 is located on the baryonic Tully-Fisher relation (McGaugh et al. 2000), which connects the baryonic content M_b to the circular velocity. The baryonic content M_b of the galaxy can be evaluated adding the stellar mass $M_\star$ to the gas mass M_g. To compute the gas budget we considered the molecular gas content M_{H_2} evaluated by Talia et al. (2018) and the ionized gas mass M_{ion} derived from the [O III] $\lambda5007$ narrow line luminosity (see Sect. 3.6.2). However, the latter amounts to $M_{ion} \simeq 8.5 \times 10^6$ M$_\odot$ if we use the observed [O III] $\lambda5007$ flux or to $M_{ion} \simeq 2.2 \times 10^8$ M$_\odot$ when correcting for dust extinction, which is in both the cases negligible respect to the molecular gas mass $M_{H_2} = (3.24 \pm 0.60) \times 10^{10}$ M$_\odot$ (Talia et al. 2018).
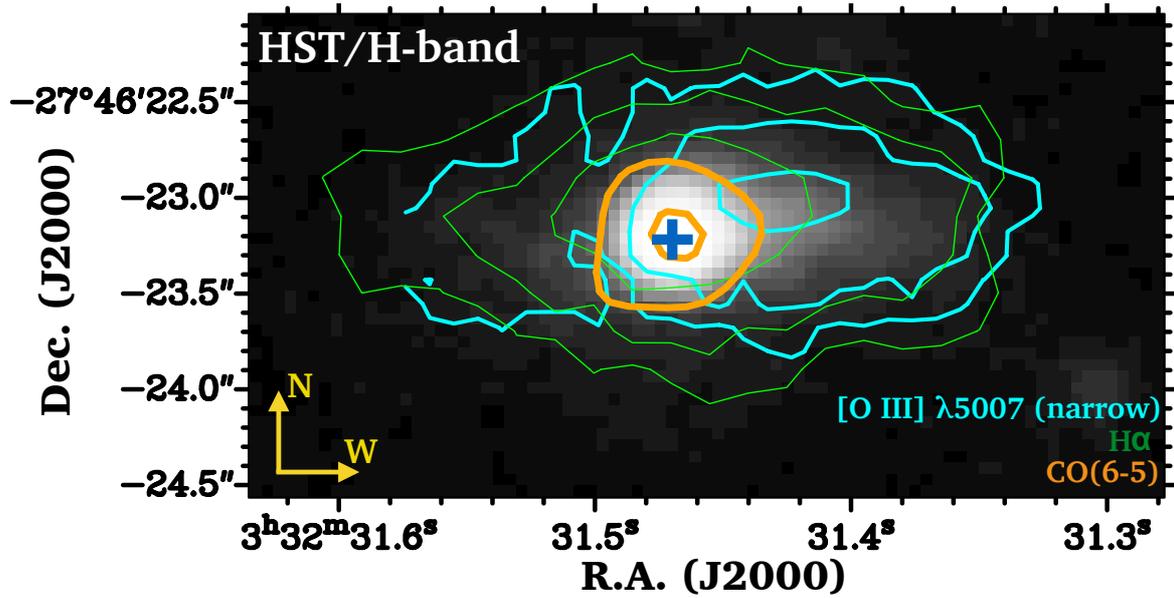
Figure 3.12: The multi-phase gas emission of GMASS 0953 overimposed on the *HST/WFC3* (*H*-band) image. The contours refer to the [O III] λ5007 narrow line (cyan), Hα (green) and CO(J=6-5) (orange, ALMA data; Talia et al. 2018). The lowest contour level is at 3σ. The cross indicates the galaxy center.
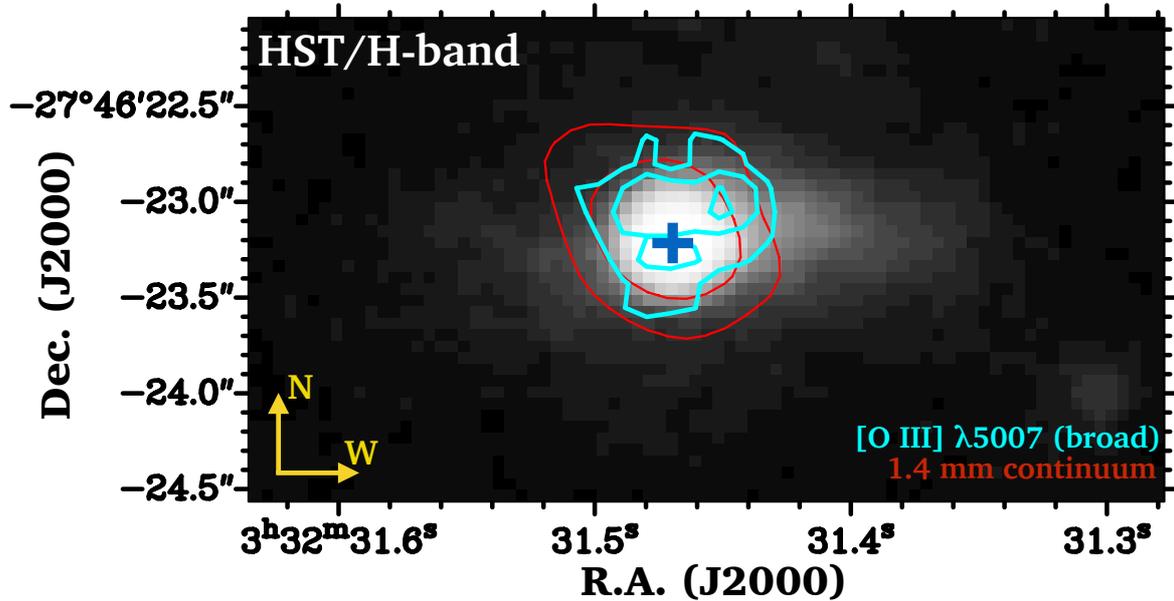
Figure 3.13: Comparison between the [O III] λ5007 blueshifted line (cyan) and the dust continuum (red, ALMA data; Talia et al. 2018). The two emissions are both concentrated near the center of GMASS 0953, marked with a cross.

We hence computed the baryonic mass as $M_{\rm b} \simeq M_{\star} + M_{\rm H_2} = (1.47 \pm 0.12) \times 10^{11}$ M$_\odot$. For the circular velocity we used again $V_{\rm ion}$ at 13 kpc. If we put these two values on the local baryonic Tully-Fisher relation of Lelli et al. (2016b), we find that GMASS 0953 is well included into the 0.11 dex scatter of the $z = 0$ relation (Fig. 3.14). This result suggests that massive galaxies that are already relaxed at $z \gtrsim 2$ may exist, in agreement with the findings of Lelli et al. (2018).

3.6   Probing the AGN feedback in action

3.6.1   Evidence of an AGN-driven ionized outflow

We know, from what we discussed in Sect. 3.3, that the [O III] $\lambda5007$ line consists of a narrow component, which we used to model the kinematics, and a broad blueshifted wing fitted in the GNIRS spectrum that is not ascribable to the rotating disc (Fig. 3.2 and Fig. 3.7). The emitting region appears concentrated near the nucleus of GMASS 0953 (Fig. 3.3, right panel).

It is interesting to evaluate the size and the velocity of the [O III] $\lambda5007$ blueshifted emission. We computed the size of the emitting region through a two-dimensional Gaussian fit on the SINFONI map. The emission appears barely resolved, with a FWHM of the major axis of $\sim 0.8''$, corresponding to 6.7 kpc. The velocity can be evaluated from the line fit of the GNIRS spectrum. We measured the velocity shift between the line centroids of the broad and the narrow [O III] $\lambda5007$ line to be $\Delta v = -535 \pm 152$ km s^{-1}.

Line velocity offsets in galaxies are often connected to outflowing gas due to stellar winds or supernova explosions. However, the typical offset in these cases amounts to $|\Delta v| \sim 100$ km s^{-1}(e.g. Shapley et al. 2003; Steidel et al. 2010; Talia et al. 2012), which is considerably lower than our value. Conversely, velocity offsets $\Delta v \sim -500$ km s^{-1} have been found in [O III] $\lambda5007$ blueshifted emission extending on several kpc in many high-z active galaxies (e.g. Cano-Díaz et al. 2012; Harrison et al. 2012; Carniani et al. 2015b; Brusa et al. 2015). These high-velocity kpc-scale emissions are actually interpreted as robust tracers of AGN-driven outflows and represent an observational evidence of the AGN feedback in action. They are also characterized by line widths > 1000 km s^{-1}, compatible with the FWHM ~ 1400 km s^{-1} of the [O III] $\lambda5007$ blueshifted line detected in our data. Finally, also the emitting region, located close to the nucleus GMASS 0953, yet supports the AGN activity as the main engine of gas expulsion in this galaxy.

The [O III] $\lambda5007$ blueshifted line therefore highlights the presence of an AGN-driven ionized outflow that affects GMASS 0953, suggesting that the AGN feedback is likely at work in this galaxy. A further support to the presence of outflowing material in the ionized phase may come from the blueshifted Hα emission in the central part of the galaxy visible in the pv diagram (Fig. 3.7, right panel; see also Förster Schreiber et al. 2014; Genzel et al. 2014). Moreover, the FORS2 rest-frame UV spectrum of GMASS 0953 presents absorption lines (e.g. C II $\lambda1334$, Si $\lambda1260$) that are blueshifted of -800 km s^{-1} respect to the systemic velocity (Cimatti et al. 2013). This fact suggests the presence of outflowing material also in a lower ionization state than that traced by [O III] $\lambda5007$ and Hα. Finally, there is a tentative evidence of a blueshifted wing affecting also the CO(J=6-5) line with $\Delta v \sim -700$ km s^{-1} with respect to the main component, which might be due to outflowing material in the molecular phase (Talia et al. 2018).
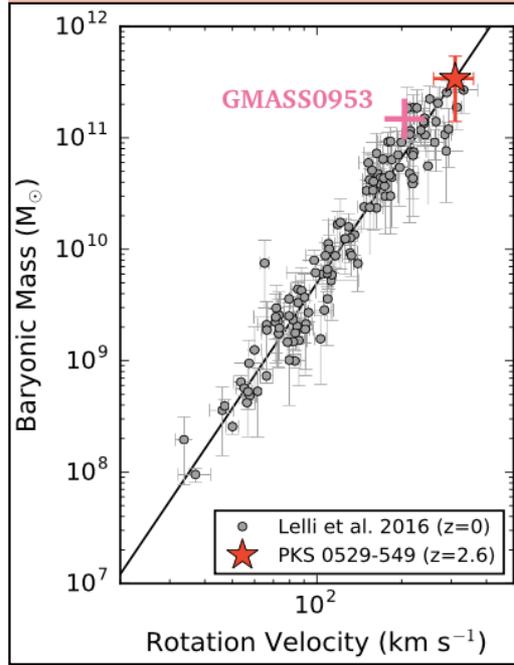
Figure 3.14: Baryonic Tully-Fisher relation found by Lelli et al. (2016b) in nearby galaxies. We see that GMASS 0953 lie onto the $z = 0$ relation, suggesting that at $z \sim 2$ there are galaxies already relaxed. Figure adapted from Lelli et al. (2018).

However, the low significance of the detection ($2.5\ \sigma$) prevents us to make a reliable analysis of this component hence, to state the effects of gas expulsion on the galaxy, we considered the ionized phase only.

3.6.2 Impact of the outflow on the host galaxy

Outflow rate

Because of the presence of outflowing gas, it is interesting to evaluate the mass of the expelled material per unit time (i.e. the outflow rate) in order to compare it with the SFR of GMASS 0953. Many studies observed AGN-driven winds in local galaxies with outflow rates that may exceed the SFR (Rupke & Veilleux 2011; Cicone et al. 2014) and influence the star formation activity by removing large amounts of gas.

We followed the approach of Cano-Díaz et al. (2012) and Carniani et al. (2015b), who derived the outflow rate of the ionized gas from the luminosity of the [O III] $\lambda 5007$ blueshifted emission. We started evaluating the outflow mass, i.e. the total mass of the ionized gas expelled, from the luminosity of the [O III] $\lambda 5007$ blueshifted component. The luminosity of the [O III] $\lambda 5007$ can be written as

$$L_{[\text{O III}]} = \epsilon_{\lambda 5007} f V_{\text{of}} \tag{3.1}$$

where $\epsilon_{\lambda 5007}$ is the line emissivity, V_{of} the total volume occupied by the ionized outflow and f is the filling factor, i. e. the ratio between the volume of the [O III] $\lambda 5007$ emitting gas and the total volume: we worked indeed under the hypotesis that [O III] is produced by a fraction of the outflowing ionized gas. We used the emissivity value reported by Cano-Díaz et al. (2012) for a temperature $T = 10^4$ K:

$$\epsilon_{\lambda 5007} = 1.11 \times 10^{-9} h \nu_{\lambda 5007} n_{\text{O}^{2+}} n_{\text{e}} \quad [\text{ erg s}^{-1}\text{cm}^{-3}] \tag{3.2}$$

where $n_{O^{2+}}$ is the number density of the doubly ionized oxygen and n_e the electron number density. Under the reasonable assumption that all the oxygen is in the ionized form, we can espress $n_{O^{2+}}$ as

$$n_{O^{2+}} = \frac{n_O}{n_H}\frac{n_H}{n_e}n_e \qquad (3.3)$$

where n_O and n_H are the neutral oxygen and hydrogen number densities. The electron number density n_e can be written as $n_e \approx n_{H^+} + 1.5n_{He}$ for a helium mixture made up by equal parts of He^+ and He^{++} (Osterbrock & Ferland 2006). Since the number density of the ionized helium n_{He} is in good approximation $0.1n_{H^+}$, under the hypothesis that $n_H \approx n_{H^+}$, Eq. (3.3) becomes

$$n_{O^{2+}} = \frac{n_O}{n_H}(1.15)^{-1}n_e = 10^{\log\left(\frac{n_O}{n_H}\right)_\odot}10^{\left[\frac{O}{H}\right]}(1.15)^{-1}n_e \qquad (3.4)$$

where $\left[\frac{O}{H}\right] \equiv \log\left(\frac{n_O}{n_H}\right) - \log\left(\frac{n_O}{n_H}\right)_\odot$ is the metallicity. Substituting Eq. (3.4) in Eq. (3.2) and Eq. (3.1) we obtain

$$L_{[O\ III]} = 4.727 \times 10^{-13}h\nu_{\lambda5007}n_e^2 10^{\left[\frac{O}{H}\right]}fV_{of} \quad [\text{ erg s}^{-1}] \qquad (3.5)$$

We used for the oxygen abudance of the sun $(n_O/n_H)_\odot$ the value of Asplund et al. (2009). If we neglect the elements heavier than helium, the ionized gas mass M_{of} of the [O III] $\lambda5007$ emitting clouds is essentially given by

$$M_{of} = (n_{H^+}m_p + n_{He}m_{He})fV_{of} \qquad (3.6)$$

where m_p and m_{He} are the proton and helium mass. Since $m_{He} \approx 2m_p$ and expressing n_{H^+} and n_{He} in terms of n_e, Eq. (3.6) becomes

$$M_{of} = 1.04\ n_e m_p fV_{of} \qquad (3.7)$$

which combined with Eq. (3.5) gives

$$M_{of} = \frac{1.04\ m_p}{4.727 \times 10^{-13}h\nu_{\lambda5007}n_e 10^{\left[\frac{O}{H}\right]}}L_{[O\ III]} \quad [\text{ g }] \qquad (3.8)$$

We measured the electron number density n_e from the [S II] $\lambda\lambda6716, 6731$ line ratio (see Sect. 3.3.1). The metallicity was derived using the mass-metallicity relation of Wuyts et al. (2016) and amounts to $\left[\frac{O}{H}\right] = \log(0.9)$ for a stellar mass of 10^{11} $M_\odot$.

We note that using [O III] $\lambda5007$ as a mass tracer of the outflowing gas implies several uncertainties since the derived outflow mass is sensitive to the ionization state and to the metallicity of the gas. The latter cannot be directly measured from the optical line ratios of GMASS 0953 because of the presence of the AGN and we resort to using the mass-metallicity relation (Wuyts et al. 2016) while the ionization state has been assumed. On the other hand, hydrogen lines such as Hβ and Hα are better mass tracers because they do not depend on these quantities (see Harrison et al. 2018). However, we do not find evidence of a blueshifted wing in the Hβ profile probably because of the low S/N and the weakness of the emission. In the case of Hα we highlighted in Sect. 3.4 the presence of outflowing material possibly shown also by this line; however, the Hα emission suffers from possible contamination of the [N II] $\lambda\lambda6548$, 6584 lines (see Sect. 3.3.3) and from the AGN broad line region (see also Brusa et al. 2015). For these reasons we do not use Hα to derive the outflow properties.

3.6 Probing the AGN feedback in action

The outflow mass was estimated in two ways: with and without applying the dust extinction correction to the [O III] $\lambda5007$ luminosity. As seen in Sect. 3.3.1 GMASS 0953 is highly obscured, hence it seems reasonable to consider both scenarios. To evaluate the intrinsic [O III] $\lambda5007$ flux, we used the color excess $E(B-V) = 0.8 \pm 0.3$ derived from the Hα and Hβ line ratio assuming a Calzetti et al. (2000) extinction curve. The resulting ionized outflow mass M_{of} in the extinction corrected case amounts to $M_{\mathrm{of}} \simeq 1.2 \times 10^8$ M$_\odot$. Without the extinction correction this quantity drops to $\simeq 4.3 \times 10^6$ M$_\odot$.

Once we have the outflow mass we can evaluate the outflow rate, i.e. the ionized gas mass expelled per unit time. In order to calculate it, we adopted a simple geometrical model to describe the outflow, as done by Cano-Díaz et al. (2012), where the material is distributed in a conical region with an opening angle Ω and radius R_{of} and is expelled in a direction almost perpendicular to the galaxy disc with a velocity v_{of}. Under this assumption, the outflow rate can be written as

$$\dot{M}_{\mathrm{of}} = \rho |v_{\mathrm{of}}| \Omega R_{\mathrm{of}}^2 \qquad (3.9)$$

where ρ is the mass density of the ionized gas and v_{of} the outflow velocity. Assuming that the ejected material is located in a volume $V_{\mathrm{of}} = \frac{4}{3}\pi R_{\mathrm{of}}^3 \frac{\Omega}{4\pi}$ and simply writing ρ as $\rho = M_{\mathrm{of}}/V_{\mathrm{of}}$, Eq. (3.9) becomes

$$\dot{M}_{\mathrm{of}} = 3 M_{\mathrm{of}} \frac{|v_{\mathrm{of}}|}{R_{\mathrm{of}}} \qquad (3.10)$$

by which it is possible to estimate the outflow rate of the ionized gas.

We estimated the outflow velocity v_{of} from the line fit of the GNIRS spectrum. There is no general consensus on how to define outflow velocities (see Harrison et al. 2018). In our analysis we followed the approach of Rupke et al. (2005), who defined the outflow maximum velocity as $v_{\mathrm{of}} = \mathrm{FWHM}_{\mathrm{broad}}/2 + |\Delta v|$, where the first term is half the FWHM of the [O III] $\lambda5007$ blueshifted component and Δv is the velocity offset between the [O III] $\lambda5007$ narrow and blueshifted component. The resulting velocity amounts to $v_{\mathrm{of}} \sim 1200$ km s^{-1}. Using this v_{of} value in Eq. (3.10) we are implicitly assuming that all the outflowing material is moving at this velocity. This could be possible due to projection effects, supported by the high inclination of the galaxy (see also Cano-Díaz et al. 2012; Brusa et al. 2015; Cresci et al. 2015). We note that using a more conservative definition of v_{of}, relying on the velocity offset $|\Delta v| \sim 530$ km s^{-1}, the outflow rate would be reduced at most by a factor ~ 2 and our results would not be considerably modified. Finally, we used as the outflow radius R_{of} half the FWHM of the emitting region visible in the SINFONI map, which amounts to $R_{\mathrm{of}} \simeq 3.3$ kpc (see also Harrison et al. 2012, 2014). Substituting these values in Eq. (3.10) and using the extinction corrected outflow mass, we found an ionized outflow rate $\dot{M}_{\mathrm{of}} \sim 120$ M$_\odot$yr^{-1} that drops to ~ 6 M$_\odot$yr^{-1} if the outflow is not extincted by dust.

An indication of whether the outflow is affected or not by dust obscuration may come from the 1.4 mm continuum of GMASS 0953 (Talia et al. 2018), which is a robust tracer of dust. After applying an astrometric correction (see Sect. 3.3.4), we overlapped the dust continuum map on the outflow emission detected with SINFONI (Fig. 3.13). Interestingly, the dust and the [O III] $\lambda5007$ blueshifted component emit in the same region. Therefore, it is plausible that the [O III] $\lambda5007$ luminosity may be dimmed by the dust along the line of sight, though it is also possible that the outflow may have already escaped the dusty region of the galaxy because of the high velocity.

Apart from the extinction correction and the adopted assumption about the outflow velocity, it should be noted that other uncertainties affect the outflow rate. The derivation of the outflow mass $M_{\rm of}$ that enters Eq. (3.10) requires the knowledge of the electron number density of the gas. This quantity was derived from the [S II] $\lambda\lambda6716$, 6731 line ratio and amounts to 500 cm^{-3} (see Sect. 3.3.1). Unfortunately, the [S II] $\lambda\lambda6716$, 6731 emission is produced by the galaxy ISM and not by the wind since we did not find evidence of a broad component in the [S II] $\lambda\lambda6716$, 6731 line fit likely because of the low S/N. Finally, we remind that we assumed a conical outflow for simplicity, but the true geometry is not known.

Depletion timescale

In order to properly gauge the impact of the AGN feedback on GMASS 0953 a comparison between the depletion timescale due to star formation with that associated to gas ejection is necessary. The former amounts to $\tau_{\rm dep}^{\rm SF} = M_{\rm H_2}/{\rm SFR} \sim 150$ Myr (Popping et al. 2017; Talia et al. 2018). The depletion timescale due to the outflow can be evaluated as the ratio between the mass of the ionized gas and the outflow rate, i.e. $\tau_{\rm dep}^{\rm OF,ion} = M_{\rm ion}/\dot{M}_{\rm of} \sim 2$ Myr (extinction corrected case). This very short value would mean that our observations were extremely unlikely, given cosmological timescales. However, if the outflowing material is supplied by the internal gas reservoir (dominated by the molecular phase) of the galaxy, the depletion timescale increases, as the total gas mass is much higher than $M_{\rm ion}$. Under the assumption that the outflow is depleting the whole ISM, we can write the depletion timescale as $\tau_{\rm dep}^{\rm OF,mol} \approx M_{\rm H_2}/\dot{M}_{\rm of}$, which is ~ 270 Myr using again the extinction corrected [O III] $\lambda5007$ luminosity. We note that this value of $\tau_{\rm dep}^{\rm OF,mol}$ represents an estimate of the depletion timescale in the central region only, since the molecular gas is concentrated within a radius of 1 kpc (Talia et al. 2018). From the comparison of the depletion timescales, it appears that the AGN-driven outflow and the star formation activity contribute in a similar way in depleting the gas reservoir of the galaxy. We note however that the outflow would be much less effective in consuming the gas if the not-extincted value of the [O III] $\lambda5007$ luminosity were considered. Using the not-extincted luminosity we obtain indeed a depletion timescale $\tau_{\rm dep}^{\rm OF,mol} \sim 5.4$ Gyr, meaning that the AGN-driven outflow is negligible compared to the star formation activity. Moreover, the latter may also drive galactic winds that would provide an additional contribution to gas consumption from star formation (Heckman & Thompson 2017).

Apart from the extinction correction, another important uncertainty affects the outflow depletion timescale. We considered in the evaluation $\tau_{\rm dep}^{\rm OF,mol}$ the contribution of the ionized outflow only. Many studies show that this phase cannot be the dominant constituent of AGN outflows (Fiore et al. 2017); in particular, molecular outflows were found to be up to two orders of magnitude more massive than ionized outflows in active galaxies where both the phases have been observed (Carniani et al. 2015b). As we mentioned in Sect. 3.6.1, we did not find evidence of outflowing material in the molecular phase except for a feature of 2.5σ blueshfted from the CO(6-5) main line. The ALMA data can be used to set an upper limit to the molecular outflow rate of GMASS 0953. We stacked the channels between -500 km s^{-1} and -1200 km s^{-1}, corresponding to the outflow emission in the SINFONI data (see Fig. 3.7, middle panel), in order to derive a 3σ upper limit to the flux density of the CO(6-5) outflow ($S_{\rm CO}^{3\sigma} = 79$ mJy, assuming the outflow has the same size of the ionized one; see also Brusa et al. 2018). This value was converted in H$_2$ mass using the same assumptions of Talia et al. (2018).

We hence derived an upper limit to the molecular outflow rate using Eq. (3.10) and adopting the same velocity of the ionized outflow. The upper limit to the molecular outflow rate amounts to ~ 2500 $M_\odot yr^{-1}$. This means that our observation does not allow us to detect outflow rates below this quantity, which can potentially contribute to gas consumption.

From the reported analysis we conclude that the role played by the AGN feedback in GMASS 0953 is quite unclear. Further investigation of this object is thus necessary to assess if the gas ejection could significantly impact the gas reservoir of this galaxy or not. However, despite the aforementioned uncertainties, GMASS 0953 appears a promising candidate to quench the star formation activity in a total depletion timescale $\tau_{\rm dep}^{\rm TOT} = M_{\rm H_2}/(SFR + \dot{M}_{\rm of}) \sim 10^8$ yr (see also Brusa et al. 2018) if the accretion from external gas is shutdown. This estimate is valid in both the extinction corrected/not-corrected case.

Chapter 4

Star formation inside galactic outflows[1]

4.1 Observations of stars inside AGN and star formation-driven outflows

4.1.1 Studies based on nebular emission lines

We discussed in Chapter 1 that AGN can affect the host galaxies by driving galactic outflows, which may suppress or trigger star formation. The latter process can happen in two modes. On one side, we have the classical positive feedback mechanism, already observed in the Milky Way and in distant galaxies, in which star formation is powered in the ambient medium due to shocks produced by winds or radio jets (Bicknell et al. 2000; Zavagno et al. 2010; Cresci et al. 2015; Baug et al. 2018). On the other hand, more recent models predict star formation inside AGN driven outflows via compression and cooling of the outflowing material (Ishibashi & Fabian 2012; Zubovas et al. 2013a; Silk 2013).

From the observational point of view, positive feedback is difficult to observe mainly for two reasons. The first one is that the putative presence of stars formed inside outflows is sought by looking at optical flux ratios of nebular emission lines using diagnostic diagrams (e.g., BPT diagrams; Baldwin et al. 1981), which should be consistent with ionization from star formation. However, the presence of a strong AGN could easily dominate these diagrams, concealing the ionization from young stars (see Gallagher et al. 2019). The second reason is that the stars formed in the outflow may quickly decelerate due to the gravitational potential of the galaxy and fall back onto the disc, becoming difficult to distinguish from the stars inside it. Because of these difficulties, only a few observations of this star formation mode have been reported in low-z galaxies.

The first evidence of positive feedback has been found by Maiolino et al. (2017) in a nearby starburst galaxy hosting an AGN. The optical and NIR emission line ratios observed in the outflow are indeed consistent with ionization from young stars rather than from the AGN. Also the high value of the ionization parameter in the outflow is consistent with ionization from stars inside the outflowing gas, rather than from the galaxy disc. However, this study is based on one object only and thus it does not allow to assess how relevant positive feedback is among the overall population of galaxies.

A statistical approach to address this issue has been adopted by Rodríguez del Pino et al. (2019) and Gallagher et al. (2019), who studied the ionization properties of AGN and star formation-driven outflows using spatially resolved MaNGA data. Both

---

[1]Based on Loiacono F., et al., A&A, in preparation.

studies suggest the existence of a significant fraction of star formation inside ionized outflows. In particular, Gallagher et al. (2019) found that one third of the outflows in their sample appear to be ionized by stars inside them. Therefore, the formation of stars in galactic outflows could be a fairly common process in galaxies.

4.1.2 The C III λ1176 absorption line as a reliable tracer of young stars

Despite the substantial progress that has been made in studying star formation inside outflows, the actual works are affected by a caveat since they are based on an indirect evidence of stars, as their presence is inferred by the line properties of the outflowing gas. The ultimate, unambiguous evidence of this new mode of star formation would come from the direct detection of stars newly formed inside the outflows.

An unambiguous tracers of young stars is provided by the C III λ1176 absorption line (hereafter C III) at UV-wavelengths. This line is produced by stellar photospheres of young O-B stars (Heap et al. 2006; Pellerin et al. 2002). Since its absorption arises from an excited level, this line is relatively easy to excite in the high-density environment of stellar photospheres. Conversely, the excitation of this transition is particularly difficult in the ISM. For this reason, the C III line provides a reliable tracer of young stars. At the moment there are no studies systematically investigating this feature, in order to unveil young stars inside galactic outflows.

With the purpose of further exploring this topic, we present in this Chapter a systematic analysis of the C III absorption line in a sample of 70 star-forming galaxies. Some of the objects in our sample are luminous-infrared galaxies and/or host an AGN based on the MIR and X-rays properties of their emission. We used high-resolution UV spectra to unveil possible blueshifted C III absorption, likely associated to stars newly formed in the outflowing gas.

This Chapter is organized as follows. In Sect. 4.2 we present the sample and describe the methods that we used to measure the C III velocity. In Sect. 4.3 we show the results of our analysis. Finally, we present interesting developments of this study in Sect. 4.4.

In this Chapter we adopt a ΛCDM cosmology using $\Omega_{\Lambda} = 0.7$, $\Omega_{M} = 0.3$ and $H_0 = 70$ km s^{-1}Mpc^{-1}.

4.2 Data analysis

4.2.1 The sample

We exploited the *Hubble Spectroscopic Legacy Archive* (HSLA) to search for high-resolution UV spectra of star-forming galaxies. The spectra were obtained using the Cosmic Origins Spectrograph (COS) mounted on the Hubble Space Telescope (HST) and they have been already reduced. We selected observations obtained with the G130M grating, which has a resolving power ~ 12000 at the C III wavelength $\lambda = 1176$Å.This corresponds to a spectral resolution of about 25 km s^{-1}. In addition, the COS aperture has a diameter of 2.5 arcsec, corresponding to 4 kpc at $z = 0.087$, that is, the average redshift of the galaxies in our sample.

We selected the spectra of star-forming galaxies where the C III line is clearly detected and for which COS was pointed towards the nuclear region. The latter criterium has been adopted for two reasons: the first one is that the central parts of the galaxies are the regions where AGN and starburst driven outflows are expected; the second one is that for this part we can neglect the effects of galaxy rotation on the stars motion. In this way, we ended up with a sample of 70 galaxies in which we analyzed the C III profile.

Then, we determine the systemic redshifts of the sources by using ancillary data. We exploited the 7th and 9th data release (DR7 and DR9) of the Sloan Digital Sky Survey (SDSS) which provided us with the spectrospic redshifts for 58/70 galaxies. For the remaining 12 sources we found the redshifts from the literature and using the Simbad and NED databases. These redshifts are based mostly on cold gas tracers (i.e., the core of the CO line or HI), which should be little affected by outflows and hence should provide robust measurements of the systemic velocity of a galaxy.

Finally, for the 58 sources in the DR7 and DR9 database, we used the optical line ratios to determine the presence of AGN activity based on BPT diagrams (Baldwin et al. 1981; Kauffmann et al. 2003; Kewley et al. 2006). We found that none of these galaxies presents any strong AGN feature according to the diagrams. However, we cannot exclude the presence of obscured AGN in our sample, whose activity is hidden in the BPT diagrams but visible at other wavelengths. For instance, this is the case of ESO 148-2 (Maiolino et al. 2017), a source that, according to the optical spectral type reported by Veilleux et al. (2013a), lies in the star-forming region of the BPT. Nevertheless, an obscured AGN was inferred from the X-rays luminosity (Brightman & Nandra 2011). We found that based on the MIR properties of the spectral energy distribution and/or polycyclic aromatic hydrocarbon (PAH) emission at 6.2 μm, there are three more AGN in our sample (NGC6090, IRAS 15250+3609, Mrk231; see Dietrich et al. 2018; Stierwalt et al. 2013). In case of NGC 6090 the AGN activity is weak and produces only the 26% of the infrared luminosity of the galaxy (Dietrich et al. 2018). Based on the low PAH equivalent width there is one further source (Haro 11) in our sample that could host an AGN. However, this is a low mass galaxy for which the low metallicity is likely responsible of the low PAH emission rather than the AGN activity. We found another AGN (SDSS J123645.51+261803.7) in the quasar catalog of Souchay et al. (2015). Therefore, the total number of AGN in our sample is five.

4.2.2 Measurement of the C III velocity

We describe in the next paragraphs the procedure that we used to estimate the C III line velocity. The procedure is based on the cross-correlation between the C III line and a library of templates and was divided in four main steps, which we present as follows:

Step 1: Library of templates

First of all, we built a library of templates, which we used as a reference to measure the C III line velocity. The library is based on COS spectra of star-forming galaxies. The advantage of using COS spectra of star-forming galaxies to build our library is that any instrumental effect is nicely taken into account in the measurement of the C III velocity. Secondly, this method avoids any assumption about the line shape and the

Table 4.1: List of the 70 galaxies in our sample. The RA and Dec column refer to the coordinates of the COS pointings. The references reported in the last column refer to redshift, type and SFR respectively. We marked with a * the sources with a broad C III profile that we excluded from the statistical analysis (see Sect. 4.3).

Name	R.A. (deg)	Dec. (deg)	z	Best shift ($\mathrm{km\,s^{-1}}$)	Median shift ($\mathrm{km\,s^{-1}}$)	$\log(\mathrm{SFR/M_\odot yr^{-1}})$	Type	Ref.
ESO148-2	348.94543	59.05404	0.0448	-19 ± 37	-7^{+36}_{-26}	2.06	AGN	a, b, c
IRAS 08339+6517*	129.596	65.1209	0.01918	-69 ± 8	-69^{+6}_{-10}	1.85	NO AGN	d, e, d
IRAS 16487+5447	252.446	54.7098	0.1038	-164 ± 54	-187^{+49}_{-35}	2.26	NO AGN	f, g, h
IRAS 23133-4251*	349.045	-42.5849	0.00536	35 ± 48	35^{+43}_{-48}	1.76	NO AGN	i, e, e
IRAS F10257+4339*	156.964	-43.9034	0.00926	121 ± 26	130^{+22}_{-21}	1.74	NO AGN	j, j, j
KISSR 2110	242.046	43.6317	0.028808	73 ± 36	81^{+44}_{-23}	-0.3	NO AGN	k, l, l
KISSR 242	199.016	29.3816	0.03779	27 ± 23	29^{+20}_{-16}	0.71	NO AGN	l, m, n
KISSR271*	200.42	28.8831	0.023	-46 ± 74	-73^{+49}_{-84}	-0.1	NO AGN	l, l, l
M 31	10.6848	41.2689	-0.001	-7 ± 90	6^{+99}_{-72}	-0.43	NO AGN	NED, o, p
MRK 231	194.059	56.8735	0.0422	-160 ± 36	-163^{+24}_{-42}	2.23	AGN	q, q, j
NGC 3125-1	151.639	-29.9352	0.003703	-33 ± 33	-33^{+21}_{-19}	-0.33	NO AGN	r, s, t
J123645.51+261803.7	189.19	26.301	0.0305	-77 ± 21	-72^{+18}_{-23}	–	AGN	u, v, –
HARO 11	9.2195	-33.5548	0.020558	26 ± 9	25^{+6}_{-10}	1.41	NO AGN	w, x, x
IRAS F15250+3608	231.7477625	35.977075	0.0552064	90 ± 88	87^{+43}_{-59}	1.05	AGN	DR7
J093813.49+542825.0	144.556	54.4736	0.1021020	7 ± 26	-1^{+24}_{-25}	1.40	NO AGN	DR7
J132734.70+664516.6	201.895	66.7546	0.0303298	-45 ± 30	-46^{+38}_{-21}	0.24	NO AGN	DR7
J170912.73+604950.0	257.303	60.8305	0.0470662	7 ± 13	10^{+12}_{-11}	0.65	NO AGN	DR7
J082354.95+280621.6	125.979	28.106	0.0472225	-12 ± 25	-12^{+16}_{-38}	1.50	NO AGN	DR7
J002101.02+005248	5.25429	0.880033	0.0983929	-2 ± 31	0^{+33}_{-22}	1.61	NO AGN	DR7
J144305.31+611838.6	220.772	61.311	0.0479423	103 ± 29	85^{+26}_{-20}	1.09	NO AGN	DR7
J120016	180.069	27.3331	0.081880	12 ± 30	24^{+27}_{-28}	0.60	NO AGN	DR7
J005527.46-002148.7	13.8645	-0.363486	0.167419	-10 ± 36	-4^{+32}_{-29}	1.72	NO AGN	DR7
J021307	33.2775	0.9368	0.039937	-26 ± 36	-17^{+42}_{-29}	0.36	NO AGN	DR7
J111244.15+550347.1	168.184	55.0631	0.131635	-41 ± 26	-35^{+20}_{-15}	1.32	NO AGN	DR7
J142947.03+064334.9	217.446	6.72638	0.173502	56 ± 28	35^{+25}_{-18}	2.01	NO AGN	DR7
J015028.4+130858.3	27.6184	13.1496	0.1466694	-44 ± 22	-53^{+25}_{-18}	1.27	NO AGN	DR7
J1156+5008	179.128	50.1395	0.235966	37 ± 24	27^{+13}_{-20}	1.59	NO AGN	DR7
J142856.4+165339.4	217.235	16.8943	0.181666	9 ± 34	8^{+36}_{-37}	1.35	NO AGN	DR7
J152521.84+075720.3	231.341	7.95564	0.075791	-33 ± 29	-32^{+25}_{-36}	0.76	NO AGN	DR7
KISSR182	195.607	28.8581	0.0223358	-84 ± 42	-62^{+29}_{-51}	-0.26	NO AGN	DR7
J114422.31+401221.2	176.093	40.2059	0.126947	-5 ± 44	-5^{+38}_{-34}	1.07	NO AGN	DR7

References (a) Saunders et al. (2000); (b) Brightman & Nandra (2011); (c) Rodríguez-Zaurín et al. (2011); (d) Cannon et al. (2004); (e) Leitherer et al. (2013); (f) Hernan-Caballero et al. (2016); (g) Duc et al. (1997); (h) Yano et al. (2016); (i) Wong et al. (2006); (j) Fluetsch et al. (2019); (k) Pustilnik et al. (1999); (l) Wofford et al. (2013); (m) Chisholm et al. (2019); (n) Chisholm et al. (2016); (o) Mutch et al. (2011); (p) Rahmani et al. (2016); (q) Veilleux et al. (2013a); (r) Meyer et al. (2004); (s) Fox et al. (2018); (t) Amblard et al. (2014); (u) Rines et al. (2003); (v) Souchay et al. (2015); (w) James et al. (2013); (x) Chisholm et al. (2018); (y) Sardaneta et al. (2020); (z) Dietrich et al. (2018).

Table 4.2: Continued

Name	R.A. (deg)	Dec. (deg)	z	Best shift ($\mathrm{km\,s^{-1}}$)	Median shift ($\mathrm{km\,s^{-1}}$)	$\log(\mathrm{SFR/M_\odot yr^{-1}})$	Type	Ref.
J115218.74+585657.0	178.078	58.9492	0.0462167	-56 ± 39	-67^{+41}_{-31}	0.77	NO AGN	DR7
J101201.93+603720.3	153.008	60.6223	0.0449798	-52 ± 89	-8^{+56}_{-65}	0.45	NO AGN	DR7
KISSR218	197.317	29.3674	0.020948	-23 ± 67	-21^{+73}_{-35}	0.07	NO AGN	DR7
J133858.25+614957.6	204.743	61.8326	0.0312599	-47 ± 93	-78^{+51}_{-68}	-0.18	NO AGN	DR7
GP1424+4217	216.024	42.2795	0.184816	-12 ± 67	6^{+50}_{-68}	1.71	NO AGN	DR7
J140347.22+062812.1*	210.947	6.47011	0.084420	-118 ± 164	-58^{+204}_{-65}	1.38	NO AGN	DR7
GP0303-0759	45.8392	-7.98979	0.164813	19 ± 58	8^{+50}_{-46}	0.88	NO AGN	DR7
KISSR178*	195.423	29.3812	0.057377	-4 ± 36	0^{+36}_{-28}	0.66	.NO AGN	DR7
GP1137+3524	174.342	35.4074	0.194313	-27 ± 66	-17^{+61}_{-63}	1.64	NO AGN	DR7
KISSR2125	242.585	43.0098	0.0252127	114 ± 67	114^{+66}_{-61}	0.48	NO AGN	DR7
J021348.53+125951.4*	33.4522	12.9976	0.218987	131 ± 80	130^{+41}_{-63}	1.45	NO AGN	DR7
KISSR2021*	236.47	44.2632	0.039943	-262 ± 218	-111^{+132}_{-129}	0.31	NO AGN	DR7
J1547+5119*	236.952	51.3195	0.245340	-27 ± 270	-173^{+178}_{-264}	1.48	NO AGN	DR7
J144827.20+630210.4	222.113	63.0363	0.051090	-198 ± 191	-94^{+103}_{-168}	0.71	NO AGN	DR7
GP1133+6514	173.266	65.2282	0.241412	30 ± 122	28^{+117}_{-138}	0.73	NO AGN	DR7
KISSR1084*	252.272	29.7588	0.032053	-495 ± 254	-581^{+135}_{-277}	0.86	NO AGN	DR7
KISSR40	185.598	29.4438	0.026181	-29 ± 101	-70^{+125}_{-68}	-0.40	NO AGN	DR7
KISSR1942	230.702	43.7735	0.039355	-31 ± 267	-44^{+229}_{-99}	-0.45	NO AGN	DR7
J110151.07+290803.6*	165.463	29.1345	0.071142	193 ± 175	87^{+66}_{-151}	0.73	NO AGN	DR7
IRAS16104+5235	242.917	52.4566	0.0294429	-194 ± 14	-189^{+15}_{-8}	1.01	AGN	y, z, e
KISSR1578	202.184	43.9307	0.0279694	-32 ± 8	-32^{+8}_{-8}	0.33	NO AGN	DR9
J152141.52+075921.7	230.423	7.98937	0.094261	-23 ± 19	-36^{+16}_{-10}	0.98	NO AGN	DR9
J092600.4+442736.1	141.502	44.4602	0.180668	7 ± 18	4^{+23}_{-12}	1.06	NO AGN	DR9
J122612	186.55	4.26002	0.094233	-7 ± 42	11^{+33}_{-29}	0.58	NO AGN	DR9
J102548.47+362258.4	156.452	36.3829	0.126500	-18 ± 26	-16^{+19}_{-24}	0.98	NO AGN	DR9
J131131	197.88	-0.645664	0.081067	-22 ± 26	-16^{+30}_{-26}	0.74	NO AGN	DR9
J141612.96+122340.5	214.054	12.3946	0.123156	-71 ± 34	-68^{+34}_{-28}	1.64	NO AGN	DR9
J132109.07+590605.3	200.289	59.1012	0.0428617	-84 ± 53	-61^{+45}_{-31}	0.60	NO AGN	DR9
J161245.59+081701	243.19	8.28361	0.149143	-55 ± 45	-51^{+41}_{-27}	1.29	NO AGN	DR9
J090704.88+532656.6	136.77	53.4493	0.0298513	-66 ± 63	-46^{+51}_{-45}	0.07	NO AGN	DR9
KISSR108	190.98	29.3696	0.0235760	26 ± 38	29^{+36}_{-25}	-0.56	NO AGN	DR9
J141454.23+054047.6	213.726	5.67989	0.08189	-44 ± 36	-56^{+29}_{-26}	0.38	NO AGN	DR9
J111323.99+293039.2	168.35	29.5109	0.175143	-48 ± 37	-38^{+33}_{-21}	0.55	NO AGN	DR9
J115241.69+661827.2*	178.174	66.3072	0.0459663	-610 ± 335	-650^{+69}_{-572}	0.42	NO AGN	DR9
GP0911+1831	137.806	18.5189	0.262173	-33 ± 38	-30^{+48}_{-31}	1.70	NO AGN	DR9
J152053.59+571122.1	230.224	57.1897	0.029470	-66 ± 68	-33^{+61}_{-47}	-0.48	NO AGN	DR9
KISSR298*	202.457	29.5797	0.0489774	-309 ± 321	-423^{+180}_{-360}	0.33	NO AGN	DR9
GP1032+2717	158.112	27.2987	0.192490	88 ± 322	88^{+122}_{-107}	1.24	NO AGN	DR9
GP1249+1234	192.144	12.5675	0.263408	-50 ± 78	-18^{+71}_{-48}	1.00	NO AGN	DR9
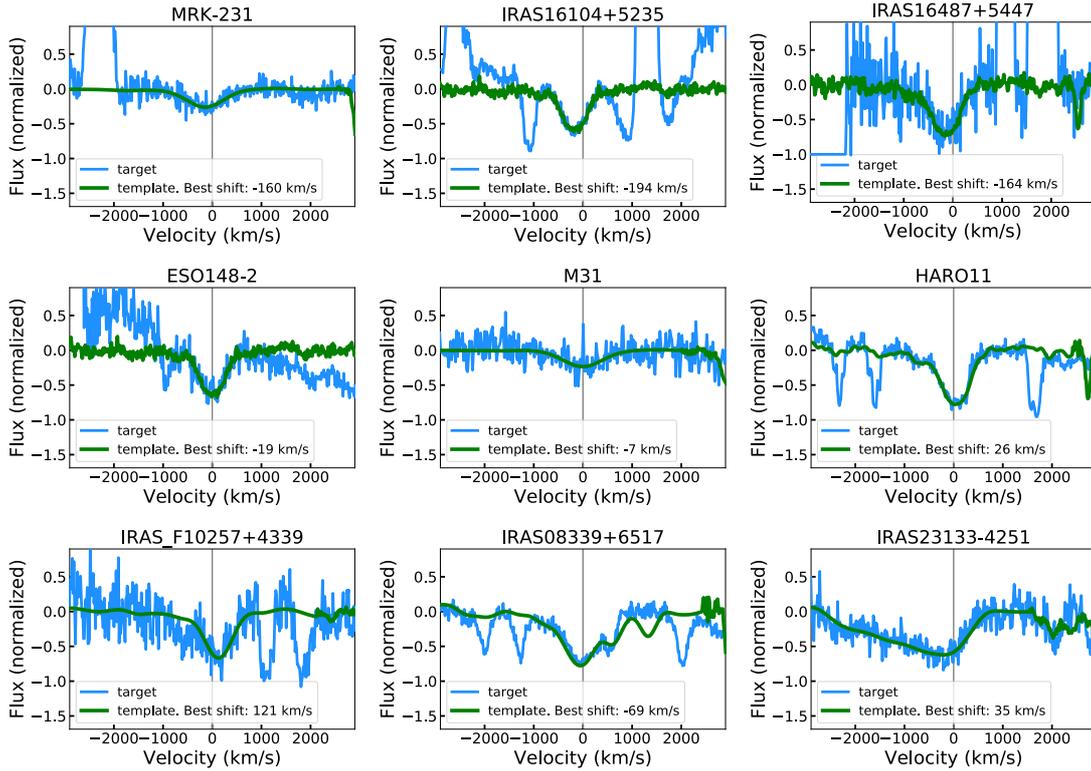
Figure 4.1: C III absorption line in some galaxies of our sample (HST/COS data). We report in the legend the C III velocity ("best shift" in Table 4.1; see also Sect. 4.2.2) estimated using the cross-correlation between the galaxies spectra and a library of templates. The galaxy line is shown in blue while the green line marks the "best" template, evaluated using the χ^2 statistics (see Sect. 4.2.2). The grey vertical line sets the systemic velocity of the galaxy. We see that several galaxies show blueshifted C III absorption, which could suggest the presence of young stars in the outflow. All the spectra are shown in Fig. 4.7 at the end of this Chapter.

velocity structure in the stellar atmosphere that would have been necessary in case we had estimated the C III velocity with a line fit (e.g. a Gaussian fit).

We used the COS spectra of nine nearby star-forming galaxies studied by James et al. (2014). These are very high signal-to-noise spectra where the C III line is clearly detected and span a broad range of metallicities and galaxy types. More importantly, the spectra of James et al. (2014) belong to low mass galaxies and HII regions in which it is very unlikely that star formation is occurring in the outflow. The data were obtained using the G130M grating, thus these spectra are perfectly consistent in terms of spectral resolution with the galaxies of our sample.

We used the C III velocity estimated by James et al. (2014) to set the systemic velocity of the templates, so that the C III line is not affected by any velocity shift. This is a crucial step, as these lines constitute the zero point velocity reference when we measure the C III velocities of our sample. We excluded from the James et al. (2014) sample the spectrum of SBS 0335–052, as it is contaminated from the Milky Way absorption (see Fig. 2 of James et al. 2014), thus we used eight spectra to build our library.

Then, in order to simulate a wide range of line widths, we smoothed each template with a Gaussian kernel with a full-width at half-maximum (FWHM) ranging from 100 to 1000 $\mathrm{km\,s^{-1}}$ at steps of 50 $\mathrm{km\,s^{-1}}$. We also diluted the C III line flux of the galaxies of James et al. (2014) from the 10 to 90% in steps of 0.1, in order to reproduce a broad span of continuum levels, associated with the potential contribution of an AGN that might dilute the stellar feature. In this way, we ended up with a library of 232 templates reproducing a wide variety of C III line absorptions.

Step 2: Normalization, rebinning, conversion from wavelength to velocity

Before performing the cross-correlation (see step 3), we normalized the templates for the continuum level and subtracted one, so that the continuum emission is set to zero. This step has been applied so that in the cross-correlation only the contribution of the C III line is taken into account, while the continuum in the proximity of the line results in a null contribution. The continuum level was estimated in close proximity of the C III line using a linear fit. Then, we rebinned the native COS spectra by six elements, so that each spectral bin spans over ~ 20 $\mathrm{km\,s^{-1}}$, corresponding to about the instrumental resolution. To convert the wavelengths to velocities we used a C III rest-frame wavelegth of 1175.53 Å, in consistency with James et al. (2014). We checked that with this value the cross-correlation (next step) gives zero velocity for the templates.

The same procedure has been applied to the spectra of the 70 galaxies in our sample.

Step 3: Cross-correlation

We cross-correlated each spectrum of the galaxies in the sample with the 232 templates, according to the relation

$$C(v) = \Sigma_n f_g(n + v) * f_t(n) \tag{4.1}$$

where $C(v)$ is the cross-correlation function, v is the lag (i.e., the velocity displacement), $f_g(n)$ and $f_t(n)$ are the flux value of the galaxy and the template in the n-th element of the two spectra. The cross-correlation was performed locally, that is, not over the entire spectrum but at the location of the C III line, as we are interested in the analysis of this spectral feature only. We thus limited the velocity range in which

we cross-correlated the spectra typically between –1000 and +1000 $\mathrm{km\,s^{-1}}$ around the C III absorption of the galaxy and the template.

For each template, we calculated the cross-correlation as a function of the velocity displacement. The C III velocity is defined as the value of the velocity displacement where the cross-correlation function peaks. We estimated this velocity by fitting a Gaussian function to the cross-correlation sampling, as its shape is likely Gaussian.

We obtained in this way 232 values of the C III velocity (i.e., one for each tempate). To choose the "best" C III velocity measurement, we shifted the galaxy spectrum according to each of the 232 values and calculated the χ^2 between the galaxy spectrum and the corresponding template. We considered as the best C III velocity the velocity shift corresponding to the least χ^2. This provides what we call "best shift" in the following analysis.

Step 4: Bootstrap

In order to calculate the uncertainties affecting the C III velocity measurement we performed a bootstrap analysis. For each galaxy spectrum we simulated fifty spectra where, for each spectral element, we substitued the observed flux with a value extracted from a Gaussian distribution centered to the observed flux and with a standard deviation equal to the noise of that spectral element. We thus repeated step (3) of this procedure for all fifty spectra. In this way, we obtained a distribution of C III velocities for each galaxy in the sample (see Fig. 4.8 at the end of this Chapter). We considered the median of the distribution as the final measurement of the C III velocity ("median shift" in Table 4.1). The uncertainties on the median were evaluated as the velocity values corresponding to the 16th and 84th percentiles of the distribution. In this step we evaluated also the error associated to the "best shift" defined in step (3). We calculated it as the standard deviation of the velocity distribution assuming the best shift as the average value.

On average, we did not find significant difference between the best shift and the median shift for the galaxies in the sample. In the rest of the discussion we consider the median shift as the C III velocity for all the galaxies. All the considerations are still valid if we use the best shift rather than the median one.

4.3   Results

We report in Table 4.1 the C III velocities that we obtained applying the method described in Sect. 4.2.2. Several galaxies present blueshifted C III absorption (see Fig. 4.1 and Fig. 4.7). This fact could suggest the presence of stars inside galactic outflows. As for other absorption and emission lines at UV-optical wavelegths in the case of galactic outflows, we detect the blueshifted absorption (corresponding to the approaching side of the outflow) because the redshifted one, produced by the receding side, is absorbed by dust in the galactic disc.

The most remarkable cases are NGC 6090 (= IRAS 16104+5235) and Mrk 231. These objects are well known starburst galaxies, which host a powerful AGN in case of Mrk 231. We see indeed that the C III line is blueshifted of $-189^{+15}_{-8}\,\mathrm{km\,s^{-1}}$ and $-163^{+24}_{-42}\,\mathrm{km\,s^{-1}}$ for these two sources, respectively. The high-velocity stars could be
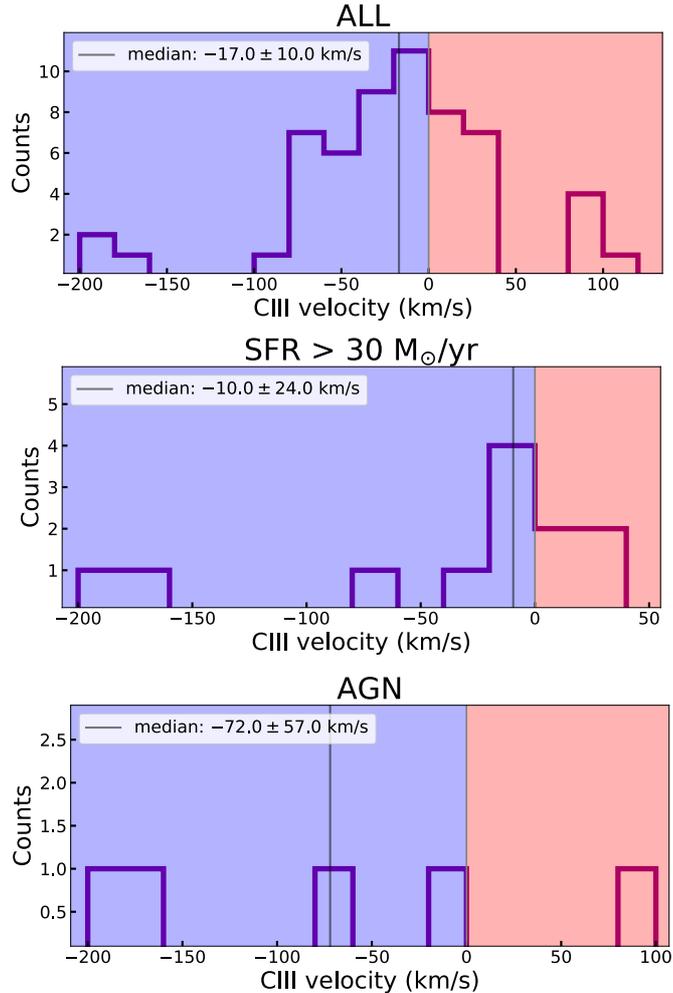
Figure 4.2: Distribution of the C III velocities for the galaxies in the sample. We removed the sources presenting a broad C III profile as the C III velocity measurement could be difficult for these objects. We see that the distribution is asymmetric and skewed to the blue (top panel), suggesting that several galaxies present young stars possibly in outflow. The asymmetry is emphasized when considering the sources with SFR > 30 $M_\odot yr^{-1}$ (middle panel) and the galaxies hosting an AGN (bottom panel). This fact highlights a possible correlation between SFR, AGN activity and the presence of outflowing stars.

produced in starburst and AGN-driven outflows. We further discuss these two sources in Sect. 4.3.4, as they present clear signs of multi-phase outflowing gas from other tracers.

On the other hand, there are objects that do not show any evidence of shifted C III absorption, which is consistent with the rest-frame velocity of the galaxy. This is expectable in "normal" star-forming galaxies as, for example, M31, which does not show evidence of intense star formation or AGN activity.

Finally, there are galaxies showing redshifted C III absorption. The redshifted absorption could be indicative of inflowing stars. An interesting case (IRAS F15250+3608) of redshifted C III absorption is discussed in Sect. 4.3.4.

4.3.1 C III velocity distribution

We now discuss with more detail the distribution of the C III velocities. Before doing this, we removed from the sample 10 sources, which show a very broad C III profile and asymmetric towards the blue (see an example in Fig. 4.1 for IRAS 23133–4251). A broad C III profile could be associated to outflowing stars, high-metallicity, or stellar winds (Pellerin et al. 2002). Thus, the C III velocity of these sources results particularly complex to interpret and could be blueshifted for effects not related to young stars formed in the outflow. For this reason we do not consider these objects in the following discussion, which is related to the statistical properties of the sample, as they could artificially make the distribution of the C III velocities bluer. We removed also three additional sources for which the C III line is contaminated by other features (i.e., possible absorption from the Milky Way and high-velocity clouds on the line of sight). Therefore, the final sample discussed hereafter includes 57 objects. The analysis including the rejected sources is presented in Fig. 4.5. None of the results is considerably modified after their inclusion. We will return on some of the rejected sources when discussing some interesting objects individually (see Sect. 4.3.4).

We see that the distribution of the C III velocities is clearly asymmetric (Fig. 4.2, top panel). The median value is -17 ± 10 km s^{-1} and the distribution, rather than being Gaussian, is skewed to the blue, with velocities as high as -200 km s^{-1}. The uncertainty on the median was evaluated as the ratio between the standard deviation of the distribution and the square root of the number of objects in the sample (i.e., the uncertainty on the average) multiplied by 1.25. This is a good approximation in case the distribution of values is quite Gaussian (Brightwell & Dransfield 2013).

We assessed the significance of the observed blueshifted velocity distribution by performing a *Kolmogorov-Smirnov test*. This test allows to quantify the difference between the distribution function of the data and the cumulative distribution function of a reference distribution. Under the so-called "null hypothesis" this difference is zero, that is, the data sample is statistically indistinguishable from the reference distribution. The probability that the data sample follows the reference distribution is quantified by a "p-value", which varies between 0 and 1. In our case, we built the reference distribution by extracting 57 random velocity values (i.e., the same number of the observed ones) from a Gaussian distribution centered in zero and with the same standard deviation of the data, that is, a velocity distribution that one would expect in case of simple fluctuactions due to different stellar populations (see some examples in Fig. 4.3). Then, we compared the observed velocity distribution to the simulated one with the Kolmogorov-Smirnov test and retained the associated p-value. We iterated this procedure for one hundred times and built a distribution of the p-values (Fig. 4.4). We considered the median of the distribution as the final probability value. We see that this value amounts to $\lesssim 10\%$, which means that the observed C III velocity distribution is offset from a Gaussian distribution centered in zero at the $\gtrsim 90\%$ of confidence level.

Overall, the high fraction of objects presenting blueshifted C III emission suggests that the formation of stars inside galactic outflows could be a quite common process in galaxies.
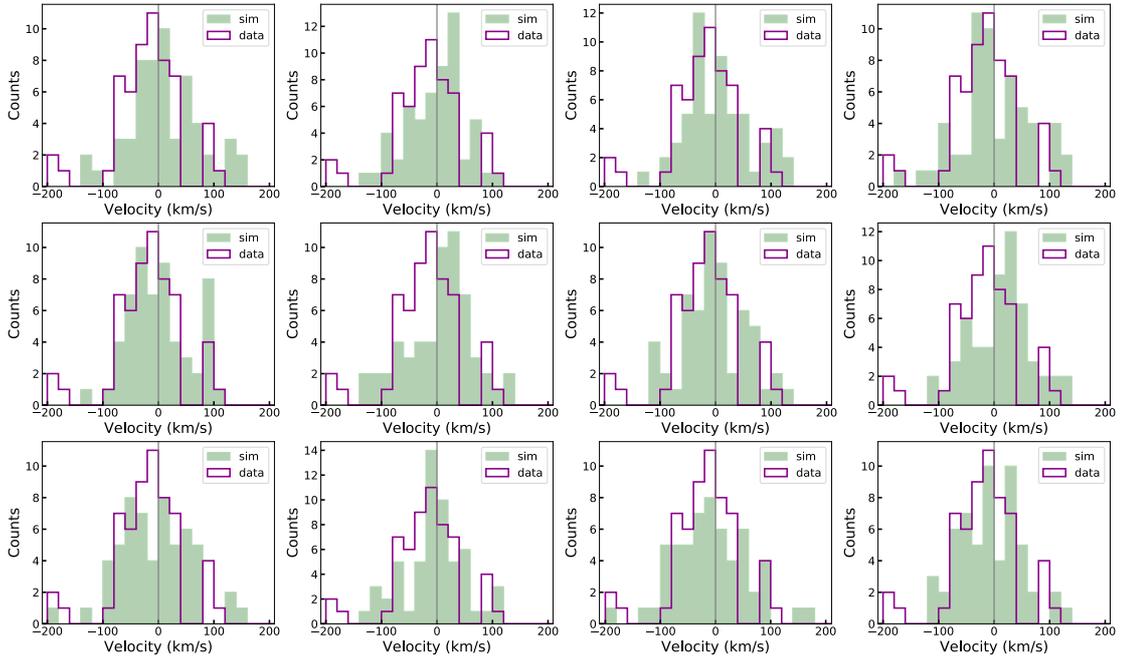
Figure 4.3: Comparison between the observed C III velocity distribution (purple) and simulated Gaussian velocity distributions (green) centered on zero with a standard deviation equal to the observed one. We simulated one hundred Gaussian distributions and performed a Kolmogorov-Smirnov test to assess if the observed distribution is significantly different from the simulated ones.
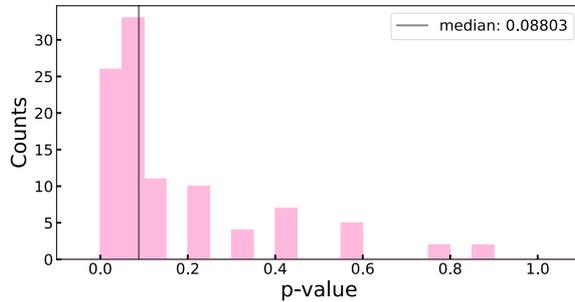
Figure 4.4: Distribution of the p-values resulting from the Kolmogorov-Smirnov test. The median of the distribution amounts to $\lesssim 10\%$, which means that the deviation of the observed C III velocity distribution from a non–shifted Gaussian is significant at the $\sim 90\%$ of confidence level.
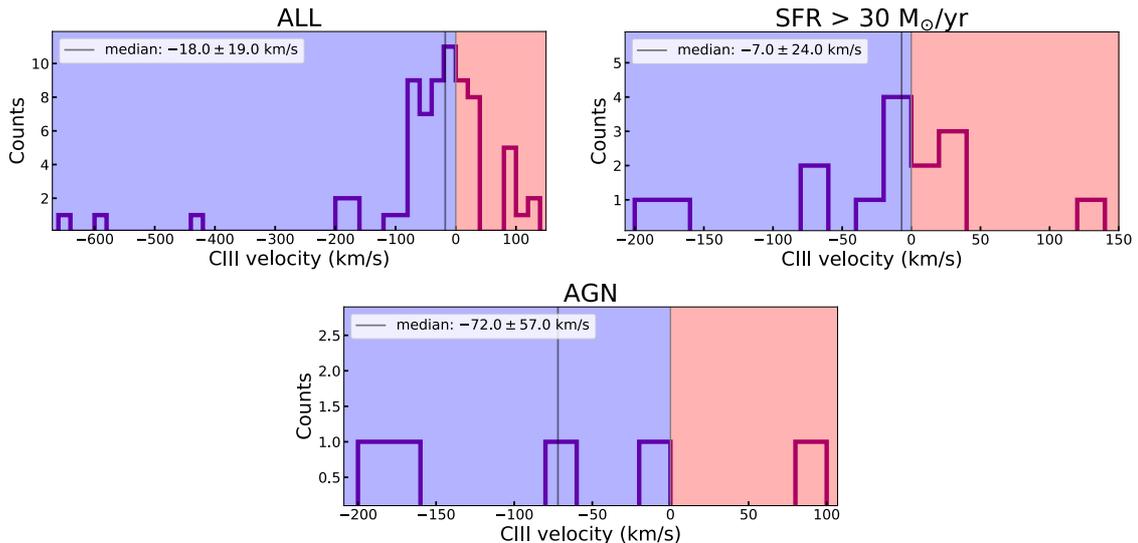
Figure 4.5: Distribution of the C III velocities of the galaxies in the sample. We included here also the sources presenting a broad C III profile. The distribution is asymmetric and skewed to the blue, suggesting that several galaxies present young stars possibly in outflow. None of the consideration reported in Sect. 4.3 is significantly modified by the inclusion of these sources.

4.3.2 Correlation with SFR and AGN activity

We now discuss the distribution of the C III velocities that we obtain by considering only the galaxies with a SFR higher than 30 $M_\odot \mathrm{yr}^{-1}$. This SFR cutoff has been chosen as a compromise to have still several sources in the new distribution and highlight any possible correlation between C III velocities and SFR. We see that the distribution (Fig. 4.2, middle panel) results more asymmetric compared to the total one, with 8 out of 12 objects having blueshifted C III absorption. The median C III velocity is -10 ± 24 km s^{-1}. The high fraction of objects with blueshifted velocities suggests a possible relation between SFR and blueshifted C III absorption. A similar correlation has been seen also by Gallagher et al. (2019). The physical reason underlying this correlation could be that more star-forming galaxies produce more powerful outfows and hence more outflowing stars. Studies of larger samples will be useful to assess this trend more firmly.

Finally, we examine the distribution of the five AGN in our sample. We see that in this case, four out of five sources present blueshifted C III absorption, with a median C III velocity of -72 ± 57 km s^{-1}. This fact suggests that the presence of C III blueshifted absorpion could be strongly related to the AGN activity of a galaxy. Unfortunately, the low number of AGN in our sample does not make this result statistically very solid, requiring additional observations.

4.3.3 Correlation with the outflow rate

We then investigated a possible correlation between the gas outflow rate (i.e., the mass of outflowing material per year) of the galaxies in the sample and the C III velocities. Unfortunately, most galaxies in the sample do not have a direct measurement of the outflow rate. Therefore, we estimated both the molecular and total outflow rate of the galaxies by using Eq (5) and Eq (6) of Fluetsch et al. (2019). These equations allow
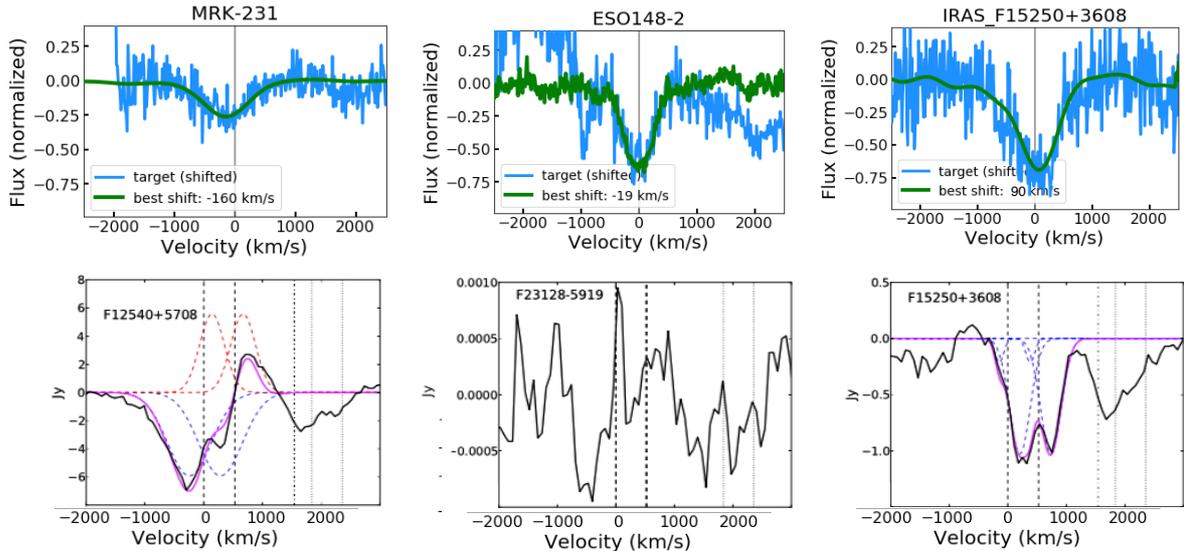
Figure 4.6: Comparison between the C III absorption line and the OH 119μm absorption in Mrk 231, ESO 148-2 and IRAS F15250+3608, observed also by Veilleux et al. (2013a). Interestingly, we see that the two lines show a similar motion, as blueshifted/non-shifted/redshifted C III absorption corresponds to blueshifted/non-shifted/redshifted OH line. This fact suggests a possible relation between molecular outflows and young stars. The bottom plots are from Veilleux et al. (2013a).

to estimate the rate of expelled gas based on the SFR, the stellar mass and the AGN luminosity of a galaxy. We set the AGN luminosity to zero for the objects without an AGN (see Table 4.1). For the AGN in the sample we collected this information from the literature (Nardini et al. 2009; Fluetsch et al. 2019). The stellar masses and SFR that go in the equations were taken from the SDSS DR7 and DR9 for most of the sources (see Sect. 4.2.1). For the remaining ones we found these properties from the literature. However, we did not find any significan relation between C III velocities and outflow rate, suggesting that the formation of stars in the outflow does not simply depend on the outflow rate but also on other physical properties of outflows (e.g., amount of dense gas).

4.3.4   Comparison with outflows traced by ISM lines

We now discuss the C III absorption line with regard to multi-phase outflows detected in the galaxies of our sample from other works in the literature. We start from the work of Veilleux et al. (2013a), who studied molecular outflows in a sample of 43 nearby galaxies using the OH 119μm line. Three objects in our sample (Mrk 231, ESO 148–2 and IRAS F15250+3608) have been studied also in this thesis. Interestingly, we find that for three out of three sources the C III absorption shows a similar motion compared to the OH line (Fig. 4.6). We see indeed that Mrk 231 presents C III absorption that is strongly blueshifted ($v_{\mathrm{C\ III}} = -163^{+24}_{-42}$ km s^{-1}) and shows at the same time blueshifted OH absorption with a median velocity of $v_{\mathrm{OH}} = -237$ km s^{-1}(see Table 2 of Veilleux et al. 2013a). On the other hand, ESO 148–2 shows only a slightly blueshifted C III absorption line ($v_{\mathrm{C\ III}} = -7^{+36}_{-26}$ km s^{-1}) consistent with no blueshift at all, while no outflow was detected using the OH line. Finally, IRAS F15250+3608 presents both redshifted C III ($v_{\mathrm{C\ III}} = 87^{+43}_{-59}$ km s^{-1}) and OH absorption ($v_{\mathrm{OH}} = +189$ km s^{-1}),

suggesting that both gas and stars are in inflow, as they respond to the gravitational potential of the galaxy. This fact could highlight an interesting correlation between molecular outflows and the presence of young stars with similar motion, possibly associated to them. Many theories predict indeed that molecular outflows could be regions where star formation could take place because of the high density and low temperature of the outflowing gas (Zubovas et al. 2013a; Nayakshin & Zubovas 2012).

Then we consider the work of Fluetsch et al. (2019), which studied molecular outflows in 45 star-forming galaxies and AGN hosts at low redshift by analyzing the CO emission profiles. Two galaxies in our sample (Mrk 231 and IRAS F10257+4339) were studied also by Fluetsch et al. (2019). Both sources show evidence of cold outflows with velocities of 700 and 350 $km\,s^{-1}$ respectively. As discussed before, we found in Mrk 231 evidence of blueshifted C III absorption with $v_{C\ III} = -163^{+24}_{-42}$ $km\,s^{-1}$; on the other hand, we detected in IRAS F10257+4339 C III absorption redshifted of $v_{C\ III} = 130^{+22}_{-21}$ $km\,s^{-1}$. However, the C III profile of this source presents a blueshifted feature that makes the C III velocity value and its interpretation quite uncertain (see Fig. 4.1).

We now discuss the C III velocities by comparing them with ionized outflows detected at the UV-wavelengths. We consider the work by Leitherer et al. (2013), which analyzed the UV-spectra of four infrared-luminous star-forming galaxies. The authors inferred the presence of outflowing gas by studying ISM low-ionization absorption lines like Si III $\lambda1206$, Si II $\lambda1260$ and C II $\lambda1334$. They found that these lines are blueshifted with velocities ~ -400 $km\,s^{-1}$ for all the objects in their sample, i.e. NGC6090, NGC3256 (= IRAS F10257–4339), IRAS08339+6517 and IRAS23133–4251 galaxies. We found clear blueshifted C III absorption in two of these sources (NGC6090 and IRAS08339+6517) with velocities of -189^{+15}_{-8} $km\,s^{-1}$ and -69^{+6}_{-10} $km\,s^{-1}$ respectively. On the other hand we found redshifted C III absorption in NGC3256 and IRAS23133–4251. However, the latter two sources and IRAS08339+6517 were excluded from the final sample because they show a broad C III profile or blueshifted features in the line profile which make the C III velocity measurement difficult.

4.4   Future prospects

From the analysis presented above, we see that several galaxies present blueshifted C III absorption, possibly due to young stars formed inside galactic outflows. For some objects, the latter have been detected by other works using ISM lines. The presence of blueshifted C III absorption seems to be related to the SFR and the AGN activity of the galaxies. This fact suggests that positive feedback could be a quite common process in galaxies, as already suggested by Gallagher et al. (2019) and Rodríguez del Pino et al. (2019). This feedback mode could have important implications on the assembly of the spheroidal component of galaxies and on other processes, as reported in Chapter 1 (see also Gallagher et al. 2019).

The next steps of the analysis presented in this Chapter will be to further verify the reliability of our C III velocity measurements by constraining the redshifts of the galaxies in the DR7 and DR9 databases using solely optical stellar lines or low ionization nebular lines (unaffected by outflows). In this way it will be possible to exclude any contamination due to non-circular gas motion on the redshift measurement, typically dominated by Hα and [O III] $\lambda5007$ in many of these galaxies. We will also extend our library of reference spectra by including synthetic models of different stellar popula-

tions, in order to exclude any bias on the C III velocity measurement due to the COS spectra of star-forming galaxies that we used in our library of templates.

Finally, we would like to deepen the study of the objects that are particularly intriguing for the high C III blueshifted velocity, such as NGC 6090 and Mrk 231. The latter would be particulary useful to study as this galaxy represents the archetipal quasar at low-z and its outflow has been intensively studied by several works using multiwavelength tracers (e.g., Feruglio et al. 2010; Fischer et al. 2010; Rupke & Veilleux 2011; Veilleux et al. 2013b; Morganti et al. 2016; Cicone et al. 2020).
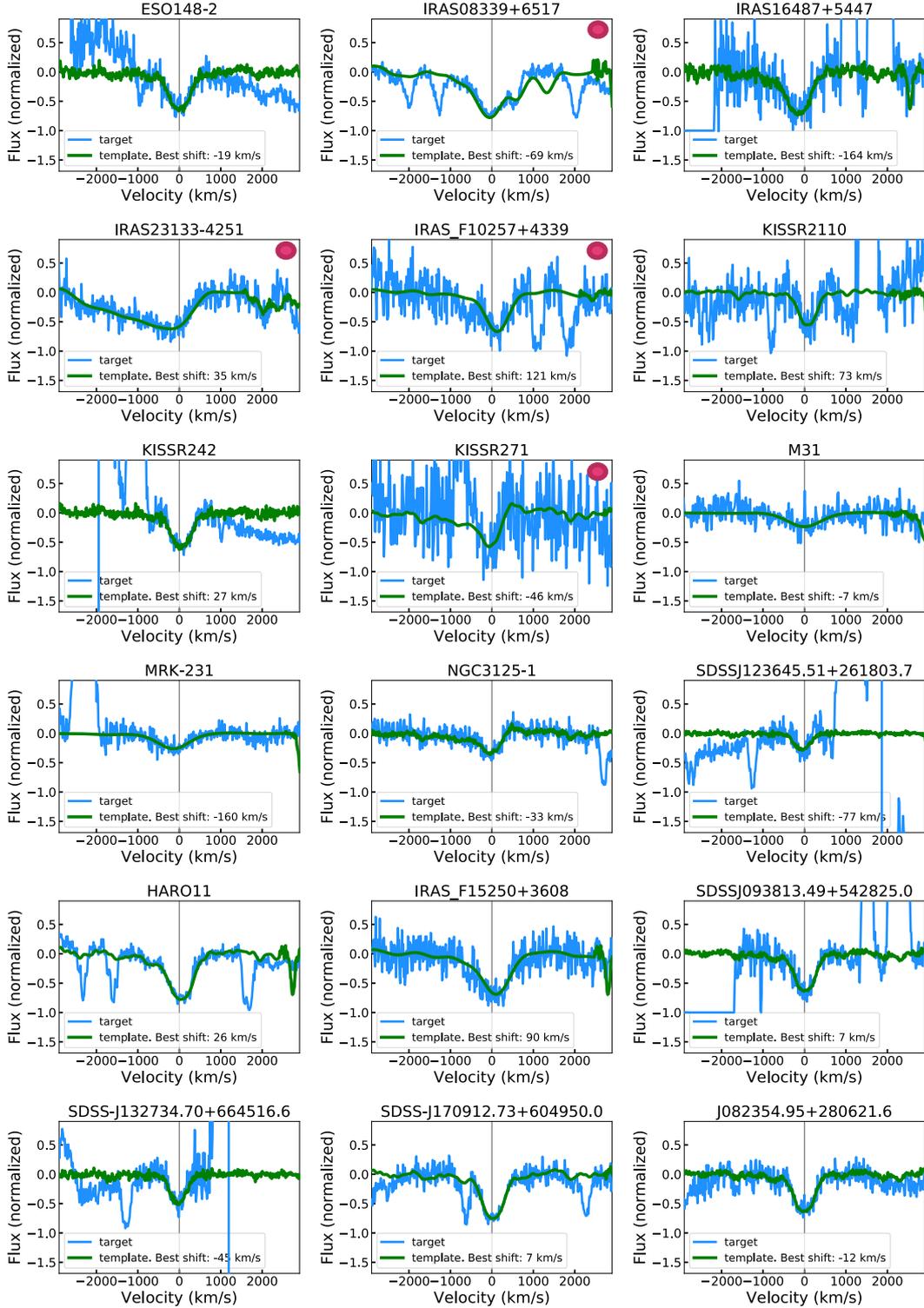
Figure 4.7: C III absorption line in the galaxies of our sample (HST/COS data). We report in the legend the C III velocity ("best shift" in Table 4.1; see also Sect. 4.2.2) estimated using the cross–correlation between the galaxies spectra and a library of templates. The galaxy line is shown in blue while the green line marks the "best" template, evaluated using the χ^2 statistics (see Sect. 4.2.2). The grey vertical line sets the systemic velocity of the galaxy. We see that several galaxies show blueshifted C III absorption, which could suggest the presence of young stars in the outflow. We marked with a magenta circle the sources with a broad C III profile that we excluded from the statistical analysis (see Table 4.1 and Sect. 4.3).
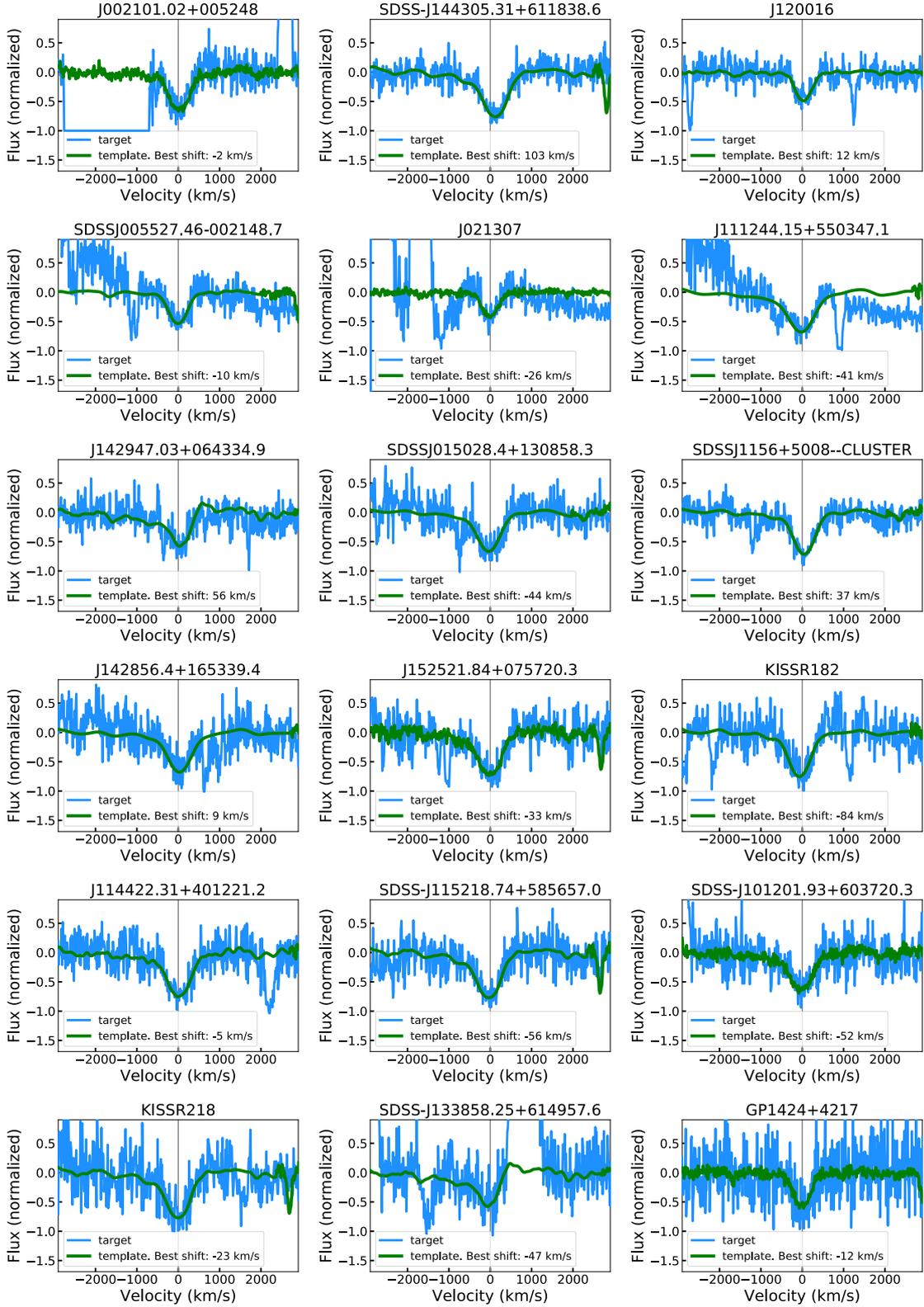
Figure 4.7: (continued) C III absorption line in the galaxies of our sample (HST/COS data).
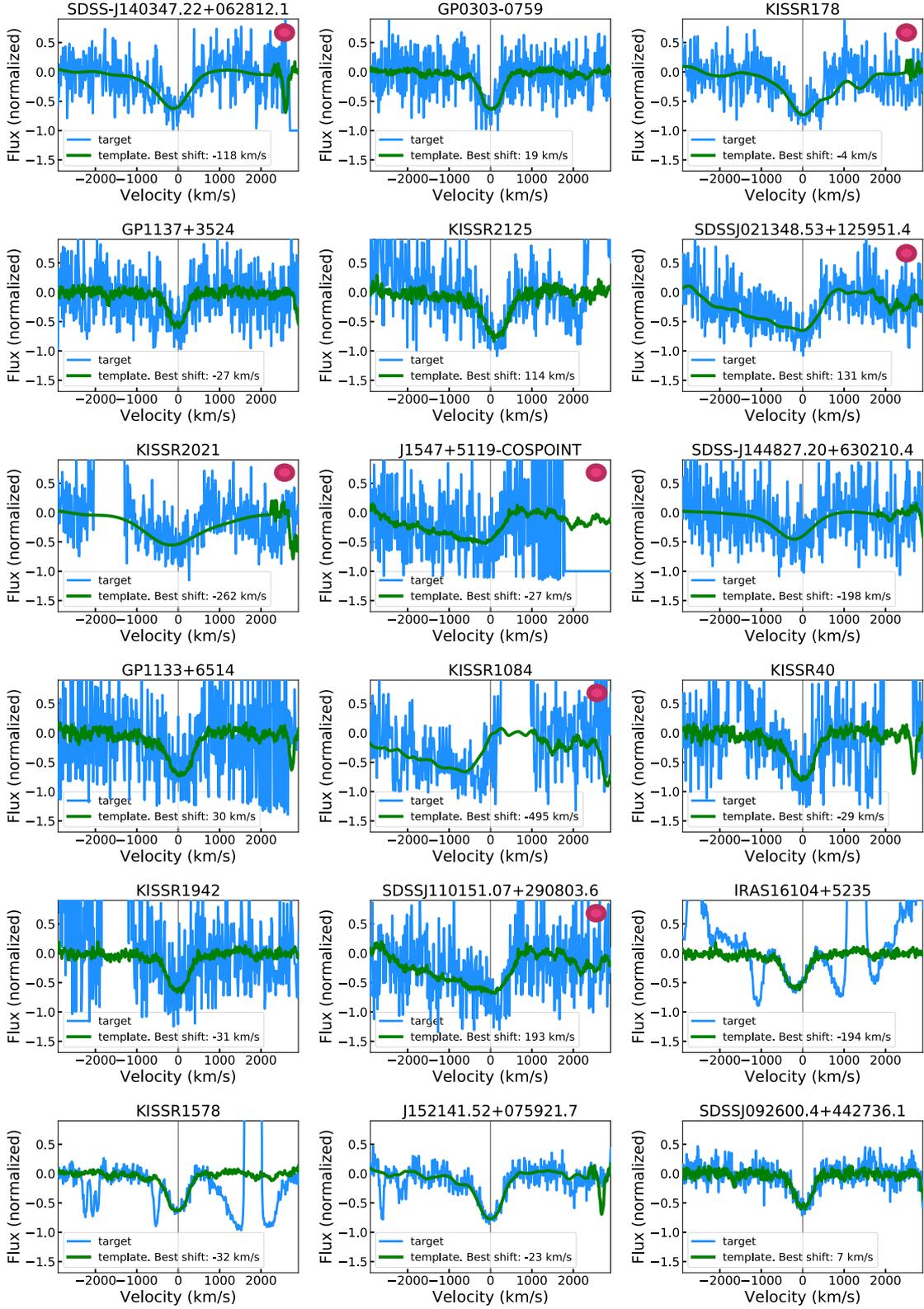
Figure 4.7: (continued) C III absorption line in the galaxies of our sample (HST/COS data).
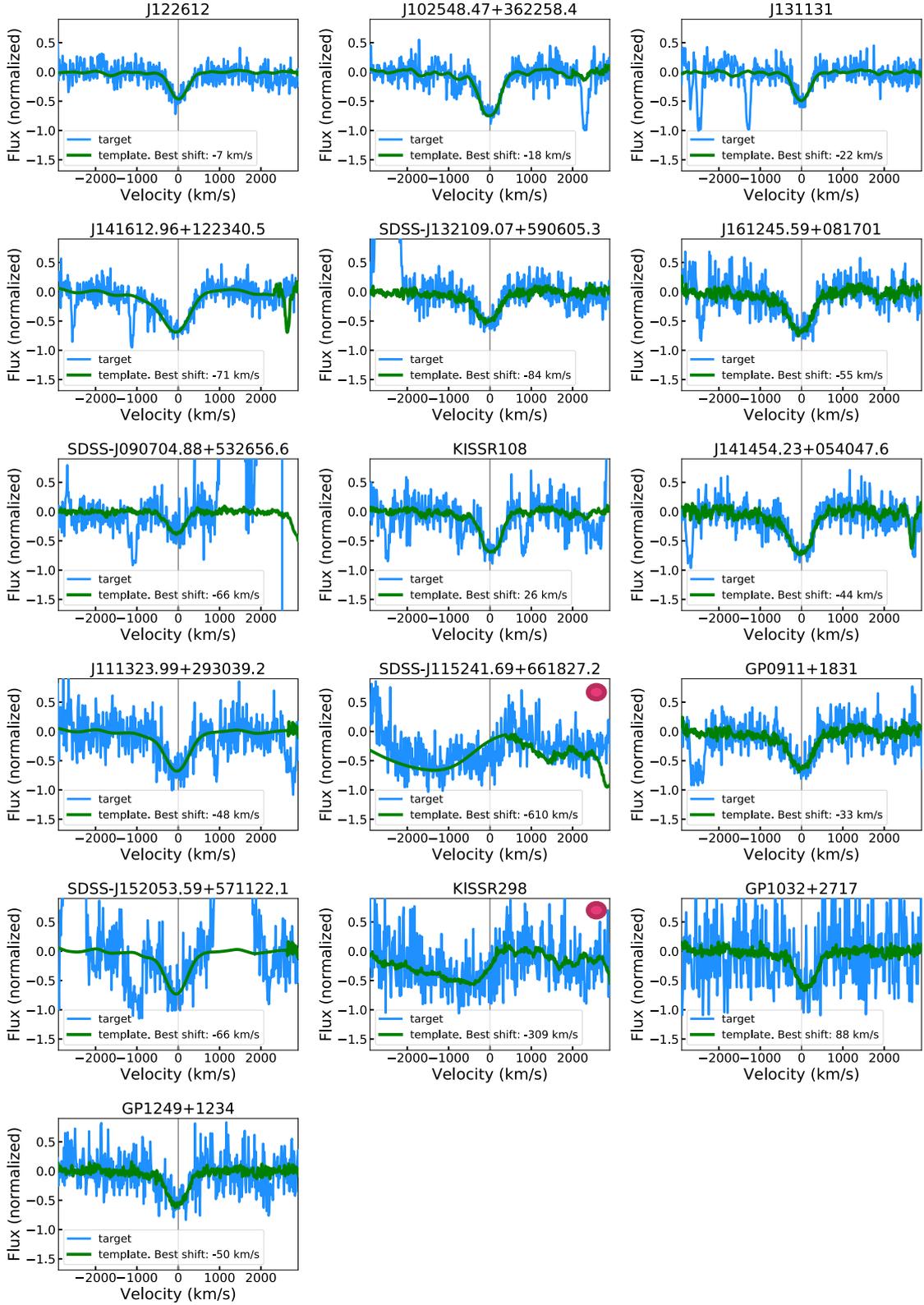
Figure 4.7: (continued) C III absorption line in the galaxies of our sample (HST/COS data).
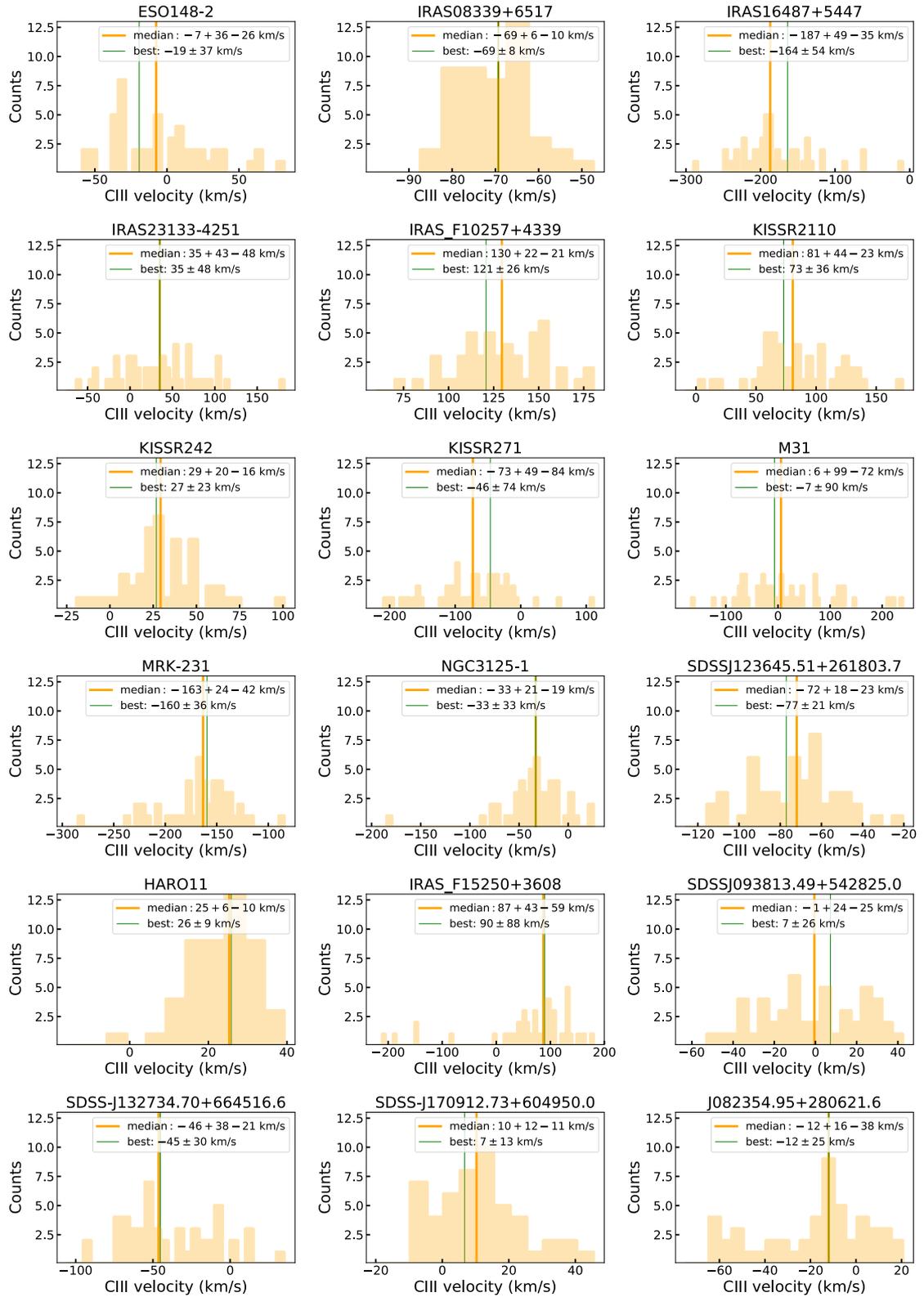
Figure 4.8: Distribution of the C III velocity in the galaxies of our sample calculated via a bootstrap analysis.
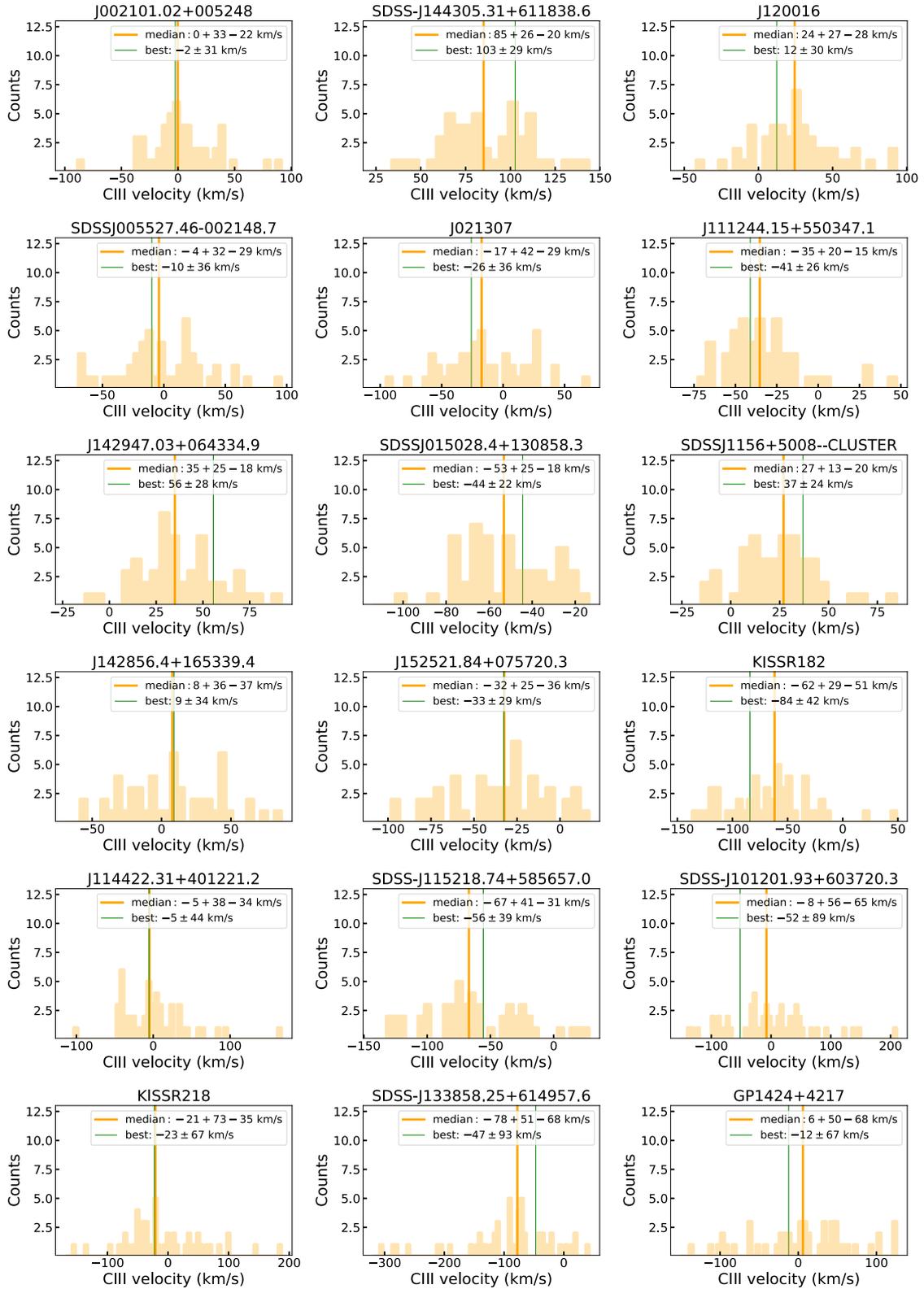
Figure 4.8: (continued) Distribution of the C III velocity in the galaxies of our sample (HST/COS data).
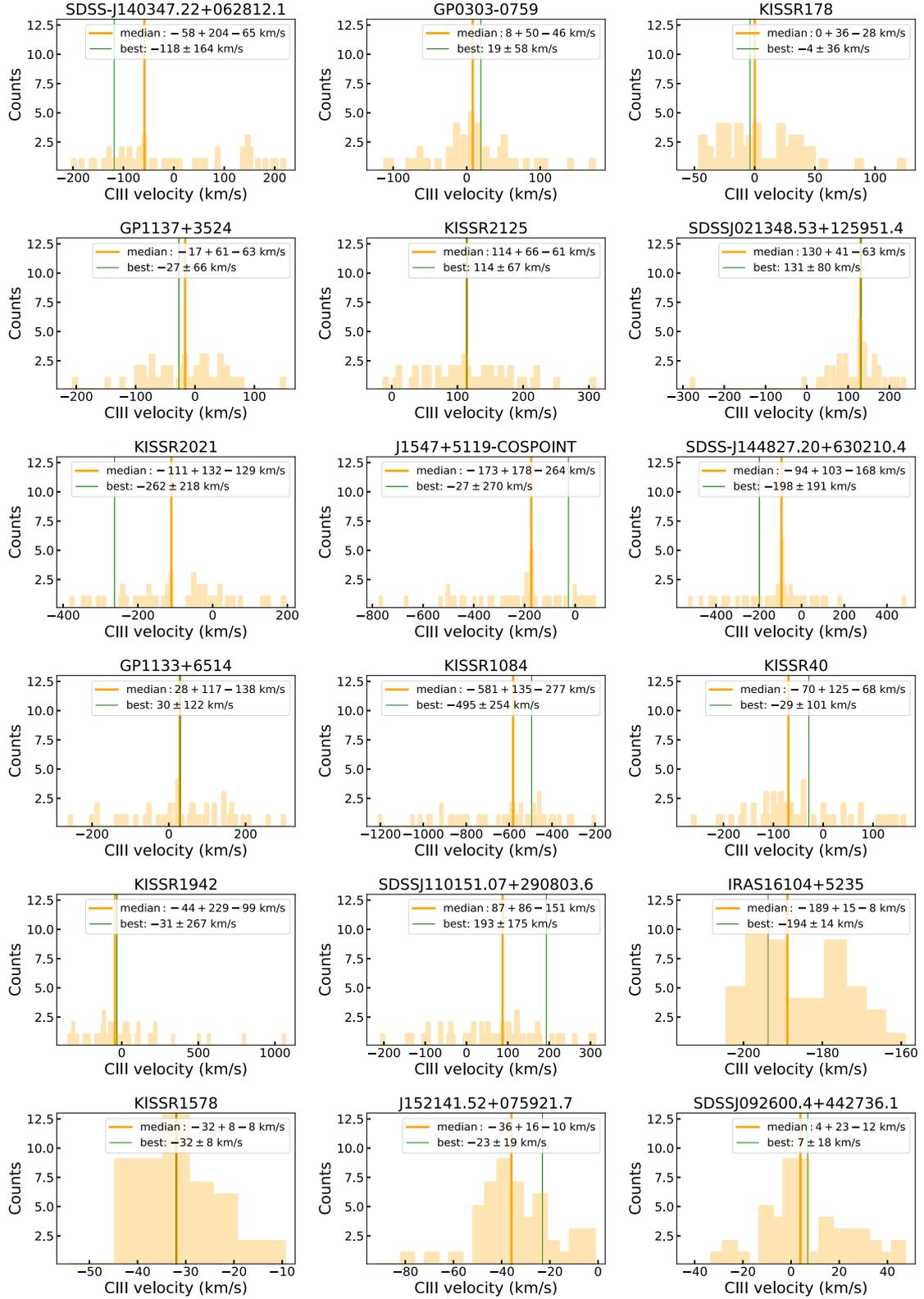
Figure 4.8: (continued) Distribution of the C III velocity in the galaxies of our sample (HST/COS data).
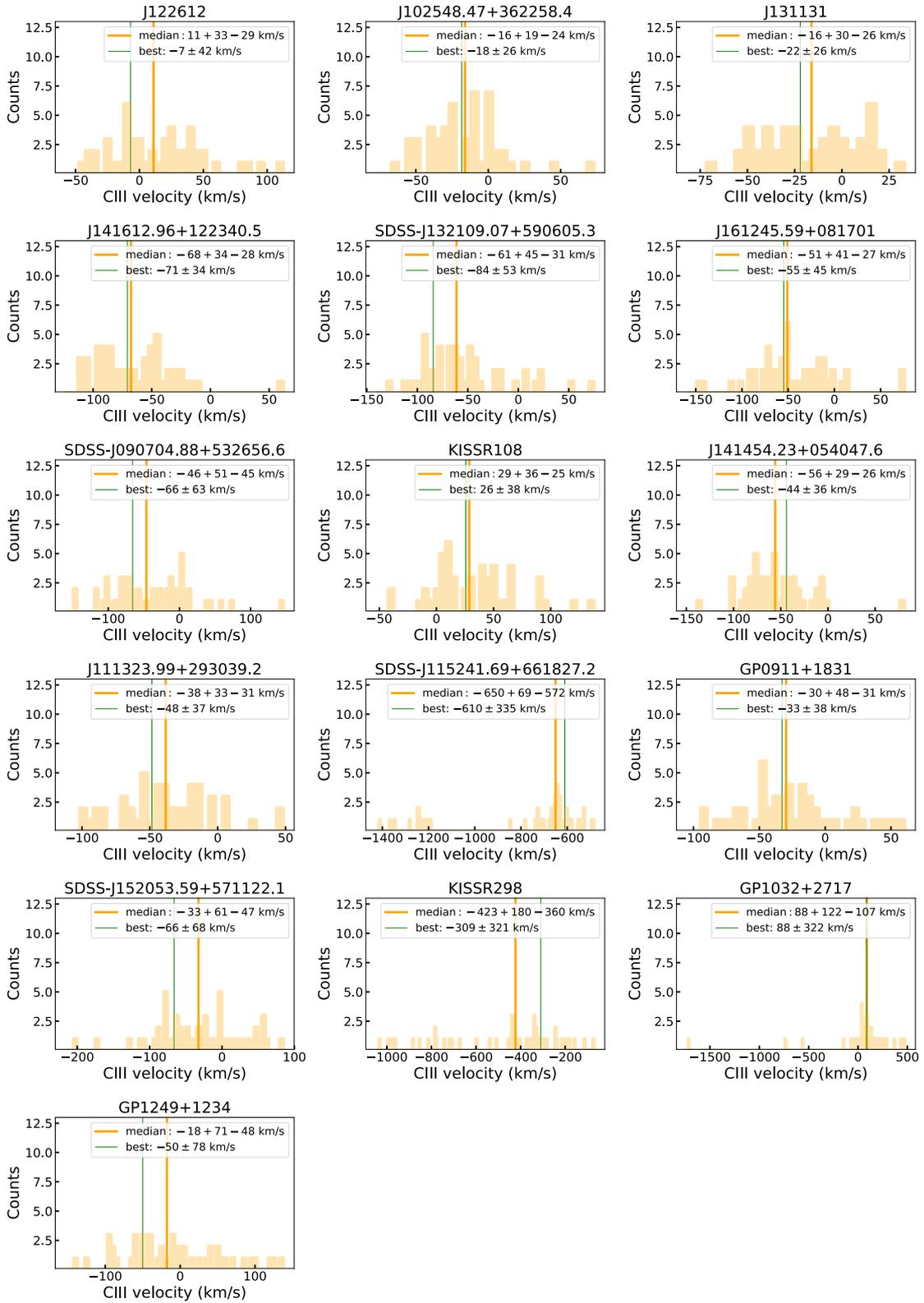
Figure 4.8: (continued) Distribution of the C III velocity in the galaxies of our sample (HST/COS data).

Chapter 5

Conclusions and future prospects

Studying the mechanisms that regulate star formation is a complex matter. The cosmic star formation history strongly varies as a function of time but what drives this variation is poorly known. A proper census of the cosmic SFRD requires multiwavelength selections of galaxies at all epochs. In particular, IR and mm-selections of galaxies are sensitive to dusty objects and to the emission of cold gas (i.e., the fuel from which stars form). These selections are thus a powerful tool if we want to provide a measurement of the total amount of star formation in the Universe, unbiased by dust extinction.

In addition, models predictions show that AGN could exert a major role in regulating the star formation activity of galaxies. According to models, they could be pivotal in quenching star formation in massive galaxies through gas ejections and heating. On the other hand, AGN could be also responsible for star formation episodes in the host galaxy. Detailed observational studies of AGN-driven outflows are crucial to assess the role that AGN have in shaping their hosts.

In this thesis, we investigated the processes that fuel and quench star formation across cosmic time. On one side, we focused on the study of cold gas via a statistical approach and we derived an estimate of the cosmic SFRD in the early Universe by using the [C II] 158μm line, that is, a tracer not affected by dust obscuration. On the other side, we explored the effectiveness of AGN feedback in both suppressing and triggering star formation in the host galaxies.

We summarize here the main results of this thesis:

1) [C II] luminosity function and cosmic SFRD at $z \sim 5$

We studied the [C II] 158μm LF at $z \sim 5$ by using the lines serendipitously discovered in the ALPINE survey. This is the first [C II] LF based on galaxies purely selected due to their [C II] emission. First, we performed a blind search over the 118 ALPINE pointings, which revealed several lines. We assessed the fidelity and completeness of the detections, and obtained a catalog including 14 robust line emitters. We identified eight serendipitous lines as [C II] emitters at $4.3 < z < 5.4$ while two lines are compatible with CO emission at lower redshift. The remaining detections do not present any optical/NIR counterpart but thay are likely associated to [C II] emission, based on the strict association with the central target or SED modeling.

We used both the eight confirmed [C II] emitters and the four lines without a counterpart to build the [C II] LF. We found strong clustering around the central ALPINE UV-targets, as 11 out of 12 sources show a velocity separation $|\Delta v| < 750$ km s^{-1} from the UV-target in the same pointing. In order to take the clustering effects into account when building the [C II] LF, we split our sample in two (i.e., a "clustered" and a "field" subsample) based on the redshift separation between the serendipitous line and

the central target in the same pointing. Then, we built two separate LFs. The clustered LF predicts an excess of sources compared to the LF of the UV-selected ALPINE targets and models expectations. On the other hand, the field LF results quite consistent with the LFs of the ALPINE targets, the serendipitous sources detected in the FIR continuum and the predictions of theoretical models. Both the clustered and field LFs suggest a possible evolution of the [C II] LF from $z \sim 5$ to $z \sim 0$. Observations of larger samples are necessary to confirm this trend as the field LF is based on one object only.

We used the [C II] emission as a star formation tracer. The validity of the SFR-[C II] relation at $z \sim 5$ was studied by Schaerer et al. (2020) using the ALPINE galaxies and we verified that it is also valid if we use the serendipitous sources detected both in [C II] and in continuum. We considered the estimate obtained for the field sample as representative of the average galaxy population since the clustered estimate could be biased towards a high-density environment. The field SFRD is a factor of ~ 1.6, on average, higher than the current estimates from UV surveys. However, because of the large errorbars, it is not possible for us to determine whether this value could be indicative of a significant fraction of obscured star formation at $z \sim 5$, as suggested by Gruppioni et al. (2020) based on the ALPINE serendipitous sources detected in the FIR continuum. Observations of larger samples are necessary to better constrain the SFRD of the Universe at these early epochs.

2) Quenching of star formation due to AGN feedback

We investigated the role of AGN in quenching star formation in massive galaxies. We studied this phenomenon in the active galaxy at $z \sim 2$ GMASS 0953. The richness in multiwavelength spectroscopic data makes this object ideal to study the kinematics of the ISM. We unveiled the existence of a multiphase disc supported by the [O III] $\lambda 5007$, Hα and CO(J=6-5) emission lines and an AGN-driven ionized outflow traced by [O III] $\lambda 5007$ and located in the central region of the galaxy.

We estimated the outflow rate in order to evaluate the impact of gas ejection on the galaxy. We found that the outflow rate amounts to ~ 120 M$_\odot$yr^{-1}, if the [O III] $\lambda 5007$ emission is obscured by dust, which corresponds to a depletion timescale of ~ 270 Myr, similar to that based on star formation (~ 150 Myr). Due to the two processes, GMASS 0953 is thus expected to rapidly quench the star formation activity, if the accretion of external gas is shutdown.

However, we stressed that the outflow rate is affected by several uncertainties. This quantity is derived under physical assumptions about the geometry, the electron number density, the metallicity and ionization state. The most dominant uncertainty is the extinction correction. We discussed indeed that applying or not applying this correction changes dramatically our results. If the outflow luminosity is not extincted by dust, the depletion timescale associated to the AGN-driven outflow becomes ~ 5.4 Gyr, negligible compared to that due to star formation. For these reasons, the role played by the AGN feedback in GMASS 0953 results quite uncertain and would need further investigation.

3) Triggering of star formation inside galactic outflows

We studied star formation inside galactic outflows in a sample of 70 nearby star-forming galaxies and AGN hosts. We used for the first time the C III $\lambda 1176$ photospheric line as a tracer of young stars inside galactic outflows. We found that several galaxies in our sample show blueshifted C III absorption, with velocities up to ~ -200 km s^{-1}, which could be indicative of stars inside the outflowing gas. The global distribution of the C III velocities is blueshifted and skewed towards the blue and differs from a Gaussian distribution centered around zero at $\gtrsim 90\%$ of confidence. The presence of blueshifted C III absorption seems to be correlated to the SFR and the AGN activity within the galaxies. We found an interesting correlation between the C III absorption and the OH 118 μm line, which traces the molecular phase of the outflow, in three galaxies of our sample. This fact suggests a possible connection between molecular outflows and the formation of stars, as suggested by models predictions.

All the topics treated in this work can be objects of further investigation in the future.

Regarding the ALPINE project, the discovery of important clustering around star-forming galaxies at $z \sim 5$ constitutes an intriguing subject. The study of the clustered sources would allow us to investigate the properties of overdense regions at high-z and compare with models predictions. Some studies found companions around quasars at $z > 6$, by studying the [C II] emission or the dust continuum (Decarli et al. 2017; Venemans et al. 2020). It would be very useful to compare the serendipitous sources around star-forming galaxies with the environment around quasars in order to understand if clustering is related to the AGN activity or it depends rather on the stellar mass of galaxies.

Another intriguing aspect concerning ALPINE could be to deepen the analysis on the serendipitous sources that do not present any optical/NIR counterpart. These objects could be representative of a population of extremely dusty galaxies whose emission emerges only at the longest wavelengths. Spectral scans with ALMA or NOEMA could be decisive in clarify the tricky nature of these sources.

Regarding the role of AGN-driven outflows in quenching star formation, we emphasized in our analysis of GMASS 0953 the uncertainties affecting the outflow rate. Several studies show that outflows are multiphase (e.g., Cicone et al. 2018). By using our data we could only constrain the ionized gas in the outflow, while we did not account for possible gas expulsion in other phases (e.g., molecular). Constraining the amount of molecular gas expelled by AGN is pivotal as this phase is suggested to be the dominant component of AGN-driven outflows (Fiore et al. 2017; Fluetsch et al. 2019) and because molecular gas is the fuel from which stars form. Deepest ALMA observations could provide key information on possible molecular gas ejection in GMASS 0953, as found for other galaxies at high redshift (Brusa et al. 2018).

Another important issue deals with the observational limits of integral field spectroscopy at high-z. We found indeed an interesting analogy between the observed [O III] $\lambda 5007$ and Hα velocity gradients in GMASS 0953 and the HI wind in the nearby galaxy M82. We thus cannot rule out the possibility that the observed emission in GMASS 0953 is due to a galaxy-scale wind. Despite finding this scenario unlikely, we caution the reader over the changelling interpretation of gas velocity gradients in low

spatial resolution data. The exquisite resolution provided by ALMA will aid in solving the degenerancy affecting the interpretation of velocity gradients at high redshift.

Finally, we will continue the analysis of the COS spectra of the galaxies studied in this thesis. In the future, it will be interesting to extend our study to a sample including more AGN, in order to assess the relevance of positive feedback in active galaxies with respect to the overall population of star-forming galaxies. Another promising perspective would be to study the C III line in a larger sample of objects with OH 119μm data to further constrain the correlation that we found between C III absorption and molecular gas ejection in three galaxies. Furthermore, the COS spectra analyzed in this thesis can be used to study also ISM lines. Their analysis can be useful to pinpoint ionized outflows possibly associated to newly formed stars. Lastly, it will be crucial to investigate star formation inside outflows at high-z, when AGN feedback is thought to play a much more important role, as distant quasars and massive star-forming galaxies present more powerful outflows.

Despite the remaining open questions, the study of cold gas and AGN-driven outflows with the most advanced spectroscopic facilities offer a unique and powerful approach to constrain the complex mechanisms that fuel and suppress star formation across cosmic time.

Bibliography

Aird, J., Nandra, K., Laird, E. S., et al. 2010, MNRAS, 401, 2531

Amblard, A., Riguccini, L., Temi, P., et al. 2014, ApJ, 783, 135

Aravena, M., Decarli, R., Gónzalez-López, J., et al. 2019, ApJ, 882, 136

Aravena, M., Decarli, R., Walter, F., et al. 2016, ApJ, 833, 68

Arnouts, S., Walcher, C. J., Le Fèvre, O., et al. 2007, A&A, 476, 137

Ashby, M. L. N., Willner, S. P., Fazio, G. G., et al. 2013, ApJ, 769, 80

Asplund, M., Grevesse, N., Sauval, A. J., & Scott, P. 2009, ARA&A, 47, 481

Baldwin, J. A., Phillips, M. M., & Terlevich, R. 1981, PASP, 93, 5

Barro, G., Kriek, M., Pérez-González, P. G., et al. 2017, ApJ, 851, L40

Baug, T., Dewangan, L. K., Ojha, D. K., et al. 2018, ApJ, 852, 119

Beckmann, R. S., Devriendt, J., Slyz, A., et al. 2017, MNRAS, 472, 949

Begeman, K. G. 1987, PhD thesis, , Kapteyn Institute, (1987)

Belokurov, V., Erkal, D., Evans, N. W., Koposov, S. E., & Deason, A. J. 2018, MNRAS, 478, 611

Bernardi, M., Meert, A., Sheth, R. K., et al. 2013, MNRAS, 436, 697

Berta, S., Lutz, D., Santini, P., et al. 2013, A&A, 551, A100

Béthermin, M., Fudamoto, Y., Ginolfi, M., et al. 2020, A&A, 643, A2

Bicknell, G. V., Sutherland, R. S., van Breugel, W. J. M., et al. 2000, ApJ, 540, 678

Binney, J. & Tremaine, S. 2008, Galactic Dynamics: Second Edition (Princeton University Press)

Blumenthal, G. R., Faber, S. M., Primack, J. R., & Rees, M. J. 1984, Nature, 311, 517

Bolatto, A. D., Wolfire, M., & Leroy, A. K. 2013, ARA&A, 51, 207

Bouwens, R. 2020, in The Build-Up of Galaxies through Multiple Tracers and Facilities, 17

Bouwens, R. J., Illingworth, G. D., Oesch, P. A., et al. 2012a, ApJ, 754, 83

Bouwens, R. J., Illingworth, G. D., Oesch, P. A., et al. 2015, ApJ, 803, 34

Bouwens, R. J., Illingworth, G. D., Oesch, P. A., et al. 2012b, ApJ, 752, L5

Bowler, R. A. A., Jarvis, M. J., Dunlop, J. S., et al. 2020, MNRAS, 493, 2059

Brammer, G. B., van Dokkum, P. G., Franx, M., et al. 2012, ApJS, 200, 13

Brightman, M. & Nandra, K. 2011, MNRAS, 413, 1206

Brusa, M., Bongiorno, A., Cresci, G., et al. 2015, MNRAS, 446, 2394

Brusa, M., Cresci, G., Daddi, E., et al. 2018, A&A, 612, A29

Calzetti, D., Armus, L., Bohlin, R. C., et al. 2000, ApJ, 533, 682

Cannon, J. M., Skillman, E. D., Kunth, D., et al. 2004, ApJ, 608, 768

Cano-Díaz, M., Maiolino, R., Marconi, A., et al. 2012, A&A, 537, L8

Capak, P., Aussel, H., Bundy, K., et al. 2012, SPLASH: Spitzer Large Area Survey with Hyper-Suprime-Cam, Spitzer Proposal

Capak, P., Carilli, C. L., Lee, N., et al. 2008, ApJ, 681, L53

Capak, P. L., Carilli, C., Jones, G., et al. 2015, Nature, 522, 455

Capak, P. L., Riechers, D., Scoville, N. Z., et al. 2011, Nature, 470, 233

Cardamone, C. N., van Dokkum, P. G., Urry, C. M., et al. 2010, ApJS, 189, 270

Carilli, C. L. & Walter, F. 2013, ARA&A, 51, 105

Carniani, S., Maiolino, R., Amorin, R., et al. 2018, MNRAS, 478, 1170

Carniani, S., Maiolino, R., De Zotti, G., et al. 2015a, A&A, 584, A78

Carniani, S., Maiolino, R., Pallottini, A., et al. 2017a, A&A, 605, A42

Carniani, S., Marconi, A., Maiolino, R., et al. 2015b, A&A, 580, A102

Carniani, S., Marconi, A., Maiolino, R., et al. 2017b, A&A, 605, A105

Casey, C. M., Narayanan, D., & Cooray, A. 2014, Phys. Rep., 541, 45

Chabrier, G. 2003, PASP, 115, 763

Chapman, S. C., Blain, A. W., Smail, I., & Ivison, R. J. 2005, ApJ, 622, 772

Chen, C.-C., Hodge, J. A., Smail, I., et al. 2017, ApJ, 846, 108

Chisholm, J., Rigby, J. R., Bayliss, M., et al. 2019, ApJ, 882, 182

Chisholm, J., Tremonti, C., & Leitherer, C. 2018, MNRAS, 481, 1690

Chisholm, J., Tremonti, C. A., Leitherer, C., Chen, Y., & Wofford, A. 2016, MNRAS, 457, 3133

Cicone, C., Brusa, M., Ramos Almeida, C., et al. 2018, Nature Astronomy, 2, 176

Cicone, C., Maiolino, R., Aalto, S., Muller, S., & Feruglio, C. 2020, A&A, 633, A163

Cicone, C., Maiolino, R., Sturm, E., et al. 2014, A&A, 562, A21

Cimatti, A., Brusa, M., Talia, M., et al. 2013, ApJ, 779, L13

Cimatti, A., Cassata, P., Pozzetti, L., et al. 2008, A&A, 482, 21

Cimatti, A., Daddi, E., Renzini, A., et al. 2004, Nature, 430, 184

Cooke, E. A., Smail, I., Swinbank, A. M., et al. 2018, ApJ, 861, 100

Cormier, D., Lebouteiller, V., Madden, S. C., et al. 2012, A&A, 548, A20

Cresci, G., Mainieri, V., Brusa, M., et al. 2015, ApJ, 799, 82

Cresci, G. & Maiolino, R. 2018, Nature Astronomy, 2, 179

Cucciati, O., Lemaux, B. C., Zamorani, G., et al. 2018, A&A, 619, A49

Cucciati, O., Tresse, L., Ilbert, O., et al. 2012, A&A, 539, A31

da Cunha, E., Charlot, S., & Elbaz, D. 2008, MNRAS, 388, 1595

Daddi, E., Cimatti, A., Renzini, A., et al. 2004, ApJ, 600, L127

Daddi, E., Dannerbauer, H., Liu, D., et al. 2015, A&A, 577, A46

Daddi, E., Dickinson, M., Morrison, G., et al. 2007, ApJ, 670, 156

Dahlen, T., Mobasher, B., Dickinson, M., et al. 2007, ApJ, 654, 172

Davé, R., Katz, N., Oppenheimer, B. D., Kollmeier, J. A., & Weinberg, D. H. 2013, MNRAS, 434, 2645

de Blok, W. J. G., Walter, F., Brinks, E., et al. 2008, AJ, 136, 2648

De Looze, I., Cormier, D., Lebouteiller, V., et al. 2014, A&A, 568, A62

Decarli, R., Aravena, M., Boogaard, L., et al. 2020, arXiv e-prints, arXiv:2009.10744

Decarli, R., Dotti, M., Bañados, E., et al. 2019a, ApJ, 880, 157

Decarli, R., Walter, F., Aravena, M., et al. 2016, ApJ, 833, 69

Decarli, R., Walter, F., Gónzalez-López, J., et al. 2019b, ApJ, 882, 138

Decarli, R., Walter, F., Venemans, B. P., et al. 2017, Nature, 545, 457

Decarli, R., Walter, F., Venemans, B. P., et al. 2018, ApJ, 854, 97

Dekel, A., Birnboim, Y., Engel, G., et al. 2009, Nature, 457, 451

Delvecchio, I., Gruppioni, C., Pozzi, F., et al. 2014, MNRAS, 439, 2736

Dessauges-Zavadsky, M., Ginolfi, M., Pozzi, F., et al. 2020, A&A, 643, A5

Di Matteo, T., Springel, V., & Hernquist, L. 2005, Nature, 433, 604

Di Teodoro, E. M. & Fraternali, F. 2015, MNRAS, 451, 3021

Di Teodoro, E. M., Fraternali, F., & Miller, S. H. 2016, A&A, 594, A77

Díaz-Santos, T., Armus, L., Charmandaris, V., et al. 2013, ApJ, 774, 68

Díaz-Santos, T., Assef, R. J., Blain, A. W., et al. 2018, Science, 362, 1034

Dickinson, M., Giavalisco, M., & GOODS Team. 2003, in The Mass of Galaxies at Low
    and High Redshift, ed. R. Bender & A. Renzini, 324

Dietrich, J., Weiner, A. S., Ashby, M. L. N., et al. 2018, MNRAS, 480, 3562

Driver, S. P., Andrews, S. K., da Cunha, E., et al. 2018, MNRAS, 475, 2891

Duc, P. A., Mirabel, I. F., & Maza, J. 1997, A&AS, 124, 533

Dunlop, J. S., McLure, R. J., Biggs, A. D., et al. 2017, MNRAS, 466, 861

Eisenhauer, F., Abuter, R., Bickert, K., et al. 2003, in Proc. SPIE, Vol. 4841, Instru-
    ment Design and Performance for Optical/Infrared Ground-based Telescopes, ed.
    M. Iye & A. F. M. Moorwood, 1548–1561

Elbaz, D., Dickinson, M., Hwang, H. S., et al. 2011, A&A, 533, A119

Elias, J. H., Joyce, R. R., Liang, M., et al. 2006, in Proc. SPIE, Vol. 6269, Society of
    Photo-Optical Instrumentation Engineers (SPIE) Conference Series, 62694C

Faber, S. M., Phillips, A. C., Kibrick, R. I., et al. 2003, in Society of Photo-Optical In-
    strumentation Engineers (SPIE) Conference Series, Vol. 4841, Instrument Design and
    Performance for Optical/Infrared Ground-based Telescopes, ed. M. Iye & A. F. M.
    Moorwood, 1657–1669

Fabian, A. C. 2012, ARA&A, 50, 455

Faisst, A. L., Capak, P. L., Yan, L., et al. 2017, ApJ, 847, 21

Faisst, A. L., Schaerer, D., Lemaux, B. C., et al. 2020, ApJS, 247, 61

Feltre, A., Charlot, S., & Gutkin, J. 2016, MNRAS, 456, 3354

Ferrarese, L. & Merritt, D. 2000, ApJ, 539, L9

Ferrero, I., Navarro, J. F., Abadi, M. G., et al. 2017, MNRAS, 464, 4736

Feruglio, C., Maiolino, R., Piconcelli, E., et al. 2010, A&A, 518, L155

Finkelstein, S. L. 2016, PASA, 33, e037

Fiore, F., Feruglio, C., Shankar, F., et al. 2017, A&A, 601, A143

Fischer, J., Sturm, E., González-Alfonso, E., et al. 2010, A&A, 518, L41

Fluetsch, A., Maiolino, R., Carniani, S., et al. 2019, MNRAS, 483, 4586

Fontana, A., Pozzetti, L., Donnarumma, I., et al. 2004, A&A, 424, 23

Foreman-Mackey, D., Hogg, D. W., Lang, D., & Goodman, J. 2013, PASP, 125, 306

Förster Schreiber, N. M., Genzel, R., Bouché, N., et al. 2009, ApJ, 706, 1364

Förster Schreiber, N. M., Genzel, R., Lehnert, M. D., et al. 2006, ApJ, 645, 1062

Förster Schreiber, N. M., Genzel, R., Newman, S. F., et al. 2014, ApJ, 787, 38

Förster Schreiber, N. M., Übler, H., Davies, R. L., et al. 2019, ApJ, 875, 21

Fox, A. J., Barger, K. A., Wakker, B. P., et al. 2018, ApJ, 854, 142

Franco, M., Elbaz, D., Béthermin, M., et al. 2018, A&A, 620, A152

Fudamoto, Y., Oesch, P. A., Faisst, A., et al. 2020, arXiv e-prints, arXiv:2004.10760

Fujimoto, S., Ouchi, M., Ferrara, A., et al. 2019, ApJ, 887, 107

Fujimoto, S., Ouchi, M., Ono, Y., et al. 2016, ApJS, 222, 1

Fujimoto, S., Ouchi, M., Shibuya, T., & Nagai, H. 2017, ApJ, 850, 83

Fujimoto, S., Silverman, J. D., Bethermin, M., et al. 2020, arXiv e-prints, arXiv:2003.00013

Gallagher, R., Maiolino, R., Belfiore, F., et al. 2019, MNRAS, 485, 3409

Geach, J. E., Dunlop, J. S., Halpern, M., et al. 2017, MNRAS, 465, 1789

Gebhardt, K., Kormendy, J., Ho, L. C., et al. 2000, ApJ, 543, L5

Gehrels, N. 1986, ApJ, 303, 336

Genzel, R., Förster Schreiber, N. M., Rosario, D., et al. 2014, ApJ, 796, 7

Genzel, R., Schreiber, N. M. F., Übler, H., et al. 2017, Nature, 543, 397

Genzel, R., Tacconi, L. J., Kurk, J., et al. 2013, ApJ, 773, 68

Giacconi, R., Zirm, A., Wang, J., et al. 2002, ApJS, 139, 369

Giavalisco, M., Ferguson, H. C., Koekemoer, A. M., et al. 2004, ApJ, 600, L93

Ginolfi, M., Jones, G. C., Béthermin, M., et al. 2020a, A&A, 643, A7

Ginolfi, M., Jones, G. C., Béthermin, M., et al. 2020b, A&A, 633, A90

Glazebrook, K., Abraham, R. G., McCarthy, P. J., et al. 2004, Nature, 430, 181

González-López, J., Decarli, R., Pavesi, R., et al. 2019, ApJ, 882, 139

González-López, J., Novak, M., Decarli, R., et al. 2020, ApJ, 897, 91

Graciá-Carpio, J., Sturm, E., Hailey-Dunsheath, S., et al. 2011, ApJ, 728, L7

Grazian, A., Fontana, A., de Santis, C., et al. 2006, A&A, 449, 951

Gruppioni, C., Béthermin, M., Loiacono, F., et al. 2020, A&A, 643, A8

Gruppioni, C., Calura, F., Pozzi, F., et al. 2015, MNRAS, 451, 3419

Gruppioni, C. & Pozzi, F. 2019, MNRAS, 483, 1993

Gruppioni, C., Pozzi, F., Rodighiero, G., et al. 2013, MNRAS, 432, 23

Gullberg, B., Smail, I., Swinbank, A. M., et al. 2019, MNRAS, 490, 4956

Guo, Y., Ferguson, H. C., Giavalisco, M., et al. 2013, ApJS, 207, 24

Harikane, Y., Ouchi, M., Shibuya, T., et al. 2018, ApJ, 859, 84

Harrison, C. M., Alexander, D. M., Mullaney, J. R., & Swinbank, A. M. 2014, MNRAS, 441, 3306

Harrison, C. M., Alexander, D. M., Swinbank, A. M., et al. 2012, MNRAS, 426, 1073

Harrison, C. M., Costa, T., Tadhunter, C. N., et al. 2018, Nature Astronomy, 2, 198

Hashimoto, T., Inoue, A. K., Mawatari, K., et al. 2019, PASJ, 71, 71

Hashimoto, T., Laporte, N., Mawatari, K., et al. 2018, Nature, 557, 392

Hasinger, G., Capak, P., Salvato, M., et al. 2018, ApJ, 858, 77

Hatsukade, B., Kohno, K., Yamaguchi, Y., et al. 2018, PASJ, 70, 105

Hatsukade, B., Ohta, K., Seko, A., Yabe, K., & Akiyama, M. 2013, ApJ, 769, L27

Hawkins, E., Maddox, S., Branchini, E., & Saunders, W. 2001, MNRAS, 325, 589

Heap, S. R., Lanz, T., & Hubeny, I. 2006, ApJ, 638, 409

Heckman, T. M., Armus, L., & Miley, G. K. 1990, ApJS, 74, 833

Heckman, T. M. & Thompson, T. A. 2017, arXiv e-prints [`arXiv:1701.09062`]

Hemmati, S., Yan, L., Diaz-Santos, T., et al. 2017, ApJ, 834, 36

Hennawi, J. F., Myers, A. D., Shen, Y., et al. 2010, ApJ, 719, 1672

Hernan-Caballero, A., Spoon, H. W. W., Lebouteiller, V., Rupke, D. S. N., & Barry, D. P. 2016, VizieR Online Data Catalog, J/MNRAS/455/1796

Herrera-Camus, R., Tacconi, L., Genzel, R., et al. 2019, ApJ, 871, 37

Hodge, J. A. & da Cunha, E. 2020, arXiv e-prints, arXiv:2004.00934

Hodge, J. A., Smail, I., Walter, F., et al. 2019, ApJ, 876, 130

Hollenbach, D. J. & Tielens, A. G. G. M. 1999, Reviews of Modern Physics, 71, 173

Hopkins, P. F., Torrey, P., Faucher-Giguère, C.-A., Quataert, E., & Murray, N. 2016, MNRAS, 458, 816

Hughes, D. H., Serjeant, S., Dunlop, J., et al. 1998, Nature, 394, 241

Iorio, G., Fraternali, F., Nipoti, C., et al. 2017, MNRAS, 466, 4159

Ishibashi, W. & Fabian, A. C. 2012, MNRAS, 427, 2998

Ishibashi, W. & Fabian, A. C. 2014, MNRAS, 441, 1474

Ishibashi, W. & Fabian, A. C. 2015, MNRAS, 451, 93

Ivison, R. J., Dunlop, J. S., Hughes, D. H., et al. 1998, ApJ, 494, 211

James, B. L., Aloisi, A., Heckman, T., Sohn, S. T., & Wolfe, M. A. 2014, ApJ, 795, 109

James, B. L., Tsamis, Y. G., Walsh, J. R., Barlow, M. J., & Westmoquette, M. S. 2013, MNRAS, 430, 2097

Jones, G. C., Béthermin, M., Fudamoto, Y., et al. 2020, MNRAS, 491, L18

Jones, G. C., Carilli, C. L., Shao, Y., et al. 2017, ApJ, 850, 180

Kauffmann, G., Heckman, T. M., Tremonti, C., et al. 2003, MNRAS, 346, 1055

Kennicutt, Robert C., J. 1998a, ApJ, 498, 541

Kennicutt, Jr., R. C. 1998b, ARA&A, 36, 189

Kereš, D., Katz, N., Weinberg, D. H., & Davé, R. 2005, MNRAS, 363, 2

Kewley, L. J., Groves, B., Kauffmann, G., & Heckman, T. 2006, MNRAS, 372, 961

Khusanova, Y., Béthermin, M., Le Fèvre, O., et al. 2020, arXiv e-prints, arXiv:2007.08384

King, A. 2005, ApJ, 635, L121

Kistler, M. D., Yüksel, H., Beacom, J. F., Hopkins, A. M., & Wyithe, J. S. B. 2009, ApJ, 705, L104

Koekemoer, A. M., Aussel, H., Calzetti, D., et al. 2007, ApJS, 172, 196

Koekemoer, A. M., Faber, S. M., Ferguson, H. C., et al. 2011, ApJS, 197, 36

Kohandel, M., Pallottini, A., Ferrara, A., et al. 2019, MNRAS, 487, 3007

Kriek, M., van Dokkum, P. G., Franx, M., et al. 2008, ApJ, 677, 219

Kriss, G. 1994, in Astronomical Society of the Pacific Conference Series, Vol. 61, Astronomical Data Analysis Software and Systems III, ed. D. R. Crabtree, R. J. Hanisch, & J. Barnes, 437

Kroupa, P. 2001, MNRAS, 322, 231

Kurk, J., Cimatti, A., Daddi, E., et al. 2013, A&A, 549, A63

Lacey, C. & Cole, S. 1993, MNRAS, 262, 627

Lagache, G., Cousin, M., & Chatzikos, M. 2018, A&A, 609, A130

Laigle, C., McCracken, H. J., Ilbert, O., et al. 2016, ApJS, 224, 24

Le Fèvre, O., Béthermin, M., Faisst, A., et al. 2020, A&A, 643, A1

Le Fèvre, O., Tasca, L. A. M., Cassata, P., et al. 2015, A&A, 576, A79

Le Floc'h, E., Aussel, H., Ilbert, O., et al. 2009, ApJ, 703, 222

Leitherer, C., Chandar, R., Tremonti, C. A., Wofford, A., & Schaerer, D. 2013, ApJ, 772, 120

Lelli, F., De Breuck, C., Falkendal, T., et al. 2018, MNRAS[arXiv:1807.03321]

Lelli, F., McGaugh, S. S., & Schombert, J. M. 2016a, AJ, 152, 157

Lelli, F., McGaugh, S. S., & Schombert, J. M. 2016b, ApJ, 816, L14

Lemaux, B. C., Cucciati, O., Le Fèvre, O., et al. 2020, arXiv e-prints, arXiv:2009.03324

Lemaux, B. C., Le Fèvre, O., Cucciati, O., et al. 2018, A&A, 615, A77

Lenkić, L., Bolatto, A. D., Förster Schreiber, N. M., et al. 2020, AJ, 159, 190

Leroy, A. K., Walter, F., Martini, P., et al. 2015, ApJ, 814, 83

Li, C. & White, S. D. M. 2009, MNRAS, 398, 2177

Liu, D., Schinnerer, E., Groves, B., et al. 2019, ApJ, 887, 235

Loiacono, F., Decarli, R., Gruppioni, C., et al. 2020, arXiv e-prints, arXiv:2006.04837

Luo, B., Brandt, W. N., Xue, Y. Q., et al. 2017, ApJS, 228, 2

Lutz, D., Poglitsch, A., Altieri, B., et al. 2011, A&A, 532, A90

Madau, P. & Dickinson, M. 2014, ARA&A, 52, 415

Madden, S. C., Poglitsch, A., Geis, N., Stacey, G. J., & Townes, C. H. 1997, ApJ, 483, 200

Magdis, G. E., Rigopoulou, D., Hopwood, R., et al. 2014, ApJ, 796, 63

Magnelli, B., Elbaz, D., Chary, R. R., et al. 2011, A&A, 528, A35

Magnelli, B., Popesso, P., Berta, S., et al. 2013, A&A, 553, A132

Magorrian, J., Tremaine, S., Richstone, D., et al. 1998, AJ, 115, 2285

Maiolino, R., Carniani, S., Fontana, A., et al. 2015, MNRAS, 452, 54

Maiolino, R., Russell, H. R., Fabian, A. C., et al. 2017, Nature, 544, 202

Malhotra, S., Helou, G., Stacey, G., et al. 1997, ApJ, 491, L27

Maniyar, A. S., Béthermin, M., & Lagache, G. 2018, A&A, 614, A39

Marchesi, S., Civano, F., Elvis, M., et al. 2016, ApJ, 817, 34

Marconi, A. & Hunt, L. K. 2003, ApJ, 589, L21

Marshall, H. L., Tananbaum, H., Zamorani, G., et al. 1983, ApJ, 269, 42

Martini, P., Leroy, A. K., Mangum, J. G., et al. 2018, ApJ, 856, 61

Matthee, J., Sobral, D., Boogaard, L. A., et al. 2019, ApJ, 881, 124

McCracken, H. J., Milvang-Jensen, B., Dunlop, J., et al. 2012, A&A, 544, A156

McGaugh, S. S., Schombert, J. M., Bothun, G. D., & de Blok, W. J. G. 2000, ApJ, 533, L99

Meyer, M. J., Zwaan, M. A., Webster, R. L., et al. 2004, MNRAS, 350, 1195

Mignoli, M., Cimatti, A., Zamorani, G., et al. 2005, A&A, 437, 883

Morganti, R., Veilleux, S., Oosterloo, T., Teng, S. H., & Rupke, D. 2016, A&A, 593, A30

Mutch, S. J., Croton, D. J., & Poole, G. B. 2011, ApJ, 736, 84

Naab, T. & Ostriker, J. P. 2017, ARA&A, 55, 59

Nardini, E., Risaliti, G., Salvati, M., et al. 2009, MNRAS, 399, 1373

Nayakshin, S. & Zubovas, K. 2012, MNRAS, 427, 372

Nelson, D., Pillepich, A., Springel, V., et al. 2018, MNRAS, 475, 624

Nesvadba, N. P. H., Cañameras, R., Kneissl, R., et al. 2019, A&A, 624, A23

Newman, S. F., Buschkamp, P., Genzel, R., et al. 2014, ApJ, 781, 21

Noordermeer, E., van der Hulst, J. M., Sancisi, R., Swaters, R. S., & van Albada, T. S. 2007, MNRAS, 376, 1513

Norman, C., Ptak, A., Hornschemeier, A., et al. 2004, ApJ, 607, 721

Novak, M., Bañados, E., Decarli, R., et al. 2019, ApJ, 881, 63

Novak, M., Smolčić, V., Delhaize, J., et al. 2017, A&A, 602, A5

Oesch, P. A., Bouwens, R. J., Illingworth, G. D., Labbé, I., & Stefanon, M. 2018, ApJ, 855, 105

Olsen, K., Greve, T. R., Narayanan, D., et al. 2017, ApJ, 846, 105

Onodera, M., Carollo, C. M., Renzini, A., et al. 2015, ApJ, 808, 161

Osterbrock, D. E. & Ferland, G. J. 2006, Astrophysics of gaseous nebulae and active galactic nuclei

Pallottini, A., Ferrara, A., Decataldo, D., et al. 2019, MNRAS, 487, 1689

Pavesi, R., Riechers, D. A., Capak, P. L., et al. 2016, ApJ, 832, 151

Pavesi, R., Riechers, D. A., Sharon, C. E., et al. 2018a, ApJ, 861, 43

Pavesi, R., Sharon, C. E., Riechers, D. A., et al. 2018b, ApJ, 864, 49

Pellerin, A., Fullerton, A. W., Robert, C., et al. 2002, ApJS, 143, 159

Pillepich, A., Springel, V., Nelson, D., et al. 2018, MNRAS, 473, 4077

Popping, G., Decarli, R., Man, A. W. S., et al. 2017, A&A, 602, A11

Popping, G., Narayanan, D., Somerville, R. S., Faisst, A. L., & Krumholz, M. R. 2019, MNRAS, 482, 4906

Pustilnik, S. A., Engels, D., Ugryumov, A. V., et al. 1999, A&AS, 137, 299

Rahmani, S., Lianou, S., & Barmby, P. 2016, MNRAS, 456, 4128

Reddy, N. A. & Steidel, C. C. 2009, ApJ, 692, 778

Riechers, D. A., Bradford, C. M., Clements, D. L., et al. 2013, Nature, 496, 329

Riechers, D. A., Capak, P. L., Carilli, C. L., et al. 2010, ApJ, 720, L131

Riechers, D. A., Carilli, C. L., Capak, P. L., et al. 2014, ApJ, 796, 84

Riechers, D. A., Pavesi, R., Sharon, C. E., et al. 2019, ApJ, 872, 7

Riess, A. G., Filippenko, A. V., Challis, P., et al. 1998, AJ, 116, 1009

Rines, K., Geller, M. J., Kurtz, M. J., & Diaferio, A. 2003, AJ, 126, 2152

Robotham, A. S. G. & Driver, S. P. 2011, MNRAS, 413, 2570

Rodighiero, G., Daddi, E., Baronchelli, I., et al. 2011, ApJ, 739, L40

Rodríguez del Pino, B., Arribas, S., Piqueras López, J., Villar-Martín, M., & Colina, L. 2019, MNRAS, 486, 344

Rodríguez-Zaurín, J., Arribas, S., Monreal-Ibero, A., et al. 2011, A&A, 527, A60

Rogstad, D. H., Lockhart, I. A., & Wright, M. C. H. 1974, ApJ, 193, 309

Romano, M., Cassata, P., Morselli, L., et al. 2020, arXiv e-prints, arXiv:2002.00961

Roseboom, I. G., Oliver, S. J., Kunz, M., et al. 2010, MNRAS, 409, 48

Rowan-Robinson, M., Oliver, S., Wang, L., et al. 2016, MNRAS, 461, 1100

Rupke, D. S., Veilleux, S., & Sanders, D. B. 2005, ApJ, 632, 751

Rupke, D. S. N., Gültekin, K., & Veilleux, S. 2017, ApJ, 850, 40

Rupke, D. S. N. & Veilleux, S. 2011, ApJ, 729, L27

Sanders, D. B., Mazzarella, J. M., Kim, D. C., Surace, J. A., & Soifer, B. T. 2003, AJ, 126, 1607

Sanders, D. B., Salvato, M., Aussel, H., et al. 2007, ApJS, 172, 86

Sardaneta, M. M., Rosado, M., & Sánchez-Cruces, M. 2020, Rev. Mexicana Astron. Astrofis., 56, 71

Saunders, W., Sutherland, W. J., Maddox, S. J., et al. 2000, MNRAS, 317, 55

Schaaf, R., Pietsch, W., Biermann, P. L., Kronberg, P. P., & Schmutzler, T. 1989, ApJ, 336, 722

Schaerer, D., Ginolfi, M., Bethermin, M., et al. 2020, arXiv e-prints, arXiv:2002.00979

Schechter, P. 1976, ApJ, 203, 297

Schenker, M. A., Robertson, B. E., Ellis, R. S., et al. 2013, ApJ, 768, 196

Schiminovich, D., Ilbert, O., Arnouts, S., et al. 2005, ApJ, 619, L47

Schinnerer, E., Carilli, C. L., Capak, P., et al. 2008, ApJ, 689, L5

Schmidt, M. 1968, ApJ, 151, 393

Scoville, N., Aussel, H., Brusa, M., et al. 2007, ApJS, 172, 1

Scoville, N., Lee, N., Vanden Bout, P., et al. 2017, ApJ, 837, 150

Scoville, N., Sheth, K., Aussel, H., et al. 2016, ApJ, 820, 83

Shankar, F., Weinberg, D. H., & Miralda-Escudé, J. 2009, ApJ, 690, 20

Shapley, A. E., Steidel, C. C., Pettini, M., & Adelberger, K. L. 2003, ApJ, 588, 65

Sharples, R., Bender, R., Agudo Berbel, A., et al. 2013, The Messenger, 151, 21

Shopbell, P. L. & Bland-Hawthorn, J. 1998, ApJ, 493, 129

Sijacki, D., Springel, V., Di Matteo, T., & Hernquist, L. 2007, MNRAS, 380, 877

Silk, J. 2013, ApJ, 772, 112

Smit, R., Bouwens, R. J., Carniani, S., et al. 2018, Nature, 553, 178

Smolčić, V., Novak, M., Bondi, M., et al. 2017, A&A, 602, A1

Solomon, P. M., Downes, D., & Radford, S. J. E. 1992, ApJ, 398, L29

Souchay, J., Andrei, A. H., Barache, C., et al. 2015, A&A, 583, A75

Speagle, J. S., Steinhardt, C. L., Capak, P. L., & Silverman, J. D. 2014, ApJS, 214, 15

Spekkens, K. & Giovanelli, R. 2006, AJ, 132, 1426

Spilker, J. S., Bezanson, R., Marrone, D. P., et al. 2016, ApJ, 832, 19

Spinoglio, L. & Malkan, M. A. 1992, ApJ, 399, 504

Springel, V., Di Matteo, T., & Hernquist, L. 2005, ApJ, 620, L79

Stacey, G. J., Hailey-Dunsheath, S., Ferkinhoff, C., et al. 2010, ApJ, 724, 957

Steidel, C. C., Erb, D. K., Shapley, A. E., et al. 2010, ApJ, 717, 289

Steinmetz, M. & Navarro, J. F. 2002, New A, 7, 155

Stierwalt, S., Armus, L., Surace, J. A., et al. 2013, ApJS, 206, 1

Swaters, R. A., Sancisi, R., van Albada, T. S., & van der Hulst, J. M. 2009, A&A, 493, 871

Swinbank, A. M., Karim, A., Smail, I., et al. 2012, MNRAS, 427, 1066

Tacconi, L. J., Genzel, R., Saintonge, A., et al. 2018, ApJ, 853, 179

Tadaki, K.-i., Kodama, T., Nelson, E. J., et al. 2017, ApJ, 841, L25

Takeuchi, T. T., Yoshikawa, K., & Ishii, T. T. 2003, ApJ, 587, L89

Talia, M., Cimatti, A., Giulietti, M., et al. 2020, arXiv e-prints, arXiv:2011.03051

Talia, M., Mignoli, M., Cimatti, A., et al. 2012, A&A, 539, A61

Talia, M., Pozzi, F., Vallini, L., et al. 2018, MNRAS, 476, 3956

Thomas, D., Maraston, C., Schawinski, K., Sarzi, M., & Silk, J. 2010, MNRAS, 404, 1775

Tully, R. B. & Fisher, J. R. 1977, A&A, 54, 661

Übler, H., Genzel, R., Tacconi, L. J., et al. 2018, ApJ, 854, L24

Ueda, Y., Hatsukade, B., Kohno, K., et al. 2018, ApJ, 853, 24

Valentino, F., Magdis, G. E., Daddi, E., et al. 2018, ApJ, 869, 27

Valentino, F., Tanaka, M., Davidzon, I., et al. 2020, ApJ, 889, 93

Vallini, L., Gallerani, S., Ferrara, A., Pallottini, A., & Yue, B. 2015, ApJ, 813, 36

Vallini, L., Gruppioni, C., Pozzi, F., Vignali, C., & Zamorani, G. 2016, MNRAS, 456, L40

van der Hulst, J. M., Terlouw, J. P., Begeman, K. G., Zwitser, W., & Roelfsema, P. R. 1992, in Astronomical Society of the Pacific Conference Series, Vol. 25, Astronomical Data Analysis Software and Systems I, ed. D. M. Worrall, C. Biemesderfer, & J. Barnes, 131

van der Wel, A., Franx, M., van Dokkum, P. G., et al. 2014, ApJ, 788, 28

van Dokkum, P. G., Kriek, M., Rodgers, B., Franx, M., & Puxley, P. 2005, ApJ, 622, L13

van Dokkum, P. G., Nelson, E. J., Franx, M., et al. 2015, ApJ, 813, 23

Veilleux, S., Meléndez, M., Sturm, E., et al. 2013a, ApJ, 776, 27

Veilleux, S., Trippe, M., Hamann, F., et al. 2013b, ApJ, 764, 15

Venemans, B. P., Walter, F., Neeleman, M., et al. 2020, ApJ, 904, 130

Vogelsberger, M., Genel, S., Springel, V., et al. 2014, MNRAS, 444, 1518

Walter, F., Carilli, C., Neeleman, M., et al. 2020, ApJ, 902, 111

Walter, F., Decarli, R., Aravena, M., et al. 2016, ApJ, 833, 67

Walter, F., Decarli, R., Carilli, C., et al. 2012, Nature, 486, 233

Walter, F., Weiß, A., Downes, D., Decarli, R., & Henkel, C. 2011, ApJ, 730, 18

Wang, X. & Loeb, A. 2018, New A, 61, 95

Wardlow, J. L., Simpson, J. M., Smail, I., et al. 2018, MNRAS, 479, 3879

Weinberger, R., Springel, V., Hernquist, L., et al. 2017, MNRAS, 465, 3291

Weinberger, R., Springel, V., Pakmor, R., et al. 2018, MNRAS, 479, 4056

Weiß, A., Kovács, A., Coppin, K., et al. 2009, ApJ, 707, 1201

Williams, C. C., Labbe, I., Spilker, J., et al. 2019, ApJ, 884, 154

Willott, C. J., Carilli, C. L., Wagg, J., & Wang, R. 2015, ApJ, 807, 180

Wisnioski, E., Förster Schreiber, N. M., Fossati, M., et al. 2019, ApJ, 886, 124

Wisnioski, E., Förster Schreiber, N. M., Wuyts, S., et al. 2015, ApJ, 799, 209

Wisnioski, E., Mendel, J. T., Förster Schreiber, N. M., et al. 2018, ApJ, 855, 97

Wofford, A., Leitherer, C., & Salzer, J. 2013, ApJ, 765, 118

Wolfire, M. G., McKee, C. F., Hollenbach, D., & Tielens, A. G. G. M. 2003, ApJ, 587, 278

Wong, O. I., Ryan-Weber, E. V., Garcia-Appadoo, D. A., et al. 2006, MNRAS, 371, 1855

Wuyts, E., Wisnioski, E., Fossati, M., et al. 2016, ApJ, 827, 74

Wyder, T. K., Treyer, M. A., Milliard, B., et al. 2005, ApJ, 619, L15

Yamaguchi, Y., Kohno, K., Tamura, Y., et al. 2017, ApJ, 845, 108

Yan, L., Sajina, A., Loiacono, F., et al. 2020, arXiv e-prints, arXiv:2006.04835

Yano, K., Nakagawa, T., Isobe, N., & Shirahata, M. 2016, ApJ, 833, 272

Yu, S., Bullock, J. S., Wetzel, A., et al. 2020, MNRAS, 494, 1539

Zanella, A., Daddi, E., Magdis, G., et al. 2018, MNRAS, 481, 1976

Zavagno, A., Russeil, D., Motte, F., et al. 2010, A&A, 518, L81

Zubovas, K. & Bourne, M. A. 2017, MNRAS, 468, 4956

Zubovas, K., Nayakshin, S., King, A., & Wilkinson, M. 2013a, MNRAS, 433, 3079

Zubovas, K., Wynn, G. A., & Gualandris, A. 2013b, ApJ, 771, 118